UNIVERSITY OF HULL

Anisotropic Particles at Liquid Interfaces

being a thesis submitted in fulfilment of the

requirements for the degree of

Doctor of

Philosophy

in the University of Hull

by

Scott Oliver Morgan M. Phys. (Hons.)

April 2022

Acknowledgements

I would like to thank my supervisor Dr. D. Martin A. Buzza for his excellent guidance, support and encouragement throughout, his extensive knowledge has been invaluable. I would also like to thank my research cluster supervisors Dr's A. M. Adawi, T. S. Horozov, J. S. G. Bouillard and G. J. Stasiuk for their ever-helpful feedback. Sincere gratitude goes to the University of Hull for waiving my fees and for granting me a scholarship to cover living expenses. I acknowledge the Viper High Performance Computing facility of the University of Hull and its support team. I would also like to thank Prof. K. A. Brakke for his assistance and guidance with some of the more difficult aspects of the Surface Evolver software. Finally, I would like to thank all my family, friends and my partner for their understanding and support throughout.

Publications and Conferences

S. O. Morgan, J. Fox, C. Lowe A. M. Adawi, J. S. Bouillard, G. J. Stasiuk, T. S. Horozov and D. M. Buzza, *Phys. Rev. E*, 2021, **103**, 042604.

S. O. Morgan, A. Muravitskaya, C. Lowe A. M. Adawi, J. S. Bouillard, G. J. Stasiuk, T. S. Horozov and D. M. Buzza, *Phys. Chem. Chem. Phys*, **24**, 11000-11013.

Abstract

In this thesis we study the adsorption dynamics and self-assembly of anisotropic particles at a liquid-liquid interface. Firstly, we couple a Langevin dynamics model with the high-resolution finite element analysis software package Surface Evolver, which explicitly includes interfacial deformations, to study the adsorption dynamics of ellipsoidal particles. Transient contact line pinning due to nanoscale defects on the particle surface are also included by renormalising particle friction coefficients and using dynamic contact angles relevant to the adsorption timescale. We reproduce the monotonic variation of particle orientation with time that is observed experimentally and are able to quantitatively model the adsorption dynamics for some experimental ellipsoidal systems but not others. However, even for the latter case, our model accurately captures the adsorption trajectory (i.e., particle orientation vs. height) of said particles.

Secondly, we extend our theoretical model to study cylindrical particles with the goal of using the adsorption kinetics of cylindrical nanorods at a liquid interface as a novel alternative route for assembling vertically aligned nanorod arrays. We find that the final orientation of non-neutrally wetting cylindrical nanorods is determined by their initial attack angle when they contact the liquid interface. Furthermore, the range of attack angles leading to the end-on state is maximised when nanorods approach the liquid interface from the bulk phase that is more energetically favorable.

Finally, we move from the role anisotropy plays in the adsorption process to investigating how particle anisotropy can be utilized to direct the self-assembly of particles adsorbed at a liquid-liquid interface. Specifically, by modeling undulating hexagonal-like platelets and changing the relative phase axis of the undulation's peaks

and the hexagonal particles vertices, we can direct the assembly to a number of different self-assembled ground states including hexagonal close packed, honeycomb and kagome lattices.

Contents

Glossary of Terms

Adsorption

The process by which a substance is accumulated at an interface or in an interfacial region.

Adsorption Coordinates

The specific spatial configuration of an anisotropic particle given in terms of the height of the centre of the particle relative to the planar interface and the angle between the planar normal and the semi-major axis of the particle.

Adsorption Kinetics

The evolution in time and space of a colloidal particle adsorbing at an interface from its initial breach to its equilibrated configuration.

Advancing Contact Angle

A dynamic contact angle between a liquid and solid which is produced in the course of the wetting process.

Anisotropic

The property of exhibiting properties with different values when measured along axes in different directions.

Arrhenius Equation

A formula relating the temperature dependence of reaction rates.

Area Fraction

The total area of an interface excluded by adsorbed particles divided by the total area of the planar interface.

Attack Angles

The angle formed between the semimajor axis of an anisotropic particle and the interface normal at the point of the initial interfacial breach.

Bijel

Bicontinuous interfacially jammed emulsion gels consisting of continuous, interpenetrating domains of two immiscible fluids maintained in a ridged arrangement by a jammed layer of interfacial colloids.

Bio-Locomotion

The various movements of organisms employed for self-propulsion.

Boltzmann Factor

The proportionality relating the average kinetic energy of particles in a gas to its thermodynamic temperature.

Bond Number

A dimensionless number describing the ratio of gravitational forces to surface tension forces.

Brownian Motion

Random fluctuations in the density of molecules in a liquid due to thermal energy.

Capillary Interactions

The attractive and repulsive interactions between adsorbed particles due to their overlapping menisci.

Capillary Number

The ratio of viscous to interfacial forces.

Centroid

The geometric centre of a plane figure.

Colloid

State of subdivision in which the particles have at least one dimension on the length scale between $1nm$ and $1\mu m$.

Common Tangent Line

A straight line which forms two tangents to a function.

Computational Complexity

The number of resources required to run an algorithm, which generally varies with the size of the input.

Contact Angle Hysteresis

The difference between advancing and receding contact angles due to heterogeneities of a surface.

Contact Line

The line circumscribing all points at which the three phases, liquid, vapour and solid meet.

Contact Line Pinning

The transient attachment of segment(s) of the three-phase contact line due to surface heterogeneities.

Continuous Phase

A phase which exhibits continuity throughout a dispersion.

Crystallography

The field of study concerned with determining the arrangement of atoms in crystalline materials.

Crystal Structure

A description of the symmetric patterns repeating along the principal directions in geometric space in a crystalline material.

Delaunay Triangulation

A tessellation of a set of points such that no single point lies inside the circumcircle of any triangle which composes the tessellation.

Depolarizing Factors

When an anisotropic shape is magnetized by a uniform field the total field inside the materiel and its surroundings change. Depolarizing factors attempt to correct for the shape anisotropy and are also known as demagnetizing factors.

Dielectric Strength

The electrical strength of an insulating material measured as the maximum voltage required to produce a dielectric breakdown.

Dimensionally Confined Nanostructures

A classification of materials having dimension which are outside of the nanoscale regime, i.e., less than $100nm$. Accordingly, the classification of a zero-dimensional (0D) material means that all dimensions are less than $100nm$, one-dimensional (1D) means that one dimension is outside this range, two dimensions are outside this range for 2D and all dimensions are outside of this scale for 3D materials.

Dimers

A colloid assembly consisting of two structural sub-units.

Dipole

An interfacial deformation around an adsorbed particle which is characterized by having a single depression and elevation with respect to the plane of the interface.

Dispersed Phase

The phase that is distributed in the form of discrete discontinuities within a second immiscible continuous phase.

Dispersion Force

Weak forces between molecules occurring due to either temporary or permanent dipoles which result in attractive or repulsive forces between molecules.

Dissipative Force

A force capable of translating mechanical energy into thermal energy causing energy to be lost from a system undergoing motion.

Dry Water

An air-water emulsion stabilized by silica particles.

Dynamic Contact Angle

The contact angle which occurs during the wetting or de-wetting of a solid.

Dynamical Attractor

A set of states to which a given system tends to evolve towards given a wide variety of initial conditions.

Dynamical State Vector

The vector fully describing an individual anisotropic particle's energetic configuration at a snapshot in time during the adsorption process.

Electrodeposition

A fabrication method used to create a metallic coating by using an electric current on a conductive material immersed in solution which contains a salt of the metal to be deposited.

Electrolytes

A substance which conducts current via dissociation into ions.

Emulsion

A dispersion consisting of two or more liquid phases.

Encapsulation

The creation of selectively permeable capsules composed of colloidal particles.

Epsilon-Near-Zero Materials

A category of materials having near zero refractive index resulting in unique linear and nonlinear optical properties.

Equilibrium Contact Angle

The contact angle satisfying the lowest free energy state of an adsorbed particle or droplet.

Evaporation Driven Assembly

The process of guiding disordered colloids adsorbed at an interface to ordered structures by evaporation of the continuous phase.

Far-Field

Far field is defined as the particle separation where only the leading order multipole capillary interaction is relevant. This distance is several multiples of the particle radius for a spherical particle.

Finite Element Analysis

A numerical method for solving partial differential equations. A mesh of an object is created from a space discretization having a finite number of points. A system of algebraic equations describing the applicable physical behaviour is applied and the approximate solution is calculated by minimising an associated error function.

Floatation Forces

The lateral capillary force between particles having a high bond number originating from the interaction of their menisci.

Fluctuation-Dissipation Theorem

The theory which quantifies the relationship between fluctuations in a system and the systems response to applied perturbations. For a given process which dissipates energy turning it into heat, for example a solid body translating through a fluid, there is a reverse process related to thermal fluctuations.

Free Energy

A measure of the capacity of a system to do work.

Free Energy Landscape

The free energy of a system as a function of its configuration.

Freeze-Fracture Shadow Casting cryo-SEM

The process of experimentally measuring wetting properties by creating a particle laden interface, jet-freezing and fracturing it with the interface acting as the weak fracture plane to expose immobilized nanoparticles. The interface is then unidirectionally metal coated and the nanoparticles heights above the interface measured via the length of their shadows.

Friction Coefficients

A measure of the amount of friction existing between two surfaces. In this thesis we consider two specifically, the translational and rotational friction coefficients.

Functionalized Facets

Alterations to the surface chemistry of specific particle faces.

Gel

A bicontinuous structure with a solid and liquid component.

Graphical Processing Unit

A specialised electronic circuit used to accelerate numerical calculations via mass parallelisation. Frequently abbreviated to GPU.

Haymaker Constant

A materiel constant which quantifies the relative strength of the attractive van der Waals forces.

Heterogeneities

The variance of properties of a system or unit of a system. With respect to colloidal particles this is usually due to variations in surface chemistry or particle shape.

Hexapole

An interfacial deformation around an adsorbed particle which is characterized by having three depressions and elevations with respect to the plane of the interface.

High Speed Confocal Microscopy

The experimental technique of producing images with high spatial resolution which uses a point illumination source and a pinhole at the confocal plane of a sample to eliminate out of focus light rays.

Holographic Microscopy

The recording of the light wave front information from an object in the form of a hologram and the reconstruction of the object image by a numerical reconstruction algorithm.

Homogeneous

The uniformity of properties of a system or unit of a system.

Hydrophobic

Describes a particle or substances interaction with water, in this case having the qualitative meaning “water fearing”.

Hydrophilic

Describes a particle or substances interaction with water, in this case having the qualitative meaning “water loving”.

Interface Compression

A technique used to compress monolayers on the surface of a subphase, usually with a Langmuir-Blodgett trough.

ITIES

An Interface between two immiscible electrolyte solutions.

Janus Particles

A particle whose surface has two or more distinct physical properties, can arise from variations in surface chemistry or particle morphology.

Kagome Lattice

A trihexagonal lattice consisting of two regular hexagons and two equilateral triangles alternating around each vertex.

Langevin Dynamics

A method of modelling the dynamics of molecular systems which approximates the canonical ensemble. The force on a given particle is calculated by summing the negative of the grad operator acting on a particle interaction potential with a damping term due to frictional forces and a final term due to random thermal fluctuations. The model can mimic viscous aspects of a solvent but neglects electrostatic screening effects.

Lattice Vector

A vector joining any two lattice points. Used to describe the unit cell of a periodic structure.

Line Tension

The energy term per unit length of the three-phase contact line due to the imbalance of intermolecular forces arising from the three phases intersecting at the contact line.

Liquid Marbles

Liquid droplets coated with hydrophobic powder.

Mesoscale Self-Assembly

The spontaneous ordering of objects ranging in size from $3nm - 10mm$ due to capillary, magnetic or electrostatic forces.

Metamaterials

Materials which have been engineered to have property(s) not found in naturally occurring materials such as negative refractive indices.

Metastable

An intermediate state in a dynamical system.

Monolayer

A layer of colloidal particles which has the thickness of a single particle.

Monopole

An interfacial deformation around an adsorbed particle arising from the presence of a vertical force acting on the particle. The interfacial deformation is either a depression or rise surrounding the particle with respect to the interface plane far from the particle.

Monotonic

A mathematical function which varies in a way that either never increases or never decreases.

Monte Carlo Methods

A class of simulation techniques which use repeated random sampling to obtain numerical results.

Multicomponent Lattice Boltzmann Model

A set of models which simulates complex flows from a statistical physics standpoint. A fluid is modelled initially by a distribution function used to describe the occupation of a lattice site with velocity and time also discretised. The location of particles in space is restrained to that of the lattice site and the simulation is propagated forwards in timesteps with the particle's velocity components and any particle collisions being updated on each iteration.

Nanolithography

A class of techniques for engineering nanometre scale structures. Depending on specific material constraints nanolithography can use light, electron beams or charged ions to transfer a pattern from a photomask to a photoresist layer which has been coated onto a substrate material.

Nanomaterials

Materials in which a single unit has a length scale between $1 - 100nm$ in at least one dimension.

Nanoscale Defects

Small, nanometre sized heterogeneities on a particles surface due to surface chemistry or particle morphology.

Nearfield

The distance beyond a colloids surface in which the higher order multipoles involved in capillary interactions become dominant. This distance is less than one radius from the surface for a spherical particle.

Neumann-Boundary Condition

A boundary condition which specifies the values of the derivative applied to the boundary of the domain.

Optical Trap

An instrument which uses a highly focused laser beam to trap a dielectric particle near the focal point of the laser beam. The particle experiences a force due to the transfer of momentum from the incident photons.

Parallel Computing

The process of breaking down larger, complex computational calculations into smaller parts which can be distributed and executed simultaneously over multiple processers.

Parallelepiped

A three-dimensional shape in which all the faces are parallelograms.

PDMS

Polydimethylsiloxane, a polymer which is frequently used to immobilise interfacial colloidal assemblies.

Plasmonic Cavity Resonators

In general, plasmonic cavity resonators are assemblies in which surface plasmons can be excited in structures with a geometry of 1D, 2D and 3D space dimensions.

Plasmonic Sensor

A sensing device which response to shifts in the spectral properties of plasmons acting as a transducer of the sensing signal.

PMMA

Poly(methyl methacrylate) a polymer which is frequently used to immobilise interfacial colloidal assemblies.

Polymeric Coatings

Thin layers of polymer applied to modify a particles surface properties.

Polarization Charge

The material response of a dielectric material when exposed to an electric field.

Quadrupole

An interfacial deformation around an adsorbed particle which is characterized by having two depressions and elevations with respect to the plane of the interface.

Quasi-Static

A process which occurs on a slow enough time frame that it appears to be in thermodynamic equilibrium.

Receding Contact Angle

A dynamic contact angle between a liquid drop and a solid which has already been wetted and is in the course of being de-wetted.

Reconfigurable Devices

Devices in which it is possible to switch back and forth between the equilibrium states of colloidal self-assembly. This is accomplished through manipulation of size, shape and interaction potential of the colloids themselves or alternatively the magnitude and direction of applied fields.

Reynolds Number

A dimensionless number which expresses the ratio of inertial forces to the viscous forces.

Separatrix

The locus of points in space in which the eigenvectors of the hessian matrix, with positive and negative values respectively, are parallel to the gradient.

Sessile Droplet

An immobile liquid droplet, in this context used as an experimental technique to measure contact angle hysteresis.

Simplices

A generalisation of a triangle to arbitrary dimensions.

Simplicial Complex

A mathematical set composed of points, line segments and facets.

Sol

A liquid dispersion containing particles of colloidal dimensions.

Stereolithography

An additive manufacturing process which works by focusing an ultraviolet light onto a vat of photopolymer resign and 3D printing an object layer by layer.

Steric Forces

Forces arising due to the arrangement of molecules and overlapping electron clouds.

Surface Energies

The work required to create an area of a particular surface due to the disruption of intermolecular bonds that occurs when a surface is created.

Surface Enhanced Raman Spectroscopy

A technique which enhances the inelastic scattering of incident photons by molecules adsorbed on rough metal surfaces or plasmonic structures.

Super-Ellipsoid Equation

A three-dimensional generalization of the ellipsoid which allows different exponents of the variables in its algebraic expression. Permits one to mathematically model a large range of shapes from spheres to cubes.

Tetramers

A colloid assembly consisting of four structural sub-units.

Two Dimensional Materials

A classification of a material which has two dimensions outside the nanoscale, i.e., less than $100nm$.

Viscous

The tendency of a liquid to resist flow because of internal friction.

Viscous Dissipation

An irreversible process in which the work done by a fluid on adjacent layers by the action of shear forces is converted to heat.

Viscous Drag

The resistance to movement felt on an object as it passes through a fluid due to the viscosity of the fluid.

Wettability

The ability of a liquid to maintain contact with a solid surface.

Young-Laplace Equation

An equation which describes the capillary pressure difference across an immiscible interface between two static fluids**.**

Chapter 1 Introduction

The field of interface and colloidal science is a union of disciplines such as chemistry, physics, nanotechnology and computational science dedicated to the study of colloidal systems. Loosely speaking, a colloid is a heterogeneous mixture of insoluble particles dispersed in a continuous medium, the particles of the colloid having at least one dimension in the range of $1nm$ to $1\mu m$.[1,2] The insoluble particles (or droplets) of the colloid being referred to as the dispersed phase and the medium being referred to as the continuous phase. The dispersed and/or continuous phase can be in gaseous, liquid or solid states with a range of sub-classifications for colloidal systems. In the case of an emulsion both dispersed and continuous phases are in the liquid state, whereas a gas dispersed in a liquid results in a foam, a solid dispersed in a liquid a sol and conversely a liquid dispersed in a solid a gel.[2]

1.1 Particles at an Interface

Solid particles adsorbed at liquid interfaces interface have been of scientific interest since the turn of the twentieth century when Ramsden first recognised that the presence of solid particles would prevent oil droplets dispersed in water from coalescing.[3] The phenomenon of Pickering emulsions was formally described several years later by Pickering who noted that the presence of particles at an interface between two immiscible phases causes a physical barrier and can lower the systems free energy.[4] Specific system parameters such as particle shape, size, hydrophobicity and specific fluid phases all playing a part in the stability of a given emulsion.[5] While the lay-persons interaction with this phenomenon likely stops at painting their walls, the interest in such systems both scientifically and commercially extends beyond emulsification to include nanostructured materials[6], reconfigurable devices[7], targeted drug delivery[8] and even mineral processing and wastewater treatment.[9]

This thesis studies both the dynamics of solid particles adsorbing to immiscible liquid-liquid interfaces and some of the self-assembly characteristics of such systems, the focus being on the role particle morphology has to play. Advances in particle synthesis over the past decade have enabled the production of ellipsoids[10], cylinders[11], cubes[12] and platelets[13] as well as a variety of more exotic geometries[14–16] on the colloidal length scale. Anisotropic particles have been shown to be particularly effective stabilisers of colloidal emulsions[17] as will be thoroughly detailed in the literature survey in Chapter 2. For the simplest anisotropic geometries such as an ellipsoidal or cylindrical particle adsorbed at the interface, the particle-particle capillary interactions have been reasonably well studied from both theoretical and experimental viewpoints.[18–20] However, the adsorption dynamics, how the particle evolves from being dispersed in one medium to equilibrating at the interface, is an area of active research[21–24] and in order advance the field we require a comprehensive understanding of the adsorption process. A practical consideration to illustrate the importance of a comprehensive understanding of the adsorption process is that morphologies such as cylinders can have multiple stable and meta-stable states.[20,21,25] Many plasmonic sensor applications, sensors utilising spectral shifts from plasmon interactions upon irradiation, require uniformly spaced "forests" of cylinders to be in the upright orientation.[26] In order to reliably reproduce such two-dimensional structures we require control over the factors which result in this state. The adsorption dynamics of anisotropic particles are the topics of Chapters 4 and 5 in which we study ellipsoidal and cylindrical particles respectively.

Particles adsorbed and equilibrated to an interface can interact with one another via different mechanisms, given sufficiently small interparticle separations. In

addition to the steric[27,28] , electrostatic and van der Waals forces[29,30] found in bulk colloidal systems, at the interface colloids also interact via capillary forces.[19,31–33] A common, everyday experience of capillary forces is the Cheerio's effect. The weight of a Cheerio is not enough to overcome the surface tension at the air-liquid interface but it is enough to deform it in such a way that if any other Cheerio's are close enough there appears to be an attraction and the cereal aggregates.[34] Capillary interactions are richer still as they can not only be attractive *and* repulsive but also directional, resulting in the observation and documentation of a wide array of two dimensional crystal structures self-assembled via capillary interactions, far beyond simple particle aggregation.[35–39]

1.2 Practical Motivation

Beyond scientific curiosity there is also much interest in the practical applications of materials formed by the organisation and assembly of colloidal particles. Applying surface coatings or a surface patterning with colloidal particles can modify surface properties such as reflectivity or wetting characteristics.[7] Furthermore, the long-ranged organisation of particles in such coatings gives rise to strong interactions with electromagnetic radiation, an area of interest for plasmonic sensing applications. Colloidal systems have even attracted the interest of researchers trying to attain digital functionalities such as logic gates, switches and data storage. The fluid phase bit being postulated as a solution to data storage on ever smaller length scales, the flipping between stable states under the influence of an external field taking the on the role of current electronic states in memory.[40] From an industrial perspective, the multinational consumer goods corporation Procter & Gamble (P&G) have collaborated with the North American Space Association (NASA) to study phase separation and colloidal stabilisation abord the international space station. P&G

have spent ten million dollars to research colloids under microgravity using the Advanced Colloids Experiments (ACE) platform in the hope of discovering scientific insights which could lead to more efficient and improved product formulations, given that two thirds of P&G's product range consist of such soft-matter systems.[41]

To illustrate how the interfacial self-assembly process is carried out in practice we describe one of the early experiments carried out by Whitesides *et al.*[42] Millimetre scale hexagonal platelets were fabricated from PDMS and selected surfaces coated with tip-ex before exposure to oxygen plasma. The exposed surfaces become hydrophilic under such conditions whereas the tip-ex coated surfaces remain hydrophobic once the tip-ex is removed. The particles are then dispersed at a Hexane – water or water-air interface and the system agitated with an orbital shaker for 24 hours. Changing the geometric configuration of the functionalised facets resulted in a variety of different 2D structures such as open and closed packed lattice configurations. The reason for the rich variety of self-assembled structures is that the shape of the menisci surrounding the particles is altered. We will return to the experiments of Whitesides in more detail in Section 2.3.5.

1.3 Thesis Outline

The aims of this thesis are to theoretically investigate the adsorption dynamics of anisotropic particles at liquid interfaces, and secondly the self-assembly of such particles at a liquid interface. To this end, the rest of the thesis is structured as follows. In Chapter 2 we review the relevant literature applicable to our stated goals starting from fundamental principles pertaining to the adsorption dynamics of isolated, anisotropic particles before reviewing the self-assembly characteristics of such adsorbed particles.

In Chapter 3 we discuss the finite element analysis method used throughout this thesis to analyse the properties of particles adsorbed at the liquid interface – Surface Evolver (SE). Due to the large investment of CPU time required for our calculations of the adsorption dynamics, we also give a detailed discussion on the practicalities and benchmarking which makes these calculations possible.

In Chapter 4 we study the adsorption dynamics of ellipsoidal particles at a liquid-liquid interface, furthermore we compare and contrast our results to existing theoretical and experimental studies.[21,22,43,44] We present a model involving deformation of the liquid meniscus around the adsorbing particle, renormalized friction coefficients and dynamic contact angles to explain both the timescales and the trajectories that are observed experimentally for adsorbing particles.

In Chapter 5 we extend the model presented in Chapter 4 to consider the adsorption kinetics of cylindrical particles which have a variety of aspect ratios and wetting properties. It has been reported both experimentally and theoretically that cylindrical particles can exist in a metastable 'end-on' state.[21,45] In this chapter we seek to use adsorption kinetics to assemble vertically aligned cylindrical nanorods at a liquid interface, with an eye on applications such as plasmonic sensors.

In Chapter 6 we move away from adsorption dynamics and present our results on the self-assembly of anisotropic particles equilibrated at the interface. Specifically, we consider two distinct particle shapes. Firstly, a hexagonal plate with an undulating edge, and secondly a distorted version of the same. The focus of the chapter is to demonstrate the possibility of engineering the self-assembled crystal structure by tuning particle shape alone, as opposed to surface chemistry. Finally, in

Chapter 7 we summarise the conclusions of the thesis and discuss potential future work.

Chapter 2 Theoretical Background and Literature Review

In this chapter we present key findings from the literature and discuss the salient concepts for understanding some of the behaviour of colloids adsorbed at liquid interfaces. We firstly deal with the thermodynamic driving force behind adsorption for a simple isolated sphere before presenting a general discussion of the role particle anisotropy plays in interfacial deformation. In section 2.2 we review the adsorption kinetics of particles at liquid interfaces presenting the experimental and theoretical evidence from the literature. Finally, after having reviewed how a particle adsorbs in the first place, we consider the interactions between them at a particle laden interface and their self-assembly characteristics in section 2.3.

2.1 Isolated Particles at Liquid Interfaces

2.1.1 Spherical Particles

To introduce the subject we start with a simple model of a spherical colloid at a liquid-liquid interface and follow the pioneering approach presented by Pieranski[46], considering the changes in surface energies as the colloid passes from one medium to the other across the fluid interface. Figure 2-1 (*left*) illustrates this situation with a

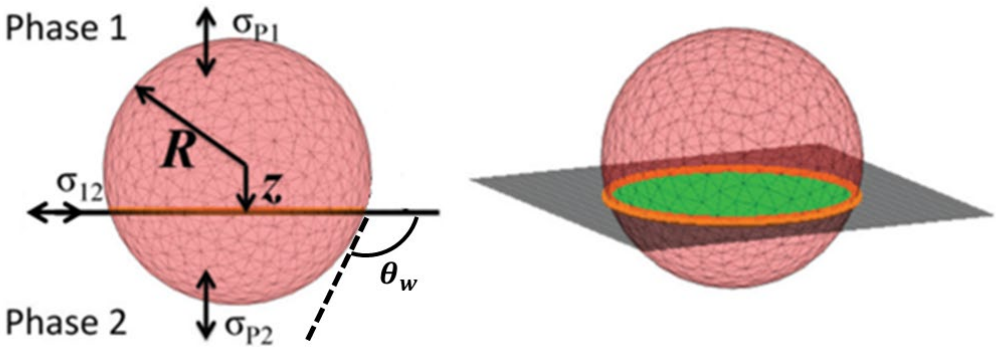

Figure 2-1 (*Left*) Spherical colloid of radius R at height z with respect to the particle center and the planar interface (modified from [47]).Illustrated is the contact angle θ_w alongside the three interfacial tension terms (σ) in which the subscripts 1,2 and P refer to phase 1, phase 2 and the particle phase respectively. (*Right*) Axonometric projection of the area of the fluid interface that is removed upon adsorption of the colloidal particle (green area) and the three-phase contact line (orange line).

spherical colloid of radius R at height z above a planar immiscible interface separating phases one & two. Included are three interfacial tension terms in which the subscripts $1,2$ and P refer to phase 1, phase 2 and the particle phase respectively. Figure 2-1 (*right*) is an axonometric projection showing the interfacial area (*green*) excluded by the presence of the particle along with the three phase contact line highlighted in orange.[47] Consider this particle, which is initially dispersed in the water phase, migrates to, and penetrates the oil-water interface becoming partially wetted by each phase. Henceforth we shall generically refer to phase 1 as oil and phase 2 as water. The spherical particles presence excludes a circular section of the oil-water interface, constituting a negative term with respect to the total interfacial energy and therefore there is a thermodynamic motivator for adsorption.[46] The total interfacial energy in this isolated case can be expressed according to Equation 2-1[21,25,48] as

$$F = A_{op}\gamma_{op} + A_{wp}\gamma_{wp} + A_{ow}\gamma_{ow} \quad \textbf{(2-1)}$$

where A corresponds to the relevant interfacial areas which will be a function of the particle height. Substituting in the relevant area terms then leads to

$$F = 2\pi R^2(1 + z_0)\gamma_{op} + 2\pi R^2(1 - z_0)\gamma_{wp} - \pi R(1 - {z_0}^2)\gamma_{ow} \quad \textbf{(2-2)}$$

where the height of the particle relative to the interface is ($z_0 = z \,/\, R$). Equation 2-2 simplifies to the form

$$F = \pi R^2 \gamma_{ow}\left({z_0}^2 + \frac{2z_0(\gamma_{op}-\gamma_{wp})}{\gamma_{ow}} + \frac{2(\gamma_{op}+\gamma_{wp})}{\gamma_{ow}} - 1\right) \quad \textbf{(2-3)}$$

Differentiation of Equation 2-3 and equating to zero to extract the equilibrium position of the particle with respect to the interface yields a form of the familiar Young's equation

$$z_0^{min} = \frac{\gamma_{wp}-\gamma_{op}}{\gamma_{ow}} \quad \textbf{(2-4)}$$

Unless otherwise stated in all our simulation work presented in chapters four, five and six, we refer to the equilibrium contact angle given by Young's equation

$$\cos\theta_w = \frac{\gamma_{po}-\gamma_{pw}}{\gamma_{ow}} \quad \textbf{(2-5)}$$

As can be seen from Figure 2-2[47], substitution of $-1 \leq z_0 \geq 1$ into Equation 2-3 permits one to estimate the free energy landscape for adsorption in this simplified example. In order to remove the adsorbed particle into either phase it follows that

$$\Delta F_{oil} = F(z_0 = 1) - F\left(z_0 = z_0^{min}\right) \quad \textbf{(2-6)}$$

$$\Delta F_{water} = F(z_0 = -1) - F\left(z_0 = z_0^{min}\right) \quad \textbf{(2-7)}$$

Utilizing Young's equation and expressing the equilibrium configuration in terms of the contact angle θ_w, we get a more widely used expression for the calculation of the attachment energy[1,49–51]

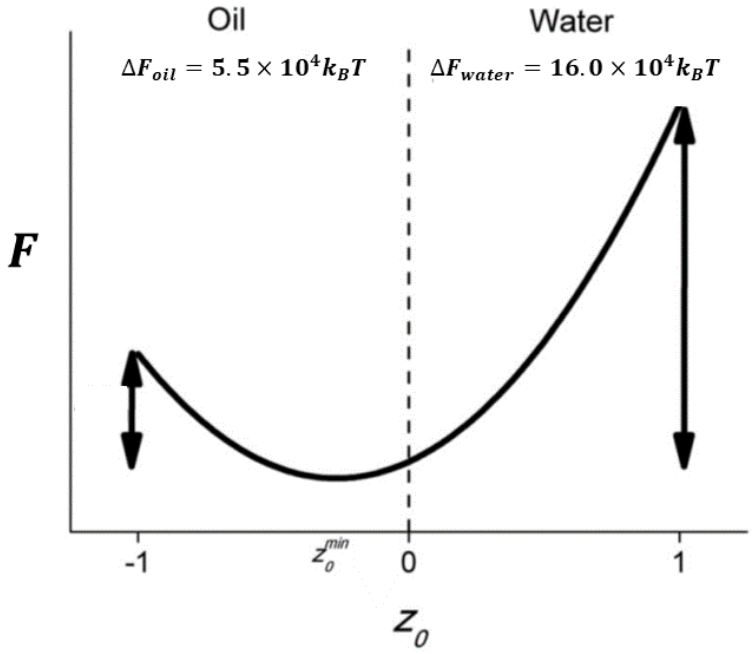

Figure 2-2 Free energy of adsorption as a function of particle height as calculated by Equations 2-6 and 2-7 for a spherical PMMA colloid with radius $R = 50\ nm$ (reproduced from[47]). At $z_0 = -1$ the particle is fully immersed in hexadecane and at $z_0 = +1$ the particle is fully immersed in the water phase. The interfacial tensions used in the calculation are $\sigma_{HD/water} = 53.5\ mNm^{-1}$, $\sigma_{HD/PMMA} = 14.2\ mNm^{-1}$ and $\sigma_{water/PMMA} = 28.5\ mNm^{-1}$.

$$\Delta F = \pi R^2 \gamma_{ow} (1 \pm \cos\theta_w)^2 \quad \textbf{(2-8)}$$

Substituting in typical values for a poly(methyl methacrylate) sphere with a radius of $50nm$ at a hexadecane-water interface where $\sigma_{HD/water} = 53.5\, mNm^{-1}$, the detachment energy is on the order of $10^5 k_b T$.[47] This represents such a large energy barrier that particle adsorption is essentially irreversible.

The contact angle θ_w quantifies the wettability of a surface. Theoretically a solid, liquid and vapor ensemble at a given temperature and pressure have a unique contact angle at equilibrium. We illustrate examples of hydrophilic ($\theta_w < 90°$), neutrally wetting ($\theta_w = 90°$), and hydrophobic ($\theta_w > 90°$) particles in Figure 2-3. In reality however, not only do contact angles vary with physical or chemical defects[52], they also have a hysteresis curve.[53] The contact angle hysteresis can be measured by slowly pumping liquid into or out of a sessile droplet. By placing a needle close to the droplets surface and injecting liquid the drop volume increases, causing the contact angle to increase and eventually reach the advancing contact angle θ_A beyond which, the three-phase contact line will advance. The receding contact angle θ_R being measured in the opposite way[54] with the equilibrium contact θ_A angle being found within this range.

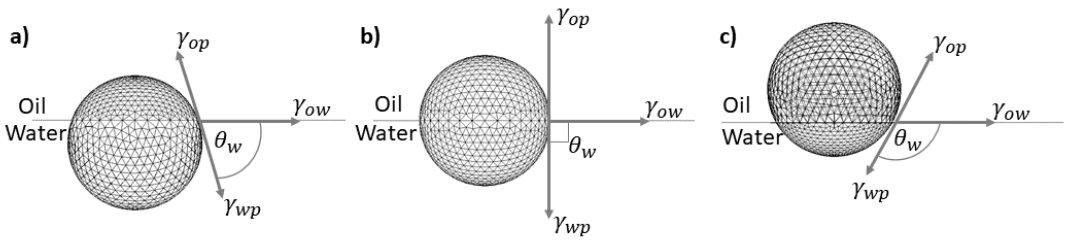

Figure 2-3 Illustration of a spherical particle at an oil-water interface with different contact angles. (a) hydrophilic particle $\theta_w = 70°$, (b) Neutrally wetting particle $\theta_w = 90°$ and (c) a hydrophobic particle $\theta_w = 120°$.

The analysis presented so far restricts the discussion to the effect of the three interfacial tensions on particle position at the liquid interface. Gravitational forces become important for larger sized particles which scale with R^3, whereas surface tension force scales with R.[47,55,56] We can quantify the relative importance of gravity and surface tension via the bond number, $B_0 = {gR^2\Delta\rho}/{\delta_{ow}}$, where g is gravitational acceleration and $\Delta\rho$ the density difference between the phases. It can be shown with typical values of interfacial tension and density that gravity can safely be neglected for $R < 10\mu m$.[56,57] For particles with $R > 10\mu m$ gravity becomes increasingly more important and results in further interesting phenomenon, the most familiar examples of this being the 'Cheerios' effect or the migration of bubbles to the walls of a container. Figure 2-4 (a) illustrates the mechanism of the apparent attraction between bubbles and the walls of a glass container. The air-water interface is distorted by the hydrophilic glass wall resulting in the familiar meniscus effect. The bubble is buoyant and experiences a net upward force F_g, however it is constraint to lie at the interface so moves along and up the meniscus.[34] Figure 2-4 (b) is an image of an upside-down drawing pin floating on

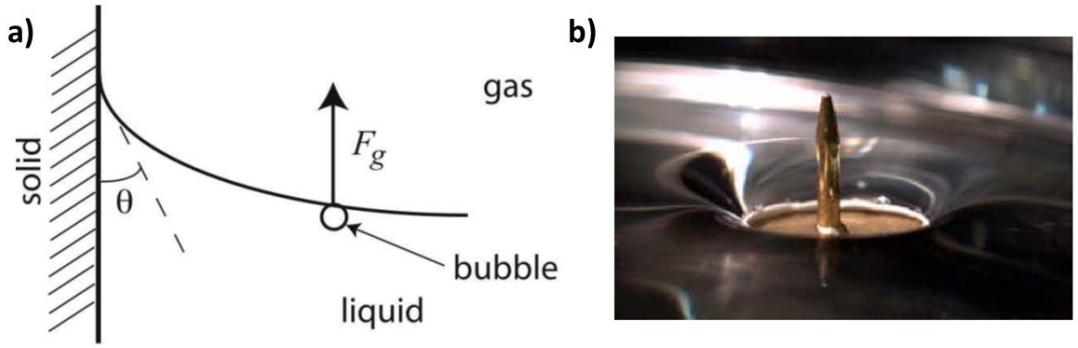

Figure 2-4 Illustrations of interfacial phenomena which can occur when gravity plays a dominant role (reproduced from[34]). (a) The aggregation of bubbles at a solid wall due to being driven up the meniscus curvature due to gravitational force. (b) An image of an upside-down drawing pin floating on water demonstrating the reversal of interfacial curvature, in this case surface tension limits the amount of interfacial deformation permitting the denser than water pin to float.

water, the fact that such a heavy particle can float at all is due to surface tension counterbalancing the weight of the pin. In an analogy to the bubble aggregation, multiple pins will attract when close enough as they "fall down" the interface.[34]

To conclude our discussion of homogeneous, isolated, spherical particles adsorbed at an immiscible interface we introduce the concept of line tension (τ). The imbalance of intermolecular forces in the interfacial region results in surface tension with an energy term *per unit area.*[58] In a similar fashion the three phase contact line has an energy term per unit length known as line tension.[59] Theoretical and experimental results suggest line tension has a magnitude of $1 - 100pN$ and can be positive or negative.[60,61] For neutrally wetting spherical particles, positive line tension tends to reduce the length of the contact line, with particles laying further in favor of their preferred phase shifting the contact angle away from ninety degrees.[47] Furthermore, Positive line tension has been shown theoretically to lead to large energy barriers to adsorption and in some cases, multiple energy minima in the free energy profile. In contrast, negative line tension tends to maximize the length of the contact line with contact angles tending toward neutrally wetting for spherical particles.[47] Line tension, along with Brownian motion sets a lower size limit to the adsorption phenomenon. At the scale of approximately $10nm$ the energy barrier to de-adsorption is on the order of thermal energy[47,62], experimental evidence suggests that below $12nm$ particles can be found dispersed in the bulk.

2.1.2 Anisotropic Particles

For spherical particles Young's constant contact angle constraint can be satisfied simply by a change in the particle height relative to the planar interface. However, for anisotropic particles the system is more complex because the particles have extra

degree(s) of freedom and the liquid interface can deform around the adsorbed particle to satisfy the constant contact angle constraint.[18,20,63]

In order to understand the behaviour of anisotropic particles adsorbed at a liquid interface, we consider the Young-Laplace equation which can be used to describe the shape of the meniscus around an adsorbed particle[64] written in the form

$$\Delta P = \gamma \left(\frac{1}{r_1} + \frac{1}{r_2}\right) \quad \textbf{(2-9)}$$

The left-hand side of Equation 2-9 is the pressure difference between the two bulk phases, γ the surface tension with r_1 and r_2 the principal radii of curvature at any given point on the meniscus. For small deformations the curvature can be approximated by $\left(\frac{1}{r_1} + \frac{1}{r_2}\right) \approx \nabla^2 h$ where ∇^2 is the 2D Laplacian operator and is defined as $\nabla^2 = \frac{\partial^2}{\partial x^2} + \frac{\partial^2}{\partial y^2}$ in Cartesian coordinates and h is the height of the meniscus.[65] Far from the particle the meniscus is flat therefore $\Delta P = 0$, continuing under the assumption of low bond number the interfacial deformation obeys the 2D Laplace equation

$$\nabla^2 h = 0 \quad \textbf{(2-10)}$$

The general solution in circular polar coordinates for a particle centered at the origin is a superposition of multipoles of the form[64]

$$h(r,\theta) = A_0 ln(r) + \sum_n \frac{A_n}{r^n} \cos n\theta + \alpha_n \quad \textbf{(2-11)}$$

In this expansion the subsequent terms are referred to as the polar monopole, dipole, quadrupole, hexapole etc., with A_n and α_n referring to the amplitude of the interface and phase angles respectively. Different leading order modes are activated depending on the particle shape, external forces and/or torques acting on the particle which will be discussed in the following.

In the presence of a vertical force such as gravity acting on an adsorbed particle the interface will deform until the capillary force balances the external force.[34] The equilibrium expression in the small slope limit is[65]

$$F_{ext} = \gamma \oint \nabla h \cdot \vec{\boldsymbol{m}}\, dl \qquad \textbf{(2-12)}$$

Equation 2-12 describes the balance of a vertical force from capillary deformation, the right-hand side, with an external force on the left-hand side. Integrating along the contact line where $\vec{\boldsymbol{m}}$ is the normal of the undisturbed interface and the other symbols are defined as before. The only term in the multipolar expansion in Equation 2-11 which contributes to the right hand side of Equation 2-12 is the monopolar term, $A_0 ln(r)$. However, in the absence of any externally applied fields and for particles with sizes less than $10\mu m$, $F_{ext} = 0$ meaning that the monopolar term is also zero as discussed in section 2.1.1.[56,57] The next term of the multipolar expansion in Equation 2-11 which describes the shape of the meniscus is the dipole which we will discuss as follows.

The dipole mode only occurs in the presence of an external torque acting upon a particle.[65] This can be seen by recognizing the form it takes in Equation 2-11 is essentially $\cos\theta$, resulting in a maximum interfacial elevation at $\theta = 0$ and depression at $\theta = \pi$ as illustrated in Figure 2-5.[65] Some interesting studies have shown that applying a magnetic field on ellipsoidal particles with an embedded magnetic dipole

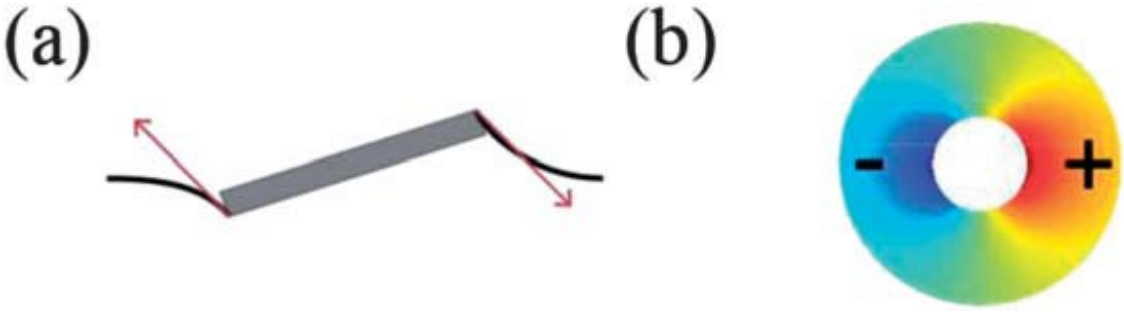

Figure 2-5 Illustration of a dipole induced by the presence of an external torque acting on a particle (reproduced from[65]). (a) Planar view of the interfacial rise and depression at the tips of a cylindrical particle. (b) Birds eye view of iso-height contour of the interface with the blue (negative sign) representing the interfacial depression and red the interfacial elevation.

causes an external torque on the particles, perturbing them from their equilibrium position resulting in switchable dipolar capillary interactions.[66] In the absence of an external field to cause this torque the dipolar term is also zero. Thus, the leading order capillary multipole which describes the meniscus shape in Equation 2-11 for low bond number anisotropic particles is the quadrupole.

Small, anisotropic, chemically homogenous particles under no external field result in the leading term of the interfacial deformation being the quadrupole.[19,20,36,65] The origin of this phenomenon is that the three phase contact line obeys Young's constant contact angle requirement. In the case of a three phase contact line moving freely over the surface of smooth particle, it must intersect the particle with a uniform contact angle at equilibrium else there will be a force imbalance.[65] Consider a neutrally wetting ellipsoid (i.e., $\theta_w = 90°$), the interface need not deform if the particle center is in plane with the interface as the constant contact angle requirement is satisfied. However, any deviation from $\theta_w = 90°$ results in the interface deforming, potentially also alongside a shift in the particle height relative to the interface. The quadrupolar

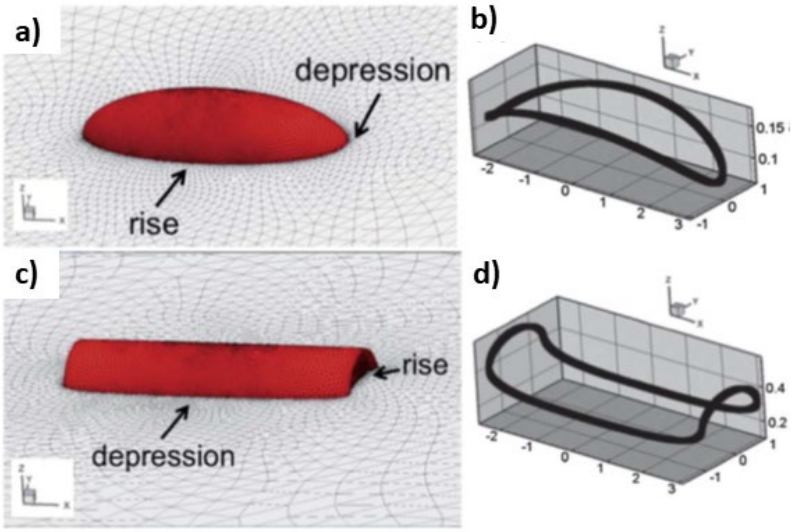

Figure 2-6 (a) Perspective views of an isolated ellipsoid (a) and cylinder (c) adsorbed at an interface and their corresponding interfacial deformations (reproduced from[36]). Also shown are the contact line profiles (b & d) with the height values normalised and expressed in units of the particle semi minor axis.

deformation is illustrated in Figure 2-6[36] for a hydrophilic ellipsoid (a) and cylinder (c) at an oil-water interface. The coordinates of the three phase contact lines are plotted in (b) and (d) for the ellipsoid and cylinder respectively. The quadrupolar deformation surrounding the cylindrical particle is much more concentrated around the flat ends due to the increased curvature of the particle at the tips. The distorted quadrupole, or concentration of contact line deformation, has been characterized for cylindrical particles both experimentally[18,20] and through simulation.[36,67] This subtle difference in the meniscus shape between ellipsoidal and cylindrical particles has a marked effect on the capillary interactions at particle laden interfaces. Cylindrical particles approach tip to tip and form linear chains, whereas ellipsoids approach in the same manner before rolling around each other and assembling side to side.[20,36] The physical justification for this effect is that the concentration of contact line deformation at the tips of the cylindrical particles effectively introduces higher order multipoles in the nearfield. We also note that as illustrated in Figure 2-6 for hydrophilic particles, the interface is depressed at the tips and rises along the sides of the ellipsoid whereas for the cylinders a capillary rise is on the ends and depression occurs along the sides.[20,36] For hydrophobic particles the signs of curvature are reversed in each case.

The equilibrium configuration for ellipsoidal particles is lying flat at the interface, however for cylinders it can take other states depending on the aspect ratio, $\alpha = {}^{L}/_{2r}$, where L is the length of the particle and r the radius.[57] For $\alpha > 2$ the particles lie flat at the interface like ellipsoids[25,36], however a metastable state also exists with the cylinders stood upright at the interface.[21] For $\alpha < 2$ a tilted states exist in which the leading order mode is a hexapole.[25] Shrinking the aspect ratio further such that the cylinder more closely resembles a disc results in the 'upright' state becoming the equilibrium orientation.

Higher order multipoles, such as the hexapole surrounding lower aspect ratio cylinders can also be found for more exotic colloidal shapes. For example, cubic particles, which have an extra degree of freedom when compared to cylinders because their height and two orientational angles can all vary. This results in three possible stable configurations depending on the specific system parameters.[39,63,68] We discuss the orientation, meniscus deformations and self-assembly characteristics of cubic particles in more detail in section 2.3.3. Improvements in particle synthesis techniques[10,16,39,69] have enabled further study into the effects of anisotropy in the form of Janus particles. Janus particles can be spherical or anisotropic particles with two different surface chemistries and hence two different contact angles.[69] Any detailed discussion of Janus particles is beyond the scope of this thesis but we note that the introduction of changes in the contact line further complicates interfacial deformations. Furthermore, Janus particles can have orientational preferences in the self-assembly process, a phenomenon we try to exploit in Chapter 6 albeit through morphology alone.

2.2 Adsorption Kinetics of Particles at Liquid Interfaces

2.2.1 Adsorption of Spheres

Having discussed the behaviour of isolated particles equilibrated with the interface we now consider the adsorption process itself. Specifically, the dynamics that occur when a colloid attaches to the interface and relaxes to its energetically preferred configuration. Nearly all theoretical models of capillary interactions assume that the particles have reached their equilibrium orientation at the interface.[36,63,64] The motivation for this assumption being the huge reduction in surface energy that occurs with binding and maximising the excluded interfacial area as discussed in section 2.1. Surface roughness of a particle results in a large increase of surface area in contact with

each phase and its importance will become clear when we consider the experimental timescales discussed in the next paragraph. We illustrate some of the effects of surface roughness in Figure 2-7[47] which shows that it has a negligible effect on the interfacial area removed by the presence of the particle but the surface area in contact with each of the phases, and also the length three phase contact line is significantly increased (orange line). In general, a water droplet on, for example, a hydrophobic surface can experience two different states. The Wenzel state is one in which the liquid follows all the contours of the surface and to paraphrase Wenzel, in the case of a spreading droplet, for an identical increase in the upper surface of the drop there is a much greater surface area underneath the drop which is wetted if the underlying surface is rough than if it were smooth.[70] Referring back to Equation 2-1, such an effect clearly alters either the A_{wp} term or the A_{op} depending on the specifics of the system under consideration. In

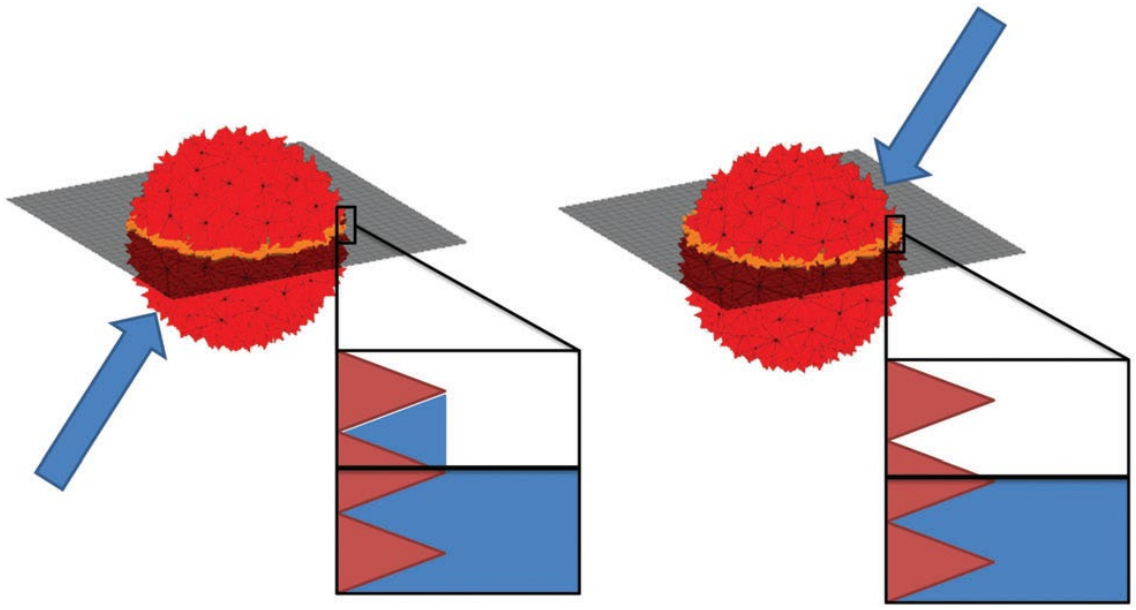

Figure 2-7 Illustration of the effect of surface roughness on a non-neutrally wetting spherical particle (reproduced from[47]). The particle preferentially wets the lower phase (blue) and here we illustrate Cassie Baxter type wetting *(left*) in which the fluid in the gaps is not replaced as the particle adsorbs from the lower phase. (*right*) The particle adsorbs from the upper phase and the 'holes' are replaced with the blue phase and the particle has Wenzel type wetting.

contrast, Cassie-Baxter wetting describes an incomplete wetting state in which a droplet is suspended on a composite surface of both material and air pockets.[71]

Nonomura *et al.*[72–74] considered the theoretical behaviour of both Wenzel and Cassie-Baxter type wetting on rough surfaced, non-neutrally wetting particles, illustrated in Figure 2-7. In the case of Cassie-Baxter type wetting, the particle adsorbs from the energetically favorable phase and the surface defects are fully wetted by this phase. In the case of Wenzel wetting, the particle adsorbs from the non-energetically favorable phase and the surface defects are filled with the energetically favorable phase. In both cases, Nonomura *et al.* showed that the presence of surface roughness increases the natural wettability of the particles.

In an elegant set of experiments Kaz *et al.* used holographic microscopy to study the adsorption process of polystyrene spheres at a decane-water interface, shown in Figure 2-8.[20] Guiding the particle to the interface with the use of an optical trap the group found the surprising result that after an initial, almost instantaneous breach of the interface, the particle trajectories are logarithmic in time. Furthermore, the velocity and capillary numbers measured, were three orders of magnitude smaller than expected from models based on viscous dissipation.[75–77] Finally, it was found that even after 100 seconds the systems were far from equilibrium having an apparent contact angle of $75°$, yet when measured with other methods the equilibrium contact angle for such systems is reportedly $110°$.[78] In order to explain these results the group proposed a theoretical model based on molecular dissipation using the Arrhenius equation

$$V = V_0 exp\left(\frac{-U}{kT} + \frac{FA}{2kT}\right) \qquad \textbf{(2-13)}$$

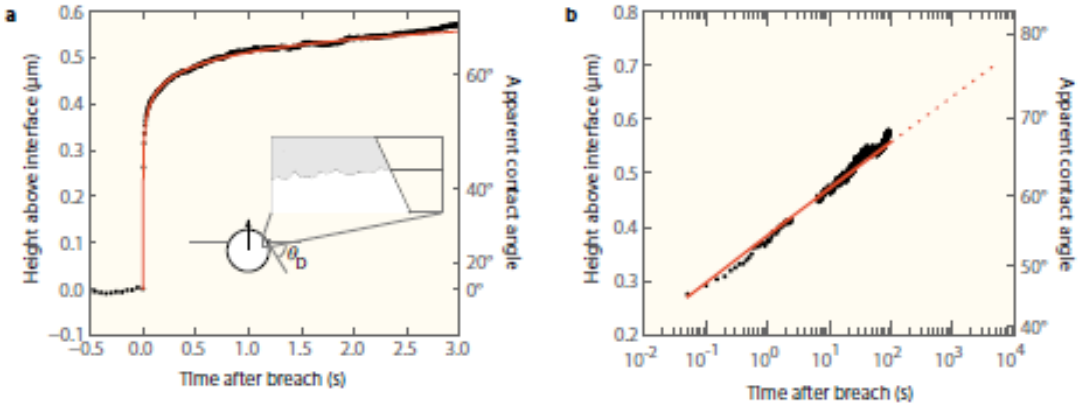

Figure 2-8 (a) Relaxation data from an adsorbing spherical particle and (b) log plot of the same, alongside a best fit from the dynamic wetting model (see text), reproduced from[20]. Clearly a rapid, almost instantaneous breach of the interface followed by logarithmically slow relaxation time.

In Equation 2-13, V is the average velocity of the contact line as it hops from one pinning site to the next. Defects can be due to surface roughness as illustrated in Figure 2-7 or heterogeneities in surface chemistry. Therefore, Equation 2-13 equates the velocity of the contact line with a Boltzmann factor representing the probability of the contact line hopping over a defect. For the contact line to hop from one defect of area A to the next, it must overcome the energy barrier U. Finally, V_0 is a molecular velocity and F is the force per unit length acting on the contact line and is due to the unbalanced surface tension forces at the three phase contact line. This thermally activated hopping model of the contact line passing over surface heterogeneities or physical defects[79] (red line in Figure 2-8) successfully models the experimental results of an adsorbing spherical particle. This contact line hopping model will be considered further in Chapter 4.

2.2.2 Adsorption of Anisotropic Particles

Due to the relative ease of fabricating spherical sub-micron particles as well as their straight-forward mathematical description, it is unsurprising that most of the research has focused on this area. However, increasing attention has been devoted to the effect particle morphology has on adsorption. The adsorption of anisotropic

particles is more complicated because anisotropic particles can potentially adopt multiple stable configurations, resulting in complex free energy landscapes for the adsorption process.[17,21,57,80–83] Despite active research in this area, the dynamics of adsorption for anisotropic particles is still poorly understood, with disagreement between available theoretical and experimental results.[21,23,43,84]

To our knowledge the first theoretical investigation into adsorption of ellipsoids was carried out by de Graaf *et al.* using a triangular tessellation simulation technique.[57] The underpinning idea behind their method was to use the tessellation technique for an ellipsoid to generate a free energy landscape as a function of particle orientation and height with respect to the planar interface. They then used a simplified Langevin dynamics model to determine possible trajectories after the initial breach, leading to the final equilibrium orientation where the ellipsoids semi-major axis is parallel with the

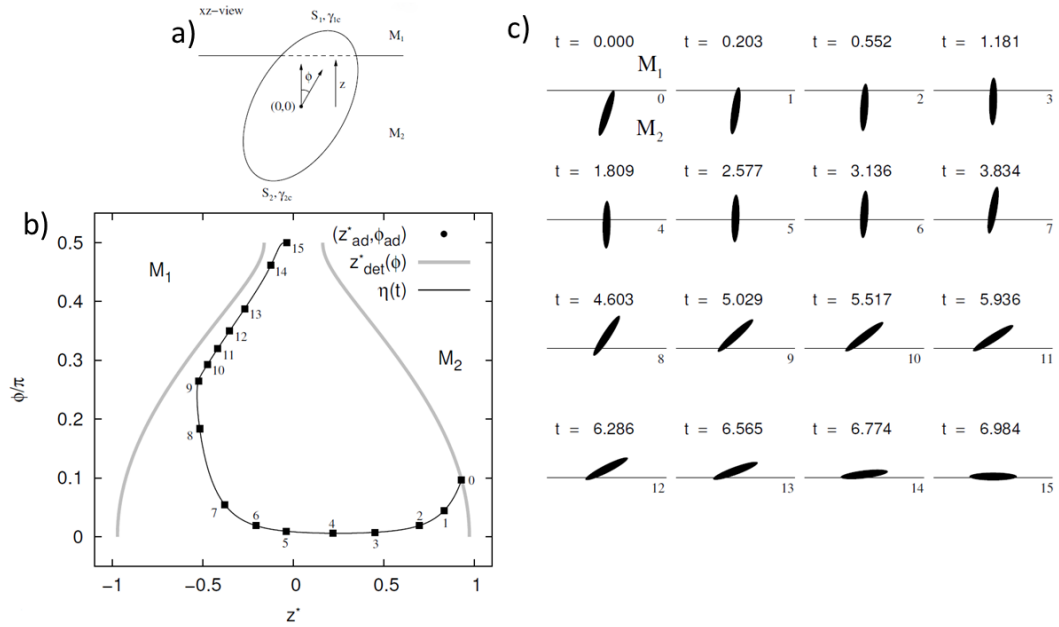

Figure 2-9 Reproduced from[21], (a) Definition of particle hight (z) relative to the undisturbed planar interface and particle tilt angle (ϕ) with respect to the interfacial normal. (b) An adsorption trajectory of a neutrally wetting ellipsoid with aspect ratio of 6. $\eta(t)$ Shows the trajectory starting from medium 2 (M_2) and terminating at $\phi/\pi = 0.5$ and z*=0. Finally, the $z^*_{det}(\phi)$ lines are the heights at which the particle just contacts the interface and are normalised such that $z^* = \frac{z}{\sqrt{a^2+2b^2}}$ where a and b are the semi-major and semi-minor axis of the ellipsoid respectively. (c) Snap shots of the evolution in time of the adsorbing ellipsoid from (b).

interfacial plane. This quasi-static model included the effects of line and surface tension but neglected electrostatic effects and interfacial deformation.[21]

As illustrated by Figure 2-9, the authors reported that the adsorption dynamics was a two-step process. Following the initial breach (Figure 2-9 (b) and (c) (t = 0.000)), the ellipsoid passes vertically through the interface to its peak height (points (1)-(9)), then rotates into its minimum energy configuration (points (10)-(15)), in summary a translational step followed by a rotational step.[21] The adsorption process is represented by a phase plane diagram (Figure 2-9 (b)), the x coordinate representing the centre of the particles height above/below the flat interface (z^*) and the y coordinate representing the tilt angle (ϕ) of the ellipsoids semi-major axis relative to the normal of the flat interface, as defined in Figure 2-9 (a). The two light grey lines in Figure 2-9 (b) labelled $z^*_{det}(\phi)$ in the legend are the configurations where the particle initially contacts the flat interface. This phase plane representation will be discussed in more detail in Chapter 4. Interestingly, most particle trajectories simulated by the group vary non-monotonically, first reducing then increasing in tilt angle into their equilibrated configuration (as seen in Figure 2-9 (b)). The timescale of the adsorbing particle to equilibrate with the interface being predicted to be between 10^{-1} s and 1s for typical micron sized particles.[21] The method de Graaf *et al.* used was intended as a steppingstone to more elaborate models which would include electrostatic and interfacial deformation effects.

A more physically realistic theoretical study of adsorption dynamics was presented somewhat later by Günther *et al.* in 2014.[22] The group combine multicomponent lattice Boltzmann (LB) simulations[85] and molecular dynamics to study the adsorption trajectories and timescales of ellipsoidal particles. Using the LB extension introduced by Shan and Chen[86] they produced a model incorporating inertia, an inter particle potential and hydrodynamic effects, implicitly permitting interfacial deformation. The results are qualitatively similar to those reported by de Graaf *et al.*, in the sense that they also predict trajectories with non-monotonic variation of particle angle (Figure 2-10). For clarity we note that the authors use different symbols to represent tilt angle (ϑ in degrees in place of ϕ/π in radians) and particle height (ξ in place of z^*) with respect to the phase plane diagrams presented by de Graaf but both are equivalent. Almost all trajectories (dashed lines) end in the equilibrium tilt angle of

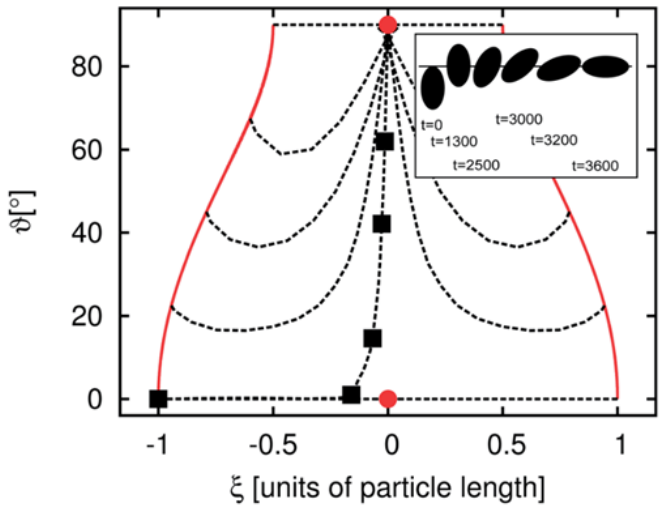

Figure 2-10 Adsorption trajectories (dashed lines) for a neutrally wetting ellipsoid ($\theta_w = 90°$) with an aspect ratio $m = 2$,obtained from LB simulations (reproduced from[22]). The red lines are the heights at which the particle just contacts the interface and are normalised in the same manner as Figure 2-9 with the y axis being expressed in degrees as opposed to radians. The authors use different symbols to represent tilt angle (ϑ in degrees in place of ϕ/π in radians) and particle height (ξ in place of z^*) with respect to the phase plane diagrams presented by de Graaf *et al.* but both are equivalent. The black squares correspond to the configuration illustrated in the inset and the red dots denote the stable (top) and meta-stable (bottom) points.

$\vartheta = 90°$, with the particle tilt angle initially moving in the 'wrong' direction, in agreement with the findings of de Graaf *et al*.[21]

The adsorption dynamics of ellipsoidal particles has more recently been studied experimentally by a number of groups. Using a digital holography technique[87] Wang *et al.* studied micron-scale functionalized polystyrene (PS) ellipsoids as they were guided by an optical trap to the interface between a decane phase and a water phase containing glycerol and salt.[23] It is reported that the force from the optical trap, less than $1pN$, is too weak to bend the interface beyond several tenths of a nano-meter.[88] The advantage of using the digital holography technique (Figure 2-11 (a-b)) is that it enables one to simultaneous recover both the particle height (Figure 2-11 (c)) *and* tilt angle (Figure 2-11 (e)) as it adsorbs over time. The experiments show that the timescales for the adsorption process were five orders of magnitude longer than predictions from simulations [21,22], consistent with the results for the spherical particles[89] discussed in section 2.2.1. Furthermore, monotonic trajectories were reported in which the particles

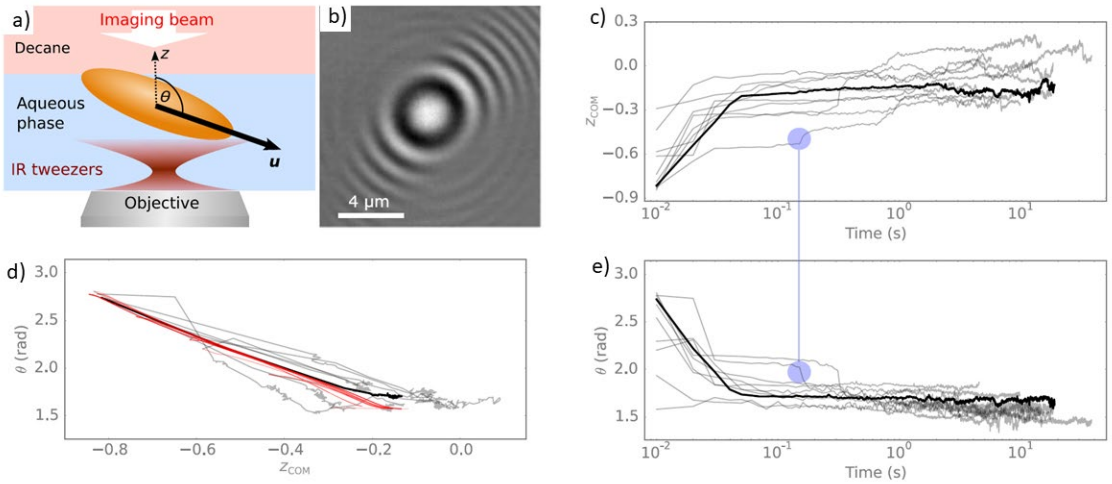

Figure 2-11 (a) Illustration of the experimentle set up in which a particle is guided to the interface by optical tweezers while the imaging beam illuminates the sample from above and generates the holograms required (b) (reproduced from[23]). (c) The evoloution the the particle center of mass height (z_{com}) relative to the interface over time, the bold black line represents the average of the individual trajectories (grey lines) (d) Particle tilt angle θ (rad) vs the particle center of mass height, the red line is the prediction from a thermally activated contact line hopping model. (e) The evolution of tilt angle over time.

'rolled' into position, i.e., the height and angle are coupled and the two-stage translation-rotation predicted by simulations were not observed (Figure 2-11 (c - e)). The authors concluded that the adsorption process is not dominated solely by viscous dissipation, but contact line pinning also plays a significant role.[23]

The logarithmic relaxation times reported for PS spherical and ellipsoidal particles has also been reported for particles of different compositions and surface functionalities. For certain polymeric particles dispersed in water the energy barrier from pinning effects at surface heterogeneities has been reportedly measured as being an order of magnitude higher than for other particles, such as oil dispersed PMMA and small silica particles, which have resulted in even longer relaxation times.[90] We note that the unexpectedly slow movement of the contact line has been reported in fields of similar study such as the physical aging of spreading droplets[91] or the unexpectedly slow lateral diffusion of adsorbed particles.[92]

The adsorption dynamics of anisotropic particles has also been studied experimentally by Coertjens *et al.*[24] Using freeze-fracture shadow casting cryo-SEM[93,94] and measuring the evolution of the particle tilt angle via high speed confocal microscopy, the group studied model ellipsoidal particles as they breached the interface. Polystyrene ellipsoids with an aspect ratio of $m = 4$ were fabricated using the stretching method[10] and allowed to migrate to a decane-glycerine/water interface via a buoyancy force from a slight density mismatch between the particles and sub-phase.[24] Unfortunately the methodology employed by Coertjens *et al.* is only able to accurately capture the evolution of particle tilt angle, not the particle centre of mass height with respect to the interface. Consistent with the findings of Wang *et al.* these experiments reported significantly longer adsorption timescales than that predicted by simulation. However,

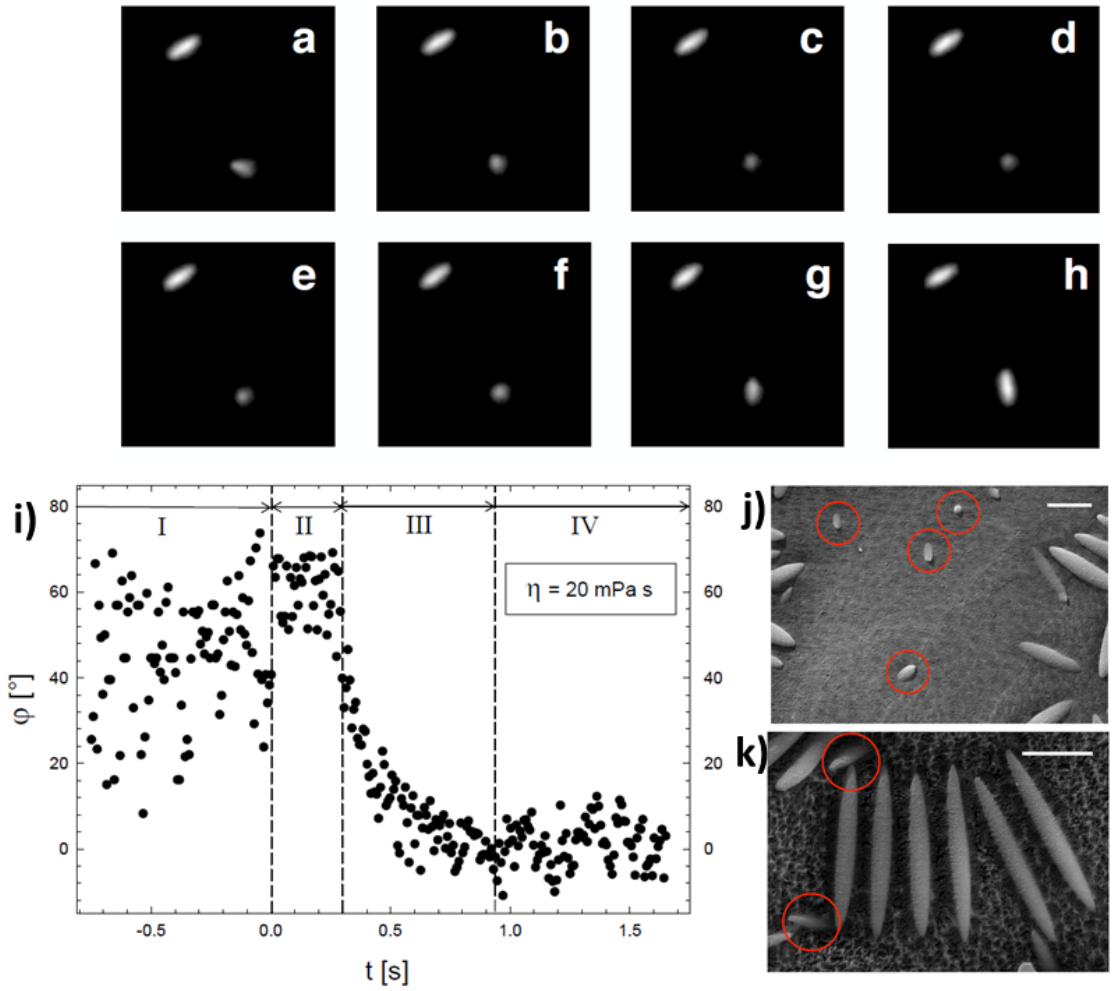

Figure 2-12 (a-h) Image sequence of an adsorbing particle (lower right of frame) occurring over the course of approximately one second (Reproduced from[24]). (i) Tilt angle versus time measurements for adsorbing particles, divided into four distinguishable stages: (I) free diffusion, (II) vertical penetration, (III) rotation and (IV) fully adsorbed. Cryo-SEM images of particles in the process of adsorption (circled) for aspect ratios of four (j) and six (k).

in contrast to Wang *et al.,* they found an initial constant angle phase as the particle translates through the interface followed by a rotation phase, consistent with some of the features of simulations[21,22] (Figure 2-12 (a-i)). Furthermore, while the timescales reported were longer compared to the afore mentioned simulations, it was much shorter compared to the experiments of Wang *et al.*

Given the wide range of initial attack angles present in Figures 2-11 & 2-12 alongside the effect of different initial attack angles predicted by simulations in Figures 2-9 & 2-10, the question arises, is the initial attack angle truly random? Coertjens *et al.*

[24] undertook a three-dimensional tracking of the ellipsoidal particles on their migration to the interface in the same set of experiments discussed above. The group found that as the particle traverses the bulk it assumes a random walk with a preferred translation direction according to its long axis. Furthermore, when the initial attack angles are analysed as a function of the ellipsoid's aspect ratio, in almost all cases the initial attack angle was found over the $35 - 60°$ range. This is consistent with the large spread of initial attack angles observed in Figure 2-11 (e) and Figure 2-12 (i). To our knowledge this is the only such study for such experimental systems.

In summation, recent experimental studies of ellipsoidal adsorption trajectories are at odds with those predicted by simulations in both timescale and spatial evolution. Furthermore, there are also discrepancies between experiments, one set suggesting that contact line pinning effects dominate the adsorption process, another suggesting capillarity plays a large role and mirroring the two-step process predicted by simulation. This subject is the focus of Chapter 4 in which we present a model which attempts to unify some of the discrepancies between experiments and theory.

2.3 Capillary Interaction and Self-Assembly of Particles at Liquid Interfaces

2.3.1 Spheres

Having discussed the adsorption process itself we now discuss what happens after particles have completed the adsorption process and equilibrated at the interface. Specifically, we discuss the capillary forces between particles arising from interfacial deformation and the role that particle morphology plays.

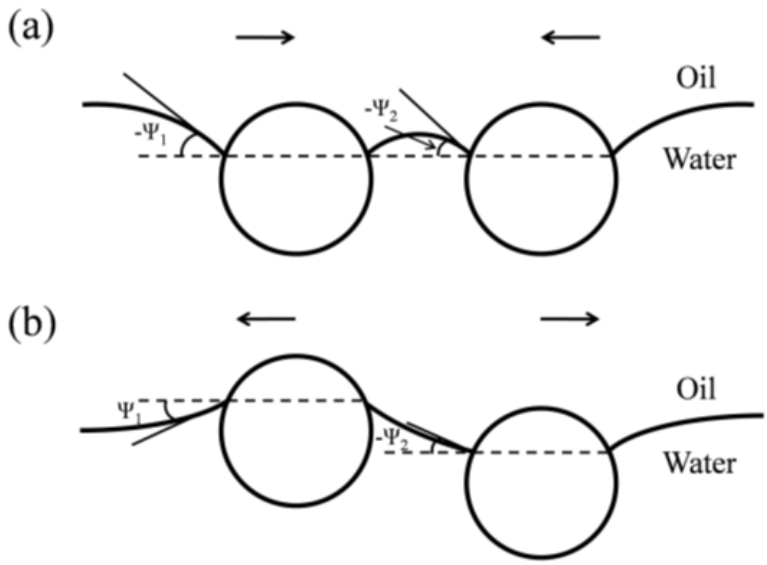

Figure 2-13 An illustration of floatation forces for two spherical particles adsorbed at an oil-water interface (reproduced from[31]). Each particle has meniscus slope angles denoted by $\psi_1$and ψ_2 and interaction is attractive (a) when the sign of the slope angles is the same, repulsive (b) when the signs are opposite.

We start by considering the lateral capillary force between two perfectly smooth spherical particles with a high bond number such that a monopolar interfacial deformation is present due to gravity. Referred to as floatation forces, these lateral capillary forces arise between adsorbed particles when their interfacial deformations overlap.[31,56,95] The floatation forces can be attractive (Figure 2-13 (a)) or repulsive (Figure 2-13 (b)) and this is determined by the sign of the meniscus slope angles $\psi_1$and ψ_2. The capillary force is attractive if $\sin\psi_1 \sin\psi_2 > 0$ and repulsive if $\sin\psi_1 \sin\psi_2 < 0$. The Cheerio's effect, discussed in section 2.1.1, is good example of this phenomena and perhaps unsurprisingly, as the size of the interfacial deformation grows so too does the strength and range of the capillary forces.[31] Conversely, as the scale and weight of the colloidal particles decreases so too does the monopolar deformation and therefore the floatation force. Once these forces become negligible, the interfacial deformations and the interactions between them are dependent higher order multipoles which we discuss in the following section.

2.3.2 Ellipsoids and Cylinders

As discussed in section 2.1.2 the leading order deformation for ellipsoids and cylindrical particles is the quadrupole. We define the rotational orientation of the two quadrupoles as illustrated in Figure 2-14[32] viewed from the top down. The positive and negative signs represent interfacial rises and depressions with respect to planarity and the particle centre to centre separation is denoted by L. The interaction energy between the two quadrupoles in the far field was derived by Stamou *et al.*[64] as

$$\Delta W(L) \approx -12\pi\sigma H^2 \cos(2\varphi_A - 2\varphi_B)\frac{r_c^4}{L^4} \quad \textbf{(2-14)}$$

where the coefficients H and σ denote the height of the meniscus at the contact line and surface tension respectively with r_c the contact radius. We focus on the cosine term of Equation 2-14 as it controls the magnitude and sign of the interaction energy given that $-1 \leq \cos(2\varphi_A - 2\varphi_B) \leq 1$ as will be discussed in the following.

To visually illustrate two interacting quadrupoles, Figure 2-15[33] is a contour plot of the meniscus height for two generic quadrupolar deformations. All units are normalised with respect to the generic particle's radius r and we define their phase angle as in Figure 2-14. It costs energy to deform an interface, however this energy cost

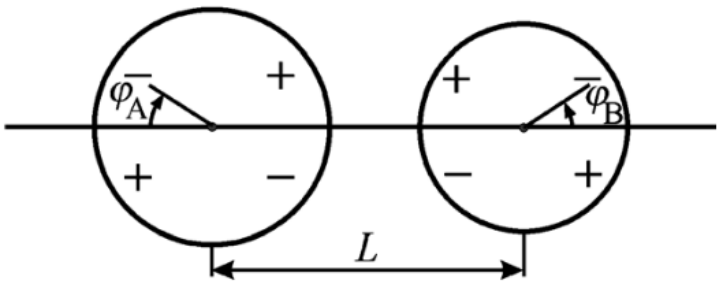

Figure 2-14 Top-down sketch of rotational orientations of generic quadrupoles A and B with centre to centre separation L (reproduced from[32]). Positive and negative signs represent a meniscus rise or depression with respect to planarity respectively.

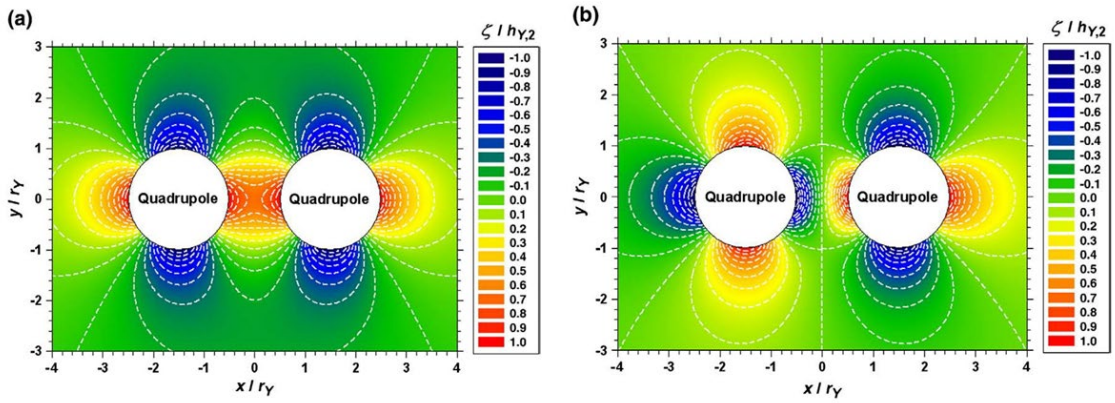

Figure 2-15 Contour plot of two similar interacting quadrupoles in an (a) attractive configuration with a respective phase shift of zero or equivalently π, and (b) repulsive configuration with a respect phase shift of $^{\pi}/_{2}$ or equivalently $^{3\pi}/_{2}$ (reproduced from[33]). All units are normalised and expressed in terms of particle radius r with red indicating an interfacial rise, green a flat interface and blue an interfacial depression.

can be minimised by overlapping deformations of the same signed curvature which manifests as attractive, repulsive and rotational forces on the particles. Figure 2-15 (a) Illustrates the overlapping interfacial rises in red for $\varphi_A = \varphi_B = 0$, equivalent to $\varphi_A = \varphi_B = \pi$ and also occurs for overlapping depression $\varphi_A = {}^{\pi}/_{2}$, $\varphi_B = -{}^{\pi}/_{2}$ alongside all symmetric variations. This snapshot in time of the interface shape results in an attraction between the two quadrupoles which pulls the two into contact, as shown experimentally in Figure 2-16 (a). Conversely two particles with opposite signs of interfacial curvature, as in 2-15 (b), is the least energetically favourable and yields a repulsion/rotation.[20]

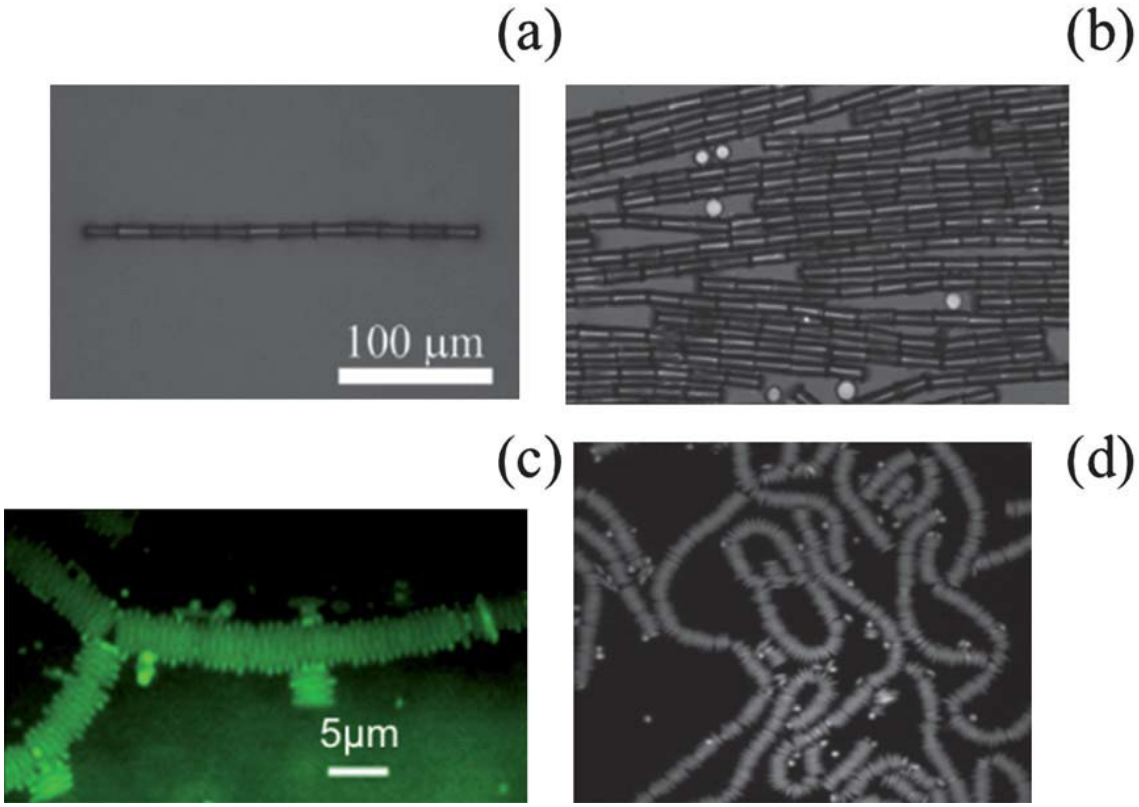

Figure 2-16 (a) Linear chain of cylindrical particles self-assembled tip to tip at an air-water interface and (b) the resulting monolayer that forms after interface compression. (c) Chains of ellipsoidal particle assembled side to side at an oil-water interface and (d) monolayers of the same (composite from [20,36,96]).

The far field behaviour of both cylinders and ellipsoids is very similar due to both particles having a quadrupolar leading order mode.[36] We note here that we refer to the far field as the particle separation where only the leading order multipole capillary interaction is relevant whereas the near field is the particle separation where higher order multipoles become relevant to the capillary interactions. A separation on the order of a single particle radii is generally speaking sufficient for nearfield effects to start to play a larger role in the interaction. In the nearfield regime the specific details of particle geometry start to become important and play a leading role in determining how the different particles self-assemble. Figure 2-16[20,36,96] illustrates experimentally the difference in behaviour between ellipsoids and cylinders and the microstructures they self-assemble too when adsorbed at the interface. For sparsely covered interfaces, cylindrical colloids assemble tip to tip in linear chains, Figure- 2-16 (a). The chains of

cylinders remain relatively straight in denser systems which can arise as a result of interface compression as in Figure 2-16 (b). In contrast the ellipsoidal particles in at an oil-air or oil-water interface (Figures 2-16 (c) and (d) respectively) rotate about each other assembling in a side to side configuration forming highly curved, sprawling chains.

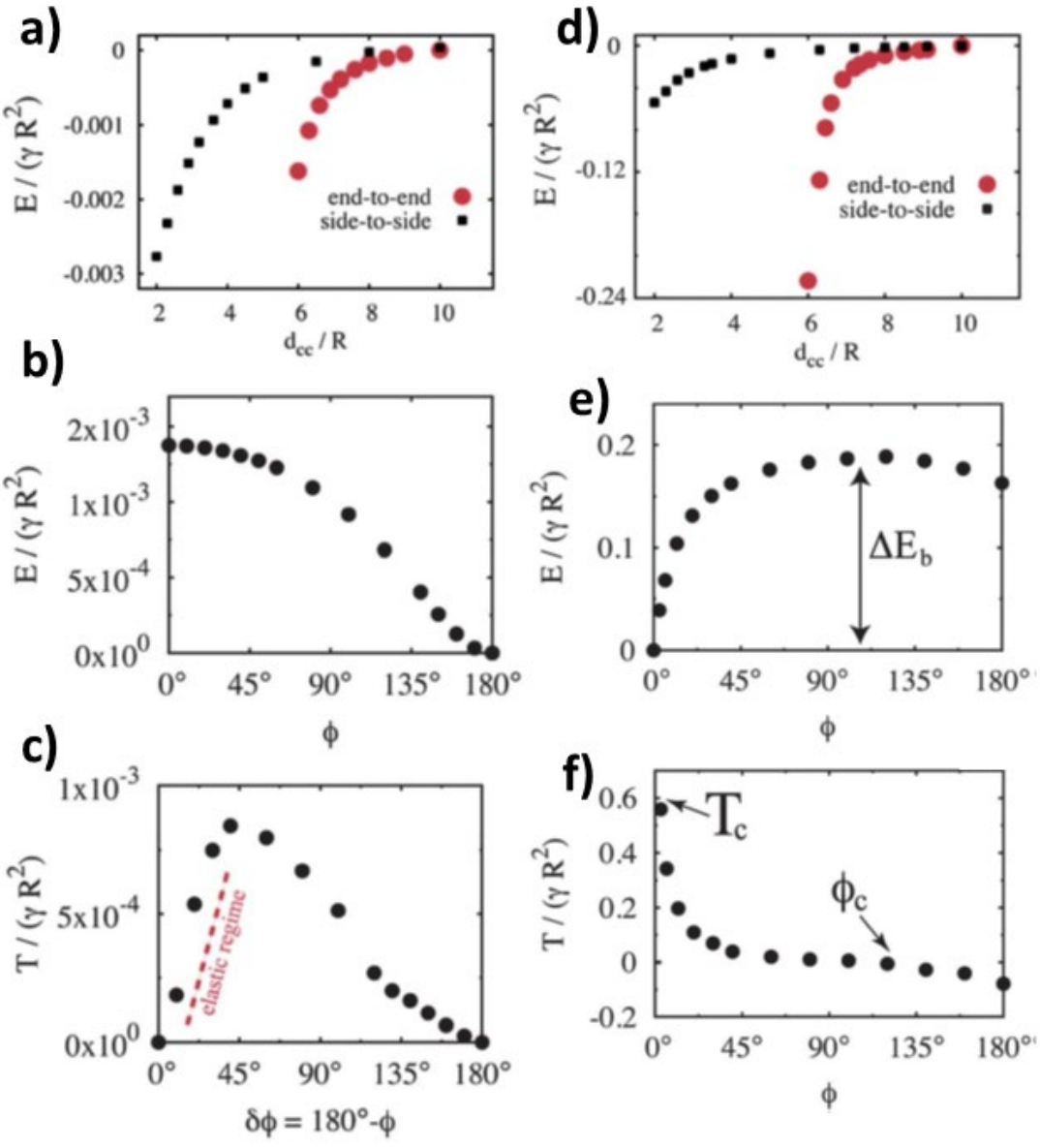

Figure 2-17 Normalised capillary energy as a function of centre to centre separation d for ellipsoids (a) and cylinders (d), the reference energy is for $d = 10r$ (reproduced from[36]). Normalised capillary energy as a function of bond angle ϕ, for two ellipsoids (b) and two cylinders (e) in contact. The final row is the capillary torque as a function of angular deviation away from the global energy minimum, the side-to-side case for ellipsoids (c) and end to end case for cylinders (f). Both ellipsoids and cylinders have an aspect ratio of three and contact angle of eighty.

To explain the above difference, Botto *et al.* studied the interactions between rod-like particles theoretically and found the presence of edges on the cylinder alters the way in which the particles can rotate about each other at contact.[36] Figure 2-17 is the result of modelling the normalised free energy landscape of two approaching ellipsoids (left column) and two approaching cylinders (right column). For a given centre to centre separation the tip-to-tip interaction is more energetically favourable for both systems up to contact as can be seen from Figure 2-17 (a) for ellipsoidal particles and (d) cylindrical particles both having an aspect ratio of six. At contact, the capillary force is almost two orders of magnitude larger for the cylinders than the maximum for the ellipsoids. For two particles at contact in the tip-to-tip configuration, tiles (c) and (e) show the normalised free energy as a function of bond angle. As can be seen there is a weak local minimum for cylinders in the side to side configuration, $\phi = 180°$, but there is a significant energy barrier between them (ΔE_b) as illustrated in tile (e). The same is not true for the ellipsoidal particles (c), which monotonically decrease with bond angle as the particles can simply 'roll' around each other due to the lack of sharp corners imposing an energy barrier.[36,67,97] A consequence of this property is that chains of ellipsoids behave as elastic elements in response to bond bending whereas chains of cylinders behave as 'brittle' elements remaining ridged for sufficiently small torques[36], allowing them to be laterally compressed into the close packed structures seen in Figure 2-16 (b).

The existence of multiple stable states for cylindrical particles offers an even richer landscape for the formation of microstructures. The global equilibrium state is the cylinder lying flat with the interface[20] and a meta-stable upright state[21], but it has also been reported that for aspect ratios between 2 and 0.5 the global equilibrium state is a

tilted orientation.[25] The leading order deformation for these tilted states is no longer quadrupolar but hexapolar which we discuss in the next section. Below aspect ratios of $m = 0.5$ the cylinders start to resemble discs and stand upright at equilibrium. The different leading order modes can lead to different microstructure such as orthorhombic, hexagonal closed packed, honeycomb and even more exotic crystal structure like the kagome lattice. In the next section we discuss some more exotic anisotropic particles and their self-assembly characteristics.

2.3.3 Cubes and Other Anisotropic Shapes

We now consider an isolated cubic particle adsorbed at an immiscible interface. Compared to the cylinders and ellipsoids, a cubic particle has an extra degree of freedom because the height, tilt and rotation angles, as defined in Figure 2-18 (a), can all vary to minimise the surface free energy. Simulations of isolated cubic particles[63] reveal three stable configurations as illustrated in Figure 2-18 (c), in which the cube can equilibrate face up in the {100} orientation (*left)*, edge up in the {110} orientation (*centre*) or vertex up in the {111} orientation (*right*).[63] Interestingly, including the effects of interfacial

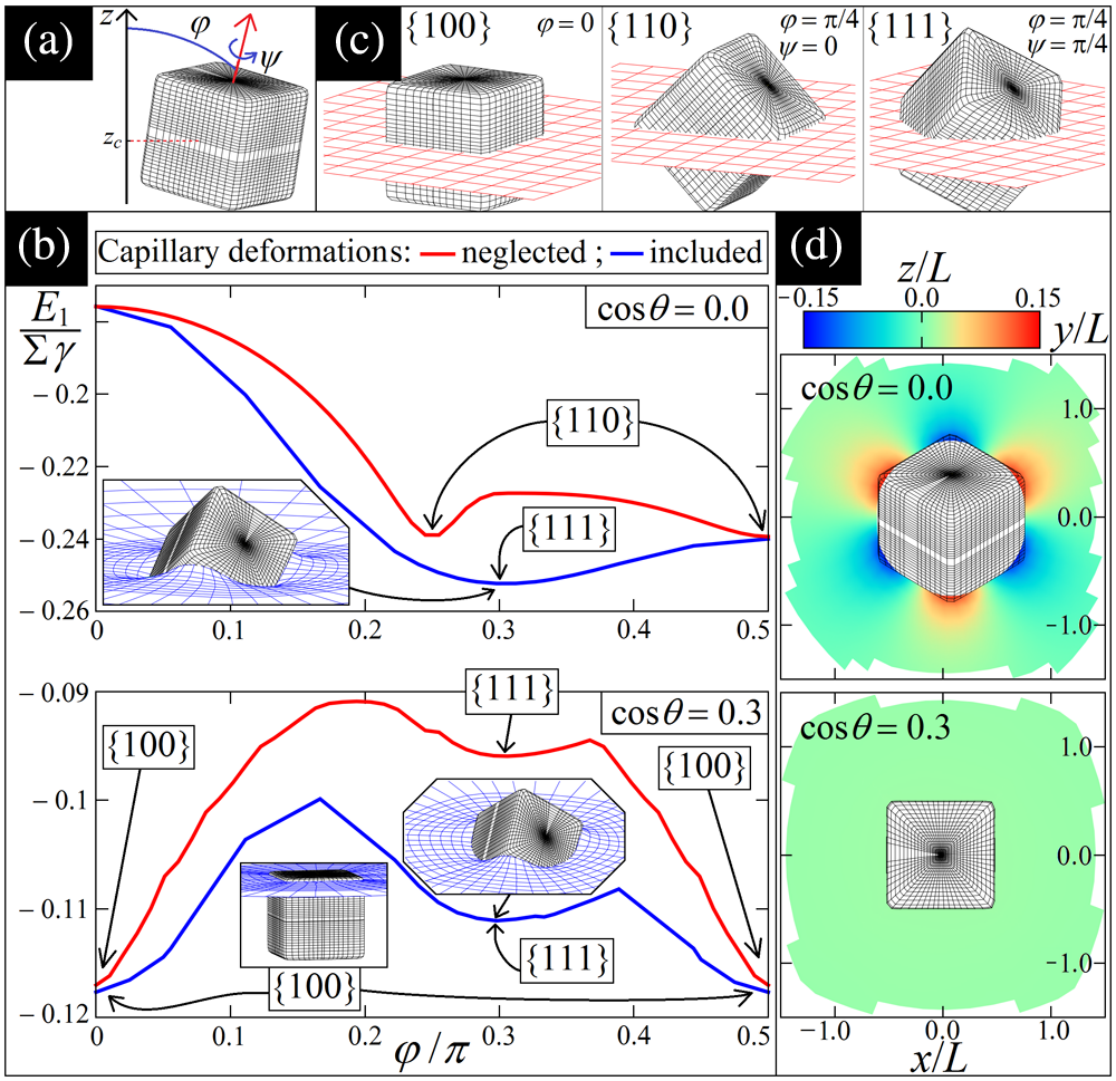

Figure 2-18 (a) Soligno *et al.* definition of tilt (φ) and rotation angles (ψ) for a cubic particle. (b) Adsorption energy of an isolated cube at a fluid-fluid interface, minimised over the particles centre of mass and rotation angle for a deformable (blue) and flat interface (red line) for a neutrally wetting system (upper) and hydrophobic system (lower) (reproduced from[63]). (c) illustrations of the three stable configurations. (d) contour plots of the two global equilibrium states in (b).

deformation significantly changes the free energy landscape by shifting the global free energy minima from the {110} to the {111} configuration for neutrally wetting cubes (Figure 2-18 (b) *top*). In the case of hydrophobic cubes (Figure 2-18 (b) *bottom*) the inclusion of interfacial deformation simultaneously reduces the free energy of the adsorbed cube in the {111} configuration and also increases the energy barriers to the other two stable states. The leading order mode for neutrally wetting cubic particles in the {111} orientation is hexapolar as illustrated in the contour plot of Figure 2-18 (d) (*top)*.

Experiments by Song *et al.* using polystyrene microcubes at an air-water interface were shown to self-assemble to linear chains and close-packed hexagonal aggregates[98,99] as illustrated in Figure 2-19.[99] More intriguingly, experiments have also revealed that cubic particles can self-assemble into graphene like honeycomb and hexagonal crystal structures.[37,38,100] Anzivino *et al.* and others have explained these results from a theoretical perspective by showing that the equilibrium orientation of cubic particles varies with contact angle which changes the interfacial deformation.[39,63,68] In turn, this effect also changes the capillary interactions leading to the different types of self-assembly observed by Song *et al.* Furthermore, simulations of

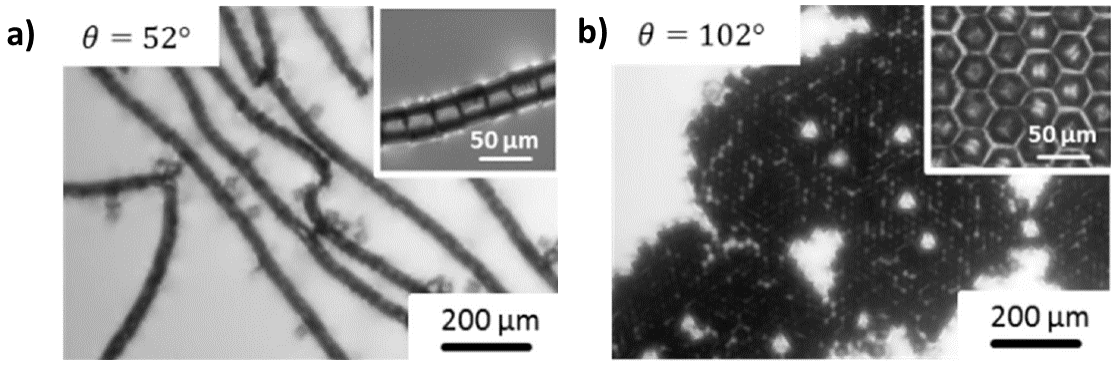

Figure 2-19 Top-down microscopy images of microcubes self assembled at an air-water interface (reproduced from[99]). (a) Linear chains self assembled from hydrophilic cubes and (b) hexagonal closed packed structures self-assembled from hydrophobic cubes. We note that the authors use θ to denote the contact angle of the cubes.

cubic particles have shown that more exotic honeycomb structures can self-assemble as a result of the interaction of the hexapolar deformations. As a result, the hexagonal closed lattice becomes the global free energy state, alongside meta-stable open structures.[39,63,68] This opens up the exciting possibility of engineering two dimensional materials by selection of particle shape coupled with immobilisation techniques.[78,101]

2.3.4 Capillarity and Bio Locomotion

To conclude this section, we briefly discuss insects using capillarity for bio locomotion. Water walking insects exploit surface tension through a variety of means allowing them to remain suspended on the interface. However, to pass from water to land they must climb the meniscus. For a millimeter scaled insect this has been referred

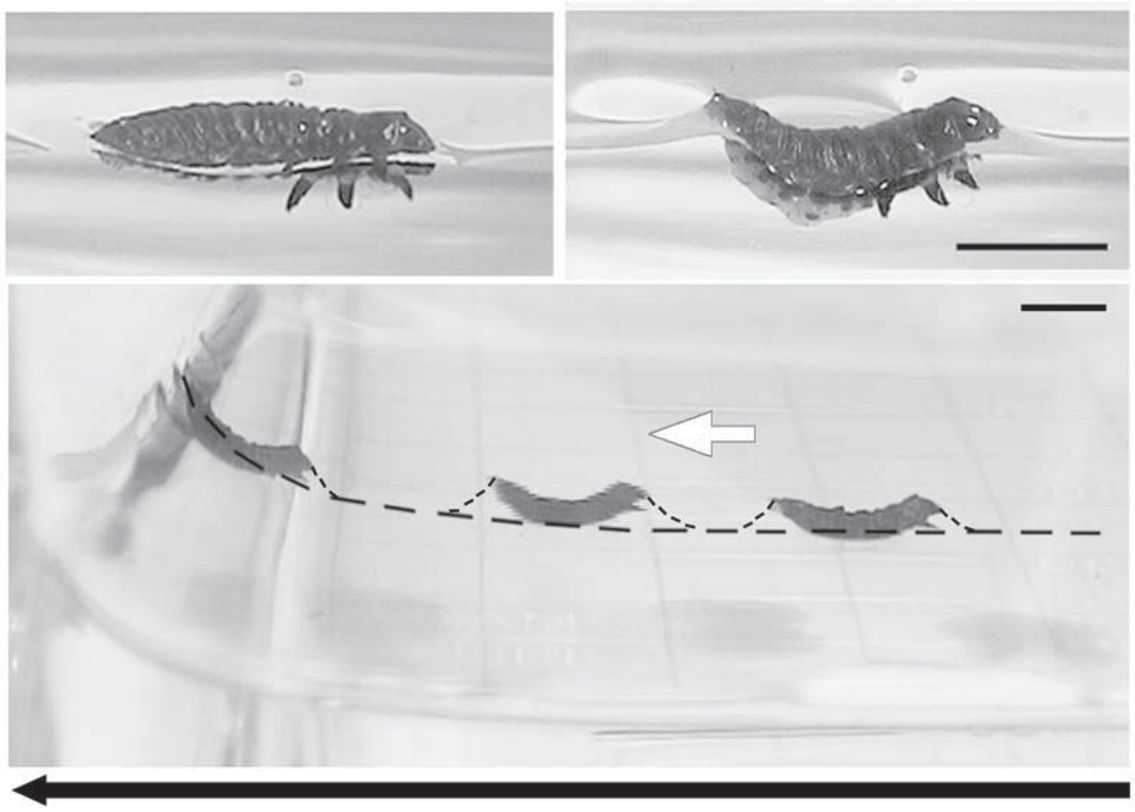

Figure 2-20 Time lapse of a waterlily leaf beetle climbing a meniscus (reproduced from [102]). (Top left) The insect is partially wetting and is therefore circumscribed by a contact line. (Top right) The beetle deforms the interface by arching it's back to create a quadrupolar deformation. (Bottom) The attractive force between the meniscus deformations pulls the beetle up to the intersection at speeds of up to $10\ ms^{-1}$ .The scale bar is $3mm$.

to as “climbing frictionless mountains”.[102] In an ingenious response, evolution has allowed such insects to utilise capillary interactions to propel themselves up the meniscus using the exact same physics that is responsible for the colloidal attractions discussed so far. As illustrated in Figure 2-20, the beetle larva (top left) arches its back to create a quadrupole (top right) which in turn generates a lateral force and drives it to the top of the meniscus.[102] For a random orientation the beetle larva experiences a torque which serves to align it perpendicular to the meniscus, very similar to the torque and attraction between cylindrical colloids.[20] By deforming the interface, the insect converts its muscular strain to surface energy which powers its accent.

2.3.5 Plates

In an early series of experiments, Bowden *et al.*[35,65,103] demonstrated the potential for precision self-assembly by showing that it was possible to engineer specific capillary bonds, achieved by controlling the shape of the menisci of adsorbed particles. The purpose of this self-titled mesoscale self-assembly (MESA) was to borrow ideas from molecular self-assembly. Specifically, shape-selective interactions between hydrophobic surfaces, and use such ideas to self-assemble larger structures to gain insight into molecular self-assembly. In previous work in MESA, spherical colloids were shown to self-assemble into close packed arrays due to interactions involving capillary[104–108] chemical[109,110], electrodynamic[111] or even entropic[112] forces. While interesting, progress in this field requires the development of *flexible* strategies which can lead to a greater range of structures. Bowden *et al.* presented a simple set of design rules which they then demonstrated could led to a rich array of both 2D and 3D structures which we discuss below.

The experiments involved dispersing millimetre scale hexagonal platelets with functionalised edges at an oil/water or water/air interface and agitating the system with an orbital shaker.[35] The way in which the undulations are introduced to the menisci is by making selected surfaces hydrophilic. The particles were fabricated from PDMS which is naturally hydrophobic, coating select surfaces with tip-ex and exposing the particle to oxygen plasma made the exposed surfaces hydrophilic. In a final step the tip-ex is removed to reveal the original hydrophobic surfaces.

Figure 2-21 illustrates some of the configurations studied, with black edges indicating the hydrophobic faces. Figure 2-21 (a) is a top-down view of the attraction between two aligned plates having a single hydrophobic face resulting in a positive meniscus (rise), (b) a side view of two positively curved menisci attracting (left), two negatively curved attracting (center) and the repulsion between a negatively and a positively curved meniscus. (c) Shows some of the specific patterning motifs studied

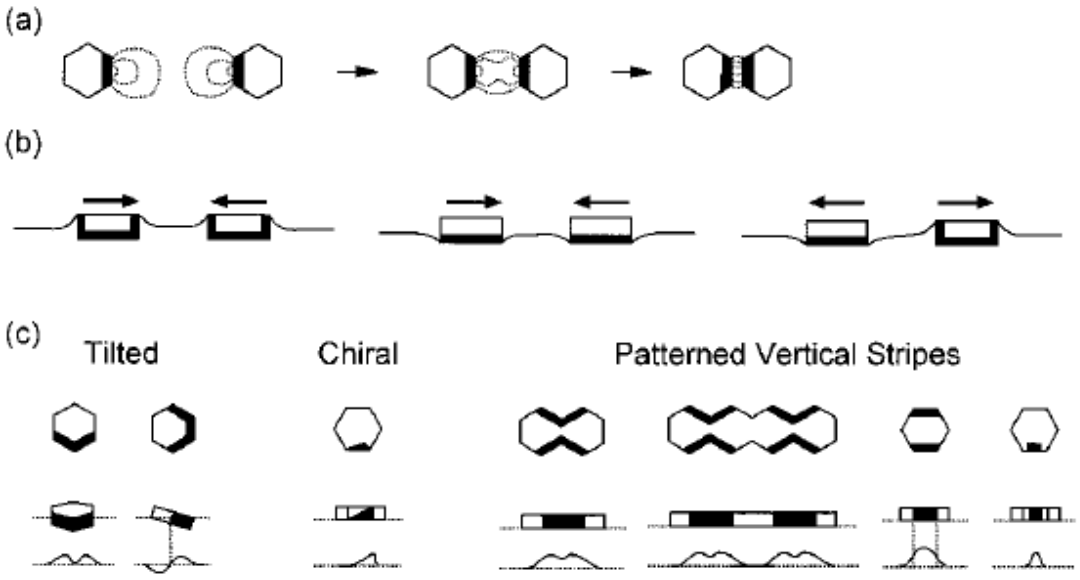

Figure 2-21 Illustration of hexagonal platelets from the experiments of Bowden *et al.* (Reproduced from [35]) showing (a) the attraction between two particles with a meniscus rise (indicated by the dashed lines). (b) Side views of two positive menisci *(left*), two negative menisci (*centre*) and a negative repelling a positive (*right*). Viewpoints of different patterning motifs, the top row are birds eye view, middle row are the side viewpoints and bottom row the profile of the menisci.

from a top-down perspective (top row), a side view (row 2) and finally the profile of the meniscus these motifs result in.

In total, 14 motifs where investigated and it was determined that not only the shape of the menisci but both the strength and the directionality of the capillary interactions could be controlled by the choice of surface patterning.[35] The nomenclature to discuss the different surface patterning is as follows. The hydrophobic faces are numbered by placing them in square brackets such that [1,2] is a plate with 2 adjacent sides (Figure 2-21 (c, top row, far left)) and [1,3,5] indicates every other face is hydrophobic. Figure 2-22 shows images of some of the self-assembled structures after the systems are left for 24 hours, the insets are sketches of the particle patterning. As can be seen this technique yields a wide array of lattice structures ranging from simple rectangular arrays in (a) and (d) from the [1] and [1,5] patterning, to honeycomb

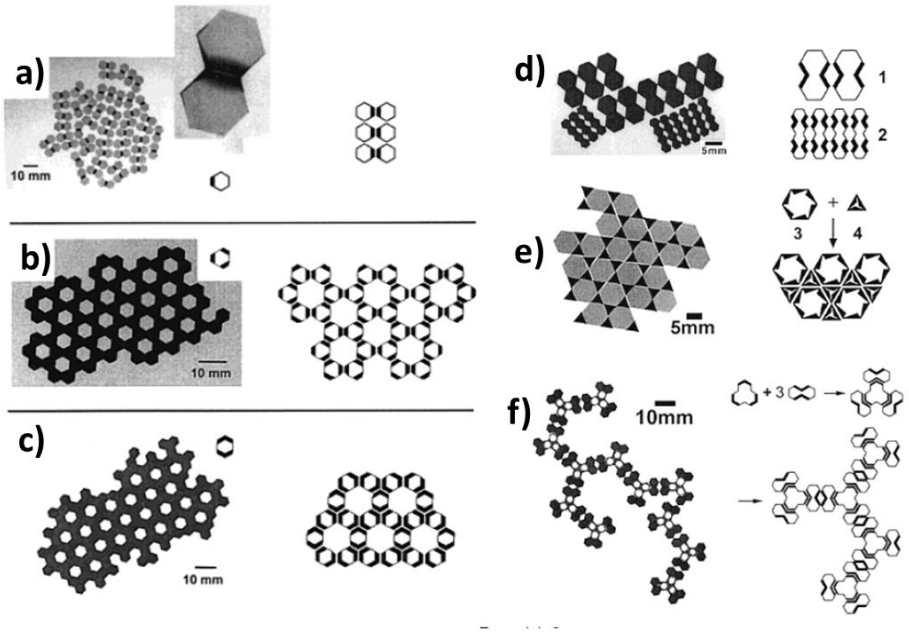

Figure 2-22 (a) Hexagons self-assembled into dimmers based on the attraction from the [1] hydrophobic faces. (b & c) Hexagons self-assemble to open hexagonal arrays based on the [1,3,5] and [1,2,3,4] motifs. (d) Square and extended chains (f) arrays from [1,5] and a combination of [1,5] and [1,2] motifs. (e) Close packed arrays arising from chiral surface patterning. The left side of each image is an optical micrograph and the right a schematic representation (reproduced from[35]).

structures resulting from the [1,2,3] and [1,2,4,5] patterning and even the chain like structures in (e) and (f).

The particles remained at the interface in the Bowden *et al.* experiments despite their large size because of the change in surface chemistry. A significant roadblock to utilizing self-assembly in practical systems or device fabrication is in miniaturizing such assemblies. Colloidal synthesis has developed to permit specific shapes to be fabricated such as spheres, ellipsoids, cylinders, cubes and even more esoteric shapes[10,12–14,16,113] out of a variety of materials. However, combining shape control with functionalization or patterning specific facets becomes difficult to scale down to the colloidal regime. To overcome this obstacle, we present a theoretical solution in Chapter 6 which bypasses the need to pattern specific facets in order to control the meniscus shape and achieves it through shape alone. In the next chapter we introduce the primary research tool we use to study these phenomena, Surface Evolver.

Chapter 3 Surface Evolver Method

In this chapter we discuss our simulation method, the finite element package Surface Evolver (SE)[114,115] which we use to model particles at interfaces. In its simplest form the Surface Evolver program minimises the energy of a surface, subject to user defined constraints. A surface is represented as a simplicial complex and the energies can include surface tension, gravity, or other forms. The user defined constraints can be geometric, such as shape or vertex location, body volumes and pressures or even shapes and areas. Finally, the surface energy is minimised through an iterative process which guides the specified surface down to its minimum energy configuration, the details of which we will discuss in this chapter.

3.1 Sphere at a Liquid Interface

We start with a simple case of a hydrophobic, spherical particle at an oil-water interface to explain the stages required in creating a Surface Evolver simulation. We arbitrarily chose the hydrophobic contact angle to be $\theta_w = 120°$. The user specifies an initial surface in terms of a finite number of geometric elements and Surface Evolver then represents this surface as a union of simplices. The initial surface specifies numbered vertices with their associated Cartesian co-ordinates, a numbered edge which joins a head and a tail vertex and a facet which is defined as a chain of three or more oriented edges. We illustrate this in Figure 3-1 showing the vertices as numbered circles which are joined by numbered, colored and directional edges. The magenta edges represent the oil-water interface, the cyan edges the particle-oil interface and the black edges an initial tessellation which SE does automatically. We omit the facet numbers in the figure for visual clarity and we omit the particle-water interface for computational efficiency without loss of generality.

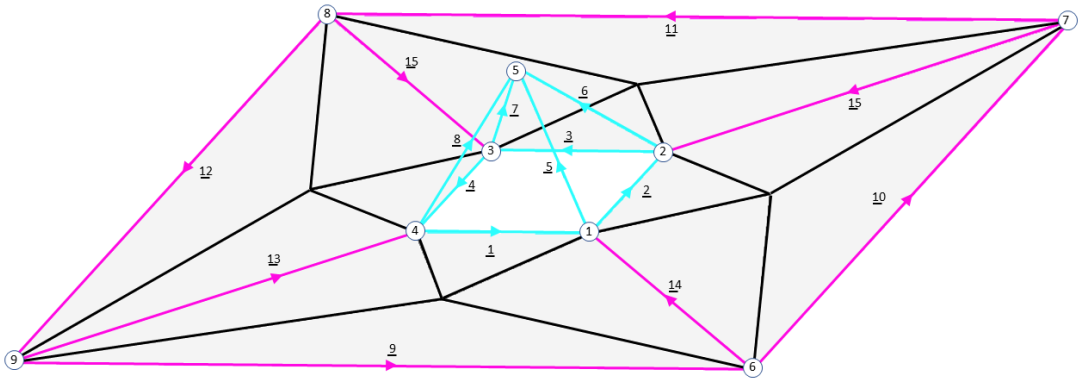

Figure 3-1 Example of the initial geometry of a spherical particle at a liquid interface. Vertices are illustrated as numbered circles, edges as underlined numbered lines with their directions indicated by arrows. As explained in the text, the cyan edges indicate the faces of the particle having a surface tension and shape constraints placed upon them and the magenta lines form the facets of the interface. The black lines are an initial tessellation SE performs. automatically.

We impose a variety of constraints on this surface to model the equilibrium height of the center of a spherical, hydrophobic colloid with respect to the planar interface. Firstly, we impose the sphere equation $x^2 + y^2 + z^2 = r^2$ on all the facets, edges and vertices on the particle (cyan) as a constraint forcing all simplices on the surface to obey this equation. Next, we impose a surface tension on these facets via Young's equation as follows. The total free energy of the system is given by

$$F_{int} = \gamma_{ow}A_{ow} + \gamma_{po}A_{po} + \gamma_{pw}A_{pw} \quad \textbf{(3-1)}$$

In which the subscripts refer to oil-water (ow), particle-oil (po), particle-water (pw) and area A. Using Young's equation $\gamma_{ow}\cos\theta_w = \gamma_{op} - \gamma_{wp}$ where θ_w is the contact angle and noting that $A_{op} = A_P - A_{wp}$ (where A_P denotes the total area of the particle) we can rearrange Equation 3-1 and drop irrelevant terms to

$$F_{int} = \gamma_{ow}A_{ow} + \gamma_{os}\cos\theta_w A_{os}. \quad \textbf{(3-2)}$$

In order to implement the contact angle within the simulations we typically set $\gamma_{ow} = 1$, and rearrange such that $\gamma_{po} = \cos\theta_w$. We apply this surface tension to the relevant

facets (cyan structures in Figure 3-1) enabling us to model neutrally wetting, hydrophobic or hydrophilic particles by simply changing a single parameter, θ_w.

For computational convenience and without loss of generality we center the particle at the origin and allow the interface to move freely in the z direction to fully equilibrate. This no different to allowing the particles center of mass to vary freely and if the simulation cell is large enough, enforces a planar interface far from the particle. The boundary is effectively a Neumann boundary condition because we assume the simulation walls are neutrally wetting, having a contact angle of $\theta_w = 90°$ at the outer boundary.[20] Once a geometry has been specified, we need to create a suitable tessellation and minimization protocol and it is worth making some remarks about how SE calculates the free energy minima to justify our choices.

The iteration step is the fundamental operation of the Evolver, it reduces energy where possible while obeying any constraints by employing a gradient decent method. For a given surface the total energy is treated as a function of the co-ordinates of the vertices. The negative gradient of the energy of a given vertex gives the force and therefore the summation of all these forces is the negative energy gradient. After this is calculated each vertex is simultaneously moved by a global multiple, called the scale factor, of its calculated force. For completeness, fixed vertices forces are set to zero, vertices on boundaries are mapped back to the forces on the boundary parameters and vertices on constraints have their forces projected to their tangent spaces.[114]

Given that the forces acting on the vertices will result in a velocity, the scale factor can be physically interpreted as the time step over which the velocity acts. In the default mode the Evolver will successively half or double this factor until a minimum energy has an upper and lower bound within the predefined target tolerance. At this

point a quadratic interpolation between the two is used to estimate the optimal value and this is used on the final iteration.[114] We now briefly discuss the options for tessellating the surface.

The main surface operations and when to use them vary for specific systems, ultimately relying on trial and error for a known result for comparison (shown later), but here we discuss the three most important options, refining, vertex averaging and equi-angulation. To refine a facet SE creates a new vertex at the midpoint of each of the edges and uses these to subdivide the original into four new facets. We can think of this physically as increasing the resolution. Equi-angulation uses the Delaunay triangulation method in order to make the facets as close as possible to equilateral, a beneficial tool to smooth out large effects/forces/outliers. Lastly, vertex averaging computes a new co-ordinate as the area-weighted average of the centroids of the facets adjoining the vertex.

Given the outline discussion of the internal workings of SE we can now settle on a minimization and tessellation protocol and show an example evolution of a hydrophobic, spherical colloid at a water-oil interface as illustrated in Figure 3-2. As can be can be seen from the snapshots, we switch between tessellation and minimization frequently in order to guide the system to its minimum energy configuration. We can be confident the surface is fully minimized when the scale factor stops changing (or does so minutely) and also from a visual inspection of the surface.

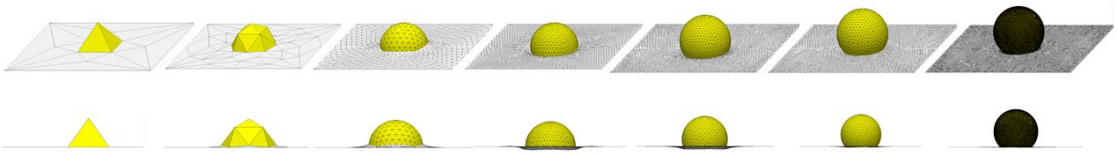

Figure 3-2 Snap shots of the evolution of a hydrophobic spherical particle at an oil water interface from an axonometric view (top row) and an in-plane view (bottom row). As discussed in the text the interface moves down the particle to satisfy Young's constant contact angle constraint.

3.2 Anisotropic Particles at the Interface

Spherical particles have been well studied from theoretical and experimental points of view.[1] Advances in particle synthesis techniques over the past decade have open up a rich variety of shapes such as ellipsoidal[10], cylindrical[113], cubic[13], tetrahedral[16] and even exotic Janus dumbbell particles.[69] To study these systems in detail from a theoretical point of view we require a mathematical definition of their geometry in order to simulate them. Unfortunately, this problem is not as clear cut as it may seem within finite element analysis software due to the presence of sharp edges in the tessellation. When the contact line attempts to pass over a sharp edge, for example on a cubic particle, it's contact angle can no longer be defined. In reality the contact angle is still constant but appears trapped at the edge with its value seemingly changing.[116]

To overcome this problem, we employ a superquadratic representation, Equation 3-3, which allows us to model the particle as a continuous surface.[117]

$$\left|\frac{x}{s_1 r_{part}}\right|^{\varepsilon_1} + \left|\frac{y}{s_2 r_{part}}\right|^{\varepsilon_2} + \left|\frac{z}{s_3 r_{part}}\right|^{\varepsilon_3} = 1 \qquad \textbf{(3-3)}$$

In equation 3-3, r_{part} defines the particle size in dimensionless units, s_i controls the ratios of the length, width and height of the particle and ε_i, the squareness parameter controls the specific shape of the particle. Figure 3-3 illustrates the power of this parameterization for different settings, demonstrating some of the morphologies available. Using the superquadratic representation overcomes the issue of the contact line 'pinning' at sharp edges because edges and corners are a continuous surface with definite curvature, allowing the contact line to smoothly pass them. We can even simulate highly sharp edges by shrinking the radii of curvature and setting $\varepsilon_i > 200$ which we have done for cylindrical particles with no problematic effect. Finally, we remark that modifications can be made to Equation 3-3 which, when combined with piecewise functions within Surface Evolver unlock the possibility to model essentially

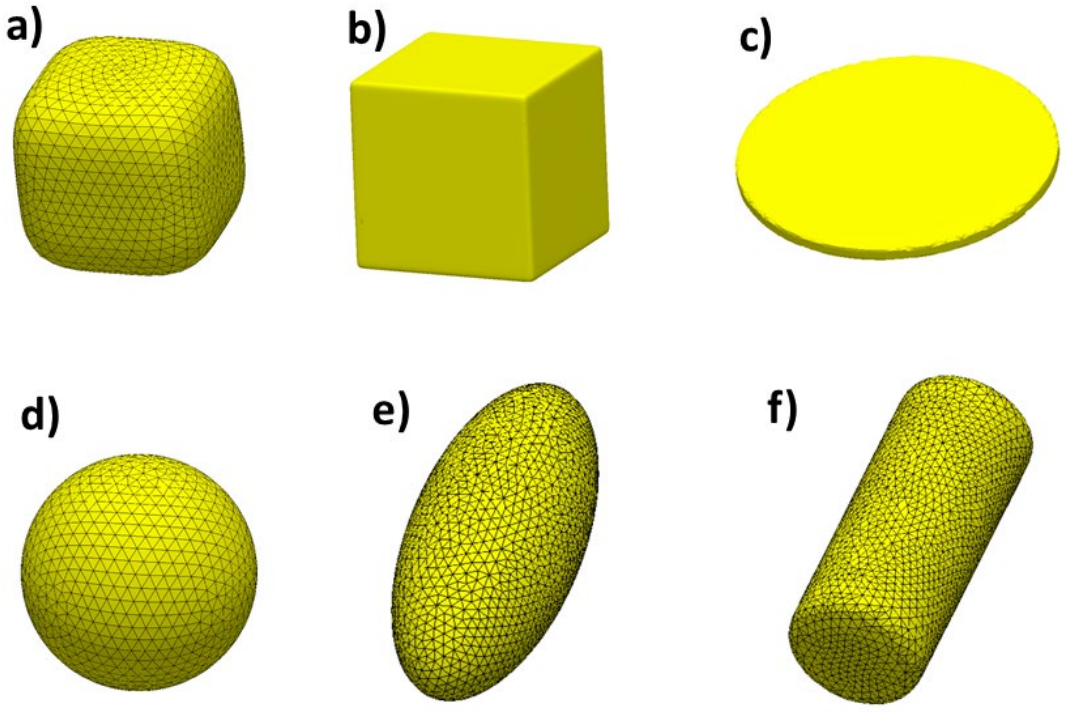

Figure 3-3 Examples of particle morphologies available from Equation 3-3 by varying ϵ_i and s_i. For all tiles $r_{part} = 1$ and the inclusion of the mesh is solely for visual effect. (a) $s_{1,2,3} = 1$, $\epsilon_{1,2,3} = 4$ (b) $s_{1,2,3} = 1$, $\epsilon_{1,2,3} = 20$ (c) $s_{1,2} = 1$, $s_3 = 0.1$, $\epsilon_{1,2} = 2$, $\varepsilon_3 = 20$ (d) $s_{1,2,3} = 1$, $\epsilon_{1,2,3} = 2$ (e) $s_1 = 2$, $s_{2,3} = 1$, $\epsilon_{1,2,3} = 2$ (f)) $s_1 = 2.5$, $s_{2,3} = 1$, $\epsilon_1 = 20$, $\varepsilon_{2,3} = 2$.

any polyhedral with arbitrary surface modifications we please, as will be demonstrated in Chapter 6.

3.3 Coordinate Transformations

An isolated and homogenous spherical particle has a single degree of freedom to equilibrate with its surroundings, only its height perpendicular to the planar interface can vary. However anisotropic particles have more degrees of freedom. In the simplest case of an ellipsoid, the particle can change its height and its tilt angle, the angle the semi-major axis makes with the planar interface (as shown in Figure 2-9 (a)). A more complex example is that of a cuboid which can change its tilt angle, rotation angle and height (Figure 3-4). The simplest way to accommodate this in our simulation is using coordinate transforms relating the local co-ordinate system aligned along the principal axis of the particle to the lab frame aligned to the undisturbed, planar liquid interface.

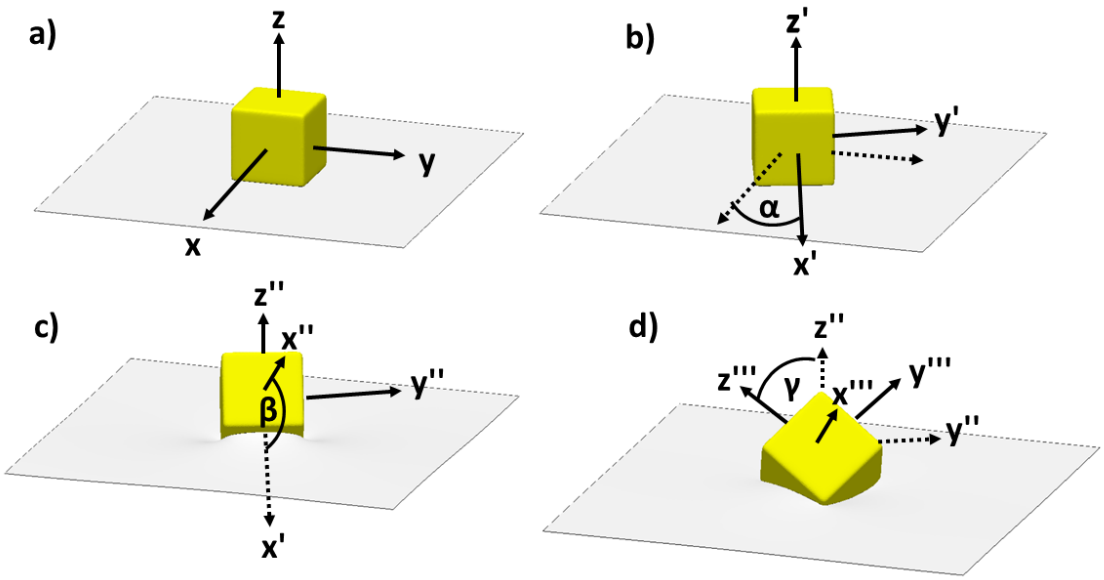

Figure 3-4 An example of how coordinate transforms are used to orientate a cubic particle at the interface, the solid arrows represent the unit vectors post transform and the dashed arrows are the unit vectors from the previous transform for reference (omitted for clarity in some instances). (a) The initial unit vectors. (b) the first transform about the unit vector z. (c) the second transform about the y prime axis. (d) The final transform about the x prime axis. We note that in the images the interface equilibrates with the hydrophobic particle and as such is free to move up and down and deform.

Combining Equation 3-3 with the rotational matrices shown in Equations 3-4 through Equation 3-7[117] we can describe a system which simulates many different particle morphology's at any orientational configuration we desire. The particle reference frame is arrived at by rotations α, β and γ about the axis z, y' and x'' respectively.

$$\begin{bmatrix}\cos\gamma & -\sin\gamma & 0\\ \sin\gamma & \cos\gamma & 0\\ 0 & 0 & 1\end{bmatrix}\times\left(\begin{bmatrix}\cos\beta & 0 & \sin\beta\\ 0 & 1 & 0\\ -\sin\beta & 0 & \cos\beta\end{bmatrix}\times\begin{bmatrix}1 & 0 & 0\\ 0 & \cos\alpha & -\sin\alpha\\ 0 & \sin\alpha & \cos\alpha\end{bmatrix}\times\begin{bmatrix}x\\ y\\ z\end{bmatrix}\right)=\begin{bmatrix}\boldsymbol{x}\\ \boldsymbol{y}\\ \boldsymbol{z}\end{bmatrix} \quad \textbf{(3-4)}$$

Resulting in

$$\boldsymbol{x} = x\cos\beta\sin\gamma + y\sin\alpha\sin\beta\cos\gamma + z\cos\alpha\sin\beta\cos\gamma - y\cos\alpha\sin\gamma + z\sin\alpha\sin\gamma \quad \textbf{(3-5)}$$

$$\boldsymbol{y} = x\cos\beta\sin\gamma + y\sin\alpha\sin\beta\sin\gamma + z\cos\alpha\sin\beta\sin\gamma + y\cos\alpha\cos\gamma - z\sin\alpha\cos\gamma \quad \textbf{(3-6)}$$

$$\boldsymbol{z} = -x\sin\beta + y\sin\alpha\cos\beta + z\cos\alpha\cos\beta \quad \textbf{(3-7)}$$

All references to particle orientation are made with respect to the interface who's normal is perpendicular to the planar, undisturbed interface. In this thesis we investigate a variety of systems and make definite references of α, β, γ in each chapter with respect to a specific system. All results presented are based on these simulation methods modified in degrees of complexity, for example when considering two particle interaction we add in an extra translational transform in the x-y plane.

3.4 Simulations with Periodic Boundary Conditions

The default domain of a surface is Euclidean space R^3. In order to implement periodic surfaces in the Evolver one can define the domain of a flat torus having an arbitrary parallelepiped as its unit cell (i.e., periodic boundary conditions).[115] The initial geometry we define for these simulations is *not* the familiar unit cell from crystallography but requires the specification of non-degenerate vertices and edges *only* and are given as Euclidean coordinates, not linear combinations of the basis vectors. The way in which the unit cell wraps around the torus is specified by how the degenerate edges and faces cross the unit cell. We illustrate this in Figure 3-5 which is an example of a cubic particle in a HCP unit cell in the {111} orientation. We show the initial

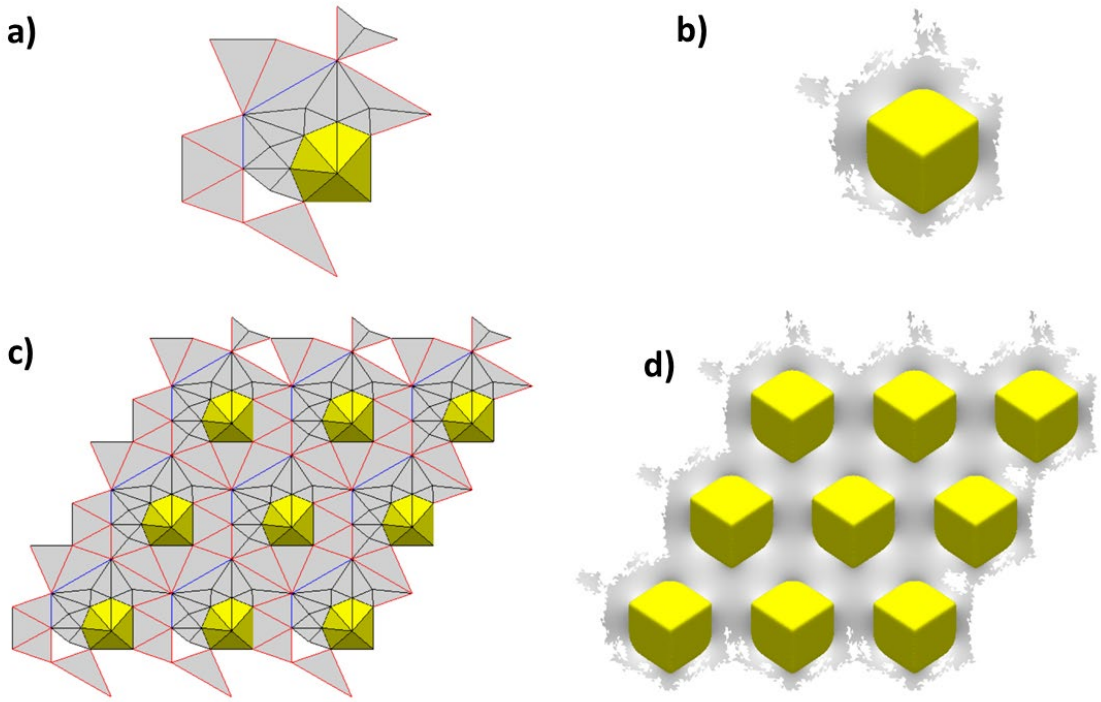

Figure 3-5 Illustration of the implementation of periodic boundary conditions in Surface Evolver for a cubic particle in the {111} orientation in a hexagonal closed packed (HCP) lattice. (a) The 'unit cell' as specified to the software, yellow facets model the particle and grey the interface. The blue lines are the only uniquely specified lines within the script because the red lines are degenerate. (b) The unit cell after minimisation procedure. We note the odd tessellation is simply the visual representation from SE and the unit cell is indeed part of a HCP lattice for which we show nine particles pre and post minimisation in (c) and (d) respectively.

geometry (left column) and the fully minimized outcome (right column) with the individual cell on the top row and a collection of nine cells (bottom row). The unit cell in (a) specified to the software consists of the yellow & grey facets representing the particle and interface respectively, with the blue lines being the only ones specified explicitly as the red are all degenerate.

3.5 Computational Practicalities

In this final subsection we provide some details of computational practicalities and parallelization necessary to facilitate the study. The systems we study in this thesis are generally defined as some function of center-to-center separation of two or more particles. These particles are sited in a simulation cell and we define the rest of the geometry as a function of particle separations in order that we may easily scale it by changing a single parameter at runtime. This procedure can lead to a computational difficulty because if we iterate the minimum energy calculations within the Evolver, decreasing the inter-particle separation with each iteration, every aspect of the simulation cell gets redefined simultaneously and the simulation can become unstable. This means we need to manually write and run one simulation for each distance. This behavior is not only tiresome but unfeasible for high resolution studies with thousands of individual simulations. In fact, during this research we have written and run well over a million simulations, and we detail the practicalities of this process in the following, providing examples in the appendices.

Given that the force calculation is in theory done simultaneously on each vertex one would immediately expect a significant benefit in computational time and resources by running SE on a graphics processing unit (GPU). Simple, parallel and repetitive calculations performed at speed is exactly the problem GPUs were designed to solve.

Unfortunately, Surface Evolver was conceived and written in 1992, a little over decade before the paradigm of parallel computing started to take-over from frequency scaling as a way to improved computational efficiency.[118] The software is written to run on serial architectures, in fact the engineering and technology company Bosch commissioned a study to investigate optimizing Surface Evolver via parallelization in 2012 in order to study thermal fatigue of PCB welds.[119] The researchers concluded that the software needed such significant reworking to make use of parallel hardware that it may as well be written from scratch. We have however found a work around to this problem which enables us orders of magnitudes decrease in computational time which we outline now for a model simulation of two approaching cylinders at the oil-water interface.

The most obvious way to simulate a pair of approaching cylinders is to run the simulation within a loop and decrease the center-to-center separation between them on each iteration, minimizing the free energy, outputting calculated values for the parameters to file and repeating. Indeed, the Evolver permits this approach with much the same syntax as for the C language. The length of time for the set of results being dependent on the total simulation box size, the scale of the tessellation and the increment size of the separation. Such an approach is absolutely feasible on a personal computer for low resolution, computationally simple and small systems. For clarity we borrow from the field of computer science and refer to the definition of computational complexity as the amount of resources to run an algorithm, which generally varies with the size of the input.[120] We further note that for geometrically complex simulations (for example some of the periodic systems we study in Chapter 6) we frequently require a

variety of initialization process to set the system up correctly and remain stable, these processes can take up to 24 hours.

An alternative way of to simulate a pair of approaching cylinders is to write a unique SE script for each center-to-center separation and call them sequentially from a batch script. The operating systems task manager allocates this process to one of the cores on the motherboard with its designated cache and the entire process stays on this local environment. However, with the omnipresence of multi cored machines we can simply divide the number of separations we wish to calculate across the number of cores we have access to and run them simultaneously because the operating systems task manager will allocate each batch script to each core. We initially discovered this by happy accident while trying to optimize the simulations to speed them up in a linear fashion with the initial testing performed on a low-end intel core i3 – 6006U (2.0Ghz, 3MB L3 cache) laptop. When calculating the free energy of two approaching cylindrical particles both with an aspect ratio of two the linear version took 9 hours 11 minutes to run and the parallel version completing in 3 hours 10 mins. Given the prevalence and relative cheapness of multicore pc's (at the time of writing AMDs 32 core/64 thread chip is the market leader), we actually use Hull university's supercomputer Viper, allowing us theoretically to run 6000 simulations simultaneously in the same time as a single iteration of the loop we outline initially.

The final problem is how to create the sheer quantity of simulation scripts and keep the read/write operations temporally coherent. To achieve this, we develop an initial 'master' simulation of a system we wish to study and give it the .txt file postfix. We then run a simple Python parsing program to get line by line access. Finally, we run this in a loop and change the quantities of interest by locating their line number and list position,

in the case of the cylinders the separation, and giving the output file name the (unique) index of the loop which we also used for the file name before adding the .fe postfix. This way we can also run the script in Unix on Viper by calling an array job on the numbered files. Such an approach results in a directory full of .txt files with the results of each individual simulation which we download and compile with a second Python program (included in the appendix).

To give an example of the possibilities the improved procedure unlocks, one of our very early studies was the free energy landscape of a neutrally wetting, chemically homogeneous and isolated cube. We varied the tilt and rotational angles (Figure 3-4) in five degree increments and calculated the free energy with SE for 324 unique configurations in order to benchmark our method against the results of Soligno *et al.*[63] The original version took us 3 months to reproduce their result, while we can now do it on a single overnight run using this massively parallel method.

Chapter 4 Adsorption Trajectories of Ellipsoidal Particles at Liquid Interfaces

4.1 Introduction

Colloidal adsorption at immiscible interfaces is of interest both scientifically and industrially yet a thorough understanding of the dynamics of the adsorption process is still lacking. In this chapter, we study the adsorption dynamics of ellipsoidal particles with a Langevin model. We couple this Langevin model to the Surface Evolver model in order to include the effects of interfacial deformation. Contact line pinning due to surface defects on the particle is incorporated into the model firstly through the use of dynamic contact angles applicable to adsorption timescales and secondly by renormalising particle friction coefficients. We compare our results to the experiments of Wang *et al.*[23] and Coertjens *et al.*[43] presented in chapter 2, and find we can quantitively model the latter but not the former. However, even in the comparison to Wang *et al.* our model accurately captures the spatial evolution of the adsorption process, if not the temporal. The purpose of this chapter then, is to clarify the interplay between capillary, viscous and contact line forces in determining the adsorption dynamics of micron scale colloids.

Particles adsorbed at liquid interfaces have a wide variety of applications such as emulsifications[5], encapsulation[121], food and pharmaceuticals[122], nanostructured materials[6] or even reconfigurable materials.[7] Beyond applications with direct commercial utility, these systems even allow for the creation of new exotic states of matter such as 'dry water'[123], liquid marbles[124] or even bijels.[125,126] The equilibrium behaviour of adsorbed colloids has been understood since the influential work of Pieranaski[46], the driving force of adsorption is the enormous reduction in free energy

while the final height of a spherical particle with respect to the interface is determined by its equilibrium contact angle, see Chapter 2 for a detailed discussion.

In opposition to the equilibrium case, the dynamics of the adsorption process of micron sized colloids to the liquid interface is much less well understood. The reduction in free energy is on the order of $10^5 kT$ by adsorption, and as such it was expected that the process was very fast due to this large driving force.[90] Experimentally however, Kaz *et al.*[89] found that after the initial breach of the interface a spherical colloid relaxes toward its equilibrium position on a timescale orders of magnitude slower than what is predicted by theoretical models based on viscous dissipation.[75–77] They showed that this logarithmically slow time scale for wetting dynamics could be explained when one considers transient pinning of the contact line at nanoscale defects as the interface traverses the surface of the particle.[79,127] Further investigations have shown that transient pining of the contact line also plays a crucial role in other dynamic phenomena involving adsorbed colloids, for example the anomalously slow in plane Brownian diffusion.[92]

Wang *et al.*[23] and Coertjens *et al.*[43] have more recently built on the foundations laid by *Kaz et al.*[89] and expanded the study of colloid adsorption dynamics to include ellipsoidal particles, once again reporting very slow adsorption timescales. The study of ellipsoidal particles is complicated by the fact that there is an additional degree of freedom, the tilt angle, when compared to spherical particles for whom only the particle height relative to the interface is of interest due uniaxial symmetry. The final equilibrium state for the ellipsoidal particles is orientated horizontally with its semi-major axis parallel to the interface.[67] Both experimental studies report a monotonic relaxation toward equilibrium with respect to time. This is in disagreement with viscous-based models in which the particle orientation with time varies non-monotonically.[21,22] The

discrepancy between theory and experiment has led to the proposition that both the adsorption time scale, and the adsorption trajectory for anisotropic particles, is controlled by contact line pinning.[44]

The viscous model used by de Graaf *et al.*[21] to predict adsorption trajectories and timescales has a number of important omissions. Firstly, the model neglects to account for deformation of the liquid interface, for particles in the low capillary number regime these deformations are no doubt significant.[18–20] Secondly, the model uses a physically unrealistic value for the ratio of the translational and rotational friction coefficients. In order to develop a model capable of accurately assessing the roles played by capillary, viscous, contact line pinning forces etc., in the adsorption of anisotropic particles, these effects must be incorporated.

In theory, the lattice-Boltzmann particle based simulations in refs.[22,128] can meet some of the requirements, however it is simply not possible to implement the long timescales necessary to investigate the low capillary and Reynolds number regimes which are experimentally relevant. However, Wang *et al.* produced a theoretical model based on contact line hopping[89,127] which was able to accurately capture their experimental results for adsorbing ellipsoids. The authors have assumed that the interface remains flat during adsorption in order to make their calculations tractable. While this model faithfully reproduces the experimental result it is not physically realistic as discussed earlier.[18–20,65,67] Implementing interfacial deformation in the contact line hopping model is a formidable challenge due to its complexity.

The purpose of this chapter is to address these challenges and incorporate interfacial deformation, contact line pinning and the correct ratio for particle friction coefficients into a Langevin model. Explicitly, we use Surface Evolver coupled with a Langevin model to account for interfacial deformation, renormalise particle friction

coefficients to account for contact line pinning, and finally we use the dynamic contact angle relevant to the adsorption timescales. This simple model reproduces a large amount of the experimental phenomenology, for example the monotonic evolution of particle orientation with time. More specifically, we need not explicitly invoke depinning dynamics of the contact line because we can obtain this behaviour by accurately modelling interfacial deformation and particle friction coefficients. Our approach enables us to quantitatively model the adsorption dynamics of Coertjens *et al.*[24] but not those reported by Wang *et al.*[23] Yet even in the latter case we are able to accurately capture the adsorption trajectory of the system (i.e., the evolution of particle orientation vs particle height).

In summary our theoretical model clarifies the different roles contact line, viscous and capillary forces play in determining the wetting dynamics of micron-scale anisotropic particles. As the final equilibrium state of anisotropic particles is not controlled by the dynamics of the individual adsorption coordinate but by their adsorption trajectory, our model can be used as a predictive tool for designing self-assembly processes for complex particles at immiscible interfaces.

4.2 Theoretical Model

We consider a prolate ellipsoidal particle adsorbing at a liquid interface, with long and short axis a, b respectively and aspect ratio $m = {}^{a}/_{b}$ (see Figure 4-1). Following experiments, we refer to the top and bottom liquid phases as oil and water respectively. The configuration of the ellipsoid at any instant during adsorption is described by the generalised coordinates h and ϕ, where h is the distance of the particle centre from the undeformed liquid interface and ϕ is the angle between the particle long axis and the flat interface normal. The particle height when it first contacts the liquid interface is

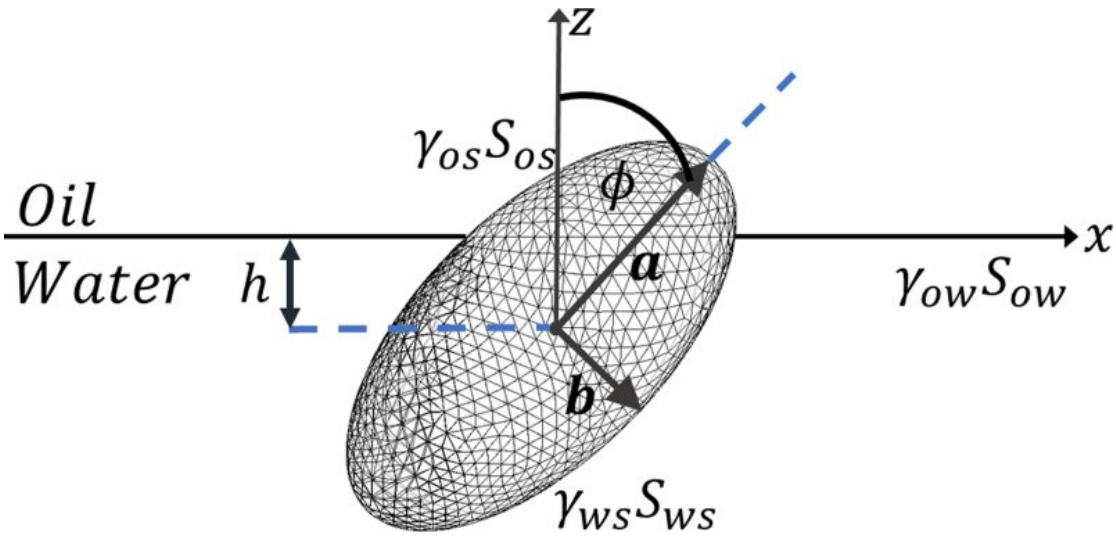

Figure 4-1 Variables characterizing the configuration of an ellipsoid adsorbing at a liquid interface.

given by $h_c = b\sqrt{m^2 cos^2\phi + sin^2\phi}$ [62] so that $h = h_c$,- h_c corresponds to the particle touching the interface from the oil and water side respectively.

For micron-sized particles where gravity is negligible, the free energy of the system is given by [21,25,48]

$$F = \gamma_{ow}S_{ow} + \gamma_{os}S_{os} + \gamma_{ws}S_{ws} \quad \textbf{(4-1)}$$

where $\gamma_{ow}, \gamma_{os}, \gamma_{ws}$ are the interfacial tensions and S_{ow}, S_{os}, S_{ws} are the areas of the oil/water, particle/oil and particle/water interfaces respectively. Using Young's equation $\gamma_{ow}\cos\theta_w = \gamma_{os} - \gamma_{ws}$ where θ_w is the contact angle of the oil/water interface at the particle surface, noting that $S_{os} = S_p - S_{ws}$ (where S_p is the total area of the particle) and dropping irrelevant constant terms, we can simplify Equation 4-1 to

$$F = \gamma_{ow}S_{ow} + \gamma_{ow}\cos\theta_w S_{os} \quad \textbf{(4-2)}$$

Note that we neglect line tension in the above free energies as we have checked that it has a negligible effect on adsorption dynamics for experimentally measured values of the line tension for micron-sized ellipsoids.[129] This observation is also consistent with what other authors have found for micron-sized objects.[128]

The interfacial areas and hence particle free energy depends sensitively on the boundary condition at the three-phase contact line. We consider two limiting cases,

firstly where the liquid interface remains flat, secondly where it is deformed due to the constant contact angle requirement.[25,48] The free energy in both cases is calculated using the finite element package Surface.[25,48,114] Specifically, the value of $F(h,\phi)$ is calculated on a 101×37 non-equidistant grid $h \in [-h_c, h_c]$ and $\phi \in \left[0, \frac{\pi}{2}\right]$. The data on this grid are then interpolated with a third order interpolation scheme to yield the full free energy landscape.

The adsorption trajectory is found by solving the Langevin equation for the particle at the liquid interface. In the low Reynolds number regime where inertial forces are negligible, this is given by the coupled differential equations

$$\lambda \frac{dh}{dt} = -\frac{\partial}{\partial h} F(h,\phi) \quad \textbf{(4-3)}$$

$$\mu \frac{d\phi}{dt} = -\frac{\partial}{\partial \phi} F(h,\phi) \quad \textbf{(4-4)}$$

where λ, μ are the translational and rotational friction coefficient of the ellipsoid respectively. The left and right-hand side of the above equations are the frictional and capillary forces respectively associated with translational (Equation 4-3) and rotational (Equation 4-4) motion. Note that since we are considering particles at liquid interfaces, λ and μ will include contributions from both viscous forces due to the bulk phases as well as contact line forces from the interface.[92] Note also that we have neglected random forces in the above equations since they are subdominant compared to capillary forces at a liquid interface. Finally, in general the coupling between rotational and translational friction is described by a tensor, however, as will be seen later, we can implicitly include this effect which leads to essentially the same adsorption trajectories when we renormalise the particle friction coefficients, along with the presence of interfacial drag.

In the general case, the friction coefficients λ and μ are functions of h and ϕ due to the asymmetry in the viscosity of the bulk phases and the anisotropy of the particle. However, as we shall see later, the frictional forces in the experimental systems are dominated by contact line forces rather than viscous forces. To a first approximation, we can therefore assume that both λ and μ are independent of h, i.e., the degree to which the particle is immersed in each of the two phases. We also note that the translational friction coefficient along the long and short axis of the ellipsoid differ by at most a factor of 2 in a viscous-based model.[21,130] To a first approximation, we will therefore also assume that λ and μ are independent of ϕ. Note that we have included the ϕ dependence of λ explicitly in our Langevin model[130] and found that this leads to adsorption trajectories which are essentially the same as what we obtain for constant λ.

Assuming λ, μ are independent of h and ϕ therefore, we can rescale Equations (4-3), (4-4) to

$$\frac{dh^*}{dt^*} = -\frac{\partial}{\partial h^*}F^*(h^*, \phi^*) \quad \textbf{(4-5)}$$

$$\frac{d\phi^*}{dt^*} = -\frac{\partial}{\partial \phi^*}F^*(h^*, \phi^*) \quad \textbf{(4-6)}$$

or more compactly to

$$\frac{d\vec{\eta}(t^*)}{dt^*} = -\vec{\nabla}F^*(h^*, \phi^*) \quad \textbf{(4-7)}$$

In the above equations, $h^* = {h}/{\alpha}$, $t^* = {t}/{\beta}$, $\phi^* = {\phi}/{\pi}$, $F^* = {F}/{\gamma_{ow}b^2}$ are scaled variables, α, β are scale factors that will be discussed in a moment, $\vec{\eta}(t^*) = \left(h^*(t^*), \phi^*(t^*)\right)$ is the dynamical state vector of the particle at any given moment in time and $\vec{\nabla} = \left(\frac{\partial}{\partial h^*}, \frac{\partial}{\partial \phi^*}\right)$ is the grad operator in (h^*, ϕ^*)coordinate space. Equation 4-7 tells us that the adsorption trajectories for the particle are remarkably simple in our simplified Langevin dynamics, i.e., they follow the path of steepest descent in the free energy landscape $F^*(h^*, \phi^*)$.[21]

The dynamic scale factors α and β depend on the friction coefficient ratio μ/λ. In ref.[21], de Graaf *et al.* chose $\alpha = \sqrt{a^2 + 2b^2}$, $\beta = \frac{a^2+2b^2}{\gamma_{ow} b^2}\lambda$ which corresponds to $\frac{\mu}{\lambda} = \frac{a^2+2b^2}{\pi^2}$ and we call this choice of scale factors Scaling 1. However, the authors point out that this choice is unphysical for a viscous-based model because it does not yield the sphere value $\frac{\mu}{\lambda} = \frac{4b^2}{3}$ for $m = 1$.[21] To overcome this problem, we also consider the scale factors $\alpha = \frac{2\pi}{3}\sqrt{a^2 + 2b^2}$ and $\beta = \frac{4\pi(a^2+2b^2)}{9\gamma_{ow} b^2}\lambda$ which corresponds to $\frac{\mu}{\lambda} = \frac{4(a^2+b^2)}{9}$ and we call this choice of scale factors Scaling 2.

4.3 Results and Discussion

To study the impact of different contact line boundary conditions and dynamic scaling on adsorption kinetics, in Figure 4-2(a-c) we show the adsorption trajectories calculated from our Langevin model for the simple case of neutrally wetting ellipsoids ($\theta_w = 90°$) with $m = 2$ for a flat liquid interface and Scaling 1 (Figure 4-2a), a flat interface and Scaling 2 (Figure 4-2b) and a deformed interface and Scaling 2 (Figure 4-2c). An equivalent experimental set up, with which we make a direct comparison with shortly, is a polystyrene ellipsoid having $a = 1200nm$, $b = 600nm$ adsorbing to a hexane-water interface under standard temperature and pressure. Regardless of the initial angle of the particle, we see that all adsorption trajectories that start from particle contact with the liquid interface (left/right red curve corresponds to contact from the water/oil side) end at the equilibrium state ($h = 0, \phi = {}^{\pi}/_{2}$) where the ellipsoid lies flat

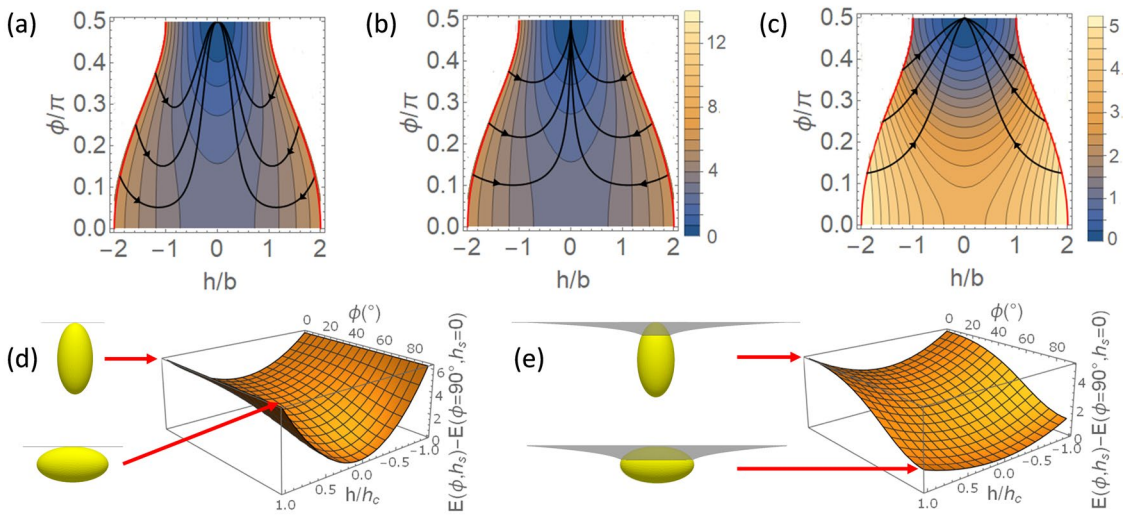

Figure 4-2 (a)-(c) Adsorption trajectories in the (h, ϕ) plane (black lines) for ellipsoids with contact angle $\theta_w = 90°$, aspect ratio $m = 2$ for (a) flat interface and Scaling 1, (b) flat interface and Scaling 2, (c) deformed interface and Scaling 2. The trajectories are superposed on contour plots of free energy landscapes, and the red curves bounding the landscape correspond to particles touching the interface from the oil side ($h = +h_c(\phi)$) or water side ($h = -h_c(\phi)$). For illustrative purposes, we show trajectories starting from either the oil or water side with initial particle angles $\phi_0 = 22.5°, 45°, 67.5°$. (d)-(e) Free energy landscape represented as a three-dimensional plot of free energy vs. h/h_c and ϕ and system configuration at $h = -h_c$ for ellipsoids in the vertical or horizontal orientation for (d) flat interface case and (e) deformed interface case.

along the interface. However, assuming a flat liquid interface leads to trajectories that are non-monotonic in ϕ (Figures 4-2a and 4-2b) while assuming a deformed liquid interface leads to trajectories are monotonic in ϕ (Figure 4-2c).

The qualitative change in the variation of ϕ is due to the fact that different contact line boundary conditions lead to very different free energy landscapes as shown in Figure 4-2d (flat interface) and Figure 4-2e (deformed interface). Recall that we are in the low capillary number regime where the adsorption is essentially a quasi-static process, i.e., particle adsorption is slow enough for the liquid interface to be in equilibrium with the configuration of the ellipsoid at each stage of the adsorption process. This means that when the liquid interface can deform, immediately after the particle breaches the liquid interface at $h = \pm h_c(\phi)$, the ellipsoid is attached to the liquid interface (effectively instantaneously on particle adsorption timescales) in order to satisfy the constant contact angle condition (Figure 4-2e left). The interface deformation Illustrated in Figure 4-2e is a transient state, its specific shape being dependent on the angle of attack and contact angle of the three-phase system. At the instant of attachment, we allow the interface to deform in such a way as to satisfy the constant contact angle condition treating it as a quasi-static system. In this case, the free energy of the system at $h = \pm h_c(\phi)$ strongly depends on ϕ, for example the horizontal state of the ellipsoid ($\phi = {}^{\pi}/_{2}$) has lower free energy compared to the vertical state ($\phi = 0$) since the former excludes more liquid interface compared to the latter. In contrast, when the liquid interface is flat, the ellipsoid is essentially detached from the liquid interface for $h = \pm h_c(\phi)$ (Figure 4-2d left) and the free energy of the system at $h = \pm h_c(\phi)$ is independent of ϕ. The flat interface assumption thus effectively raises up the corners of the landscape at $\phi = {}^{\pi}/_{2}$, causing the steepest descent paths to initially decrease in ϕ. The non-monotonic trajectories in Figure 4-2(a, b) are therefore

an artefact of the flat interface assumption, and such trajectories are either strongly suppressed or disappear altogether when we relax this assumption.

We next compare our theoretical model with the experiments of Coertjens *et al.* for fluorescent polystyrene ellipsoids where $a = 1200nm$, $b = 300nm$, $m = 4$ adsorbing to a hexane/water interface under standard temperature and pressure.[43] In the experiments a slight density mismatch between the particle ($\rho = 1.04$ g/cm^3) and subphase ($\rho = 1.15$ g/cm^3) for a 59 wt.% glycerol-water solution to provide a very small buoyancy force to guide the particles to the interface over time. The appropriate contact θ_w we should use for this system is a delicate question since the contact angle evolves slowly with time due to physical aging of the contact line.[129] To account for this effect, we use as our effective contact angle the *dynamic* (rather than equilibrium) contact angle that is relevant to the timescale of the adsorption process. Specifically, since adsorption occurs on the $\sim 0.3\ s$ timescale in this case, and the dependence of θ_w on particle stretching is weak[129], we use the contact angle measured for equivalent fluorescent polystyrene spheres on a similar timescale which is $\theta_w \approx 90°$.[129] Note that strictly speaking, one should also account for differences in advancing and receding angles around the contact line during particle adsorption.[44] However, as we are seeking a minimal model to capture the essential features of the experimental system, we have neglected this difference to a first approximation.

Due to limitations of their high speed confocal microscopy method, Coertjens *et al.* were only able to measure ϕ as a function of time.[43] In Figure 4-3, we compare all three models discussed above with a linear-log plot of the ϕ vs. t data of Coertjens *et al*. for an initial particle angle of $\phi_0 = 30°$. We use β as our fitting parameter to the drop in the data away from $\phi = 90°$. We see that quantitative agreement with the experimental data is obtained using the deformed interface and Scaling 2 model (black

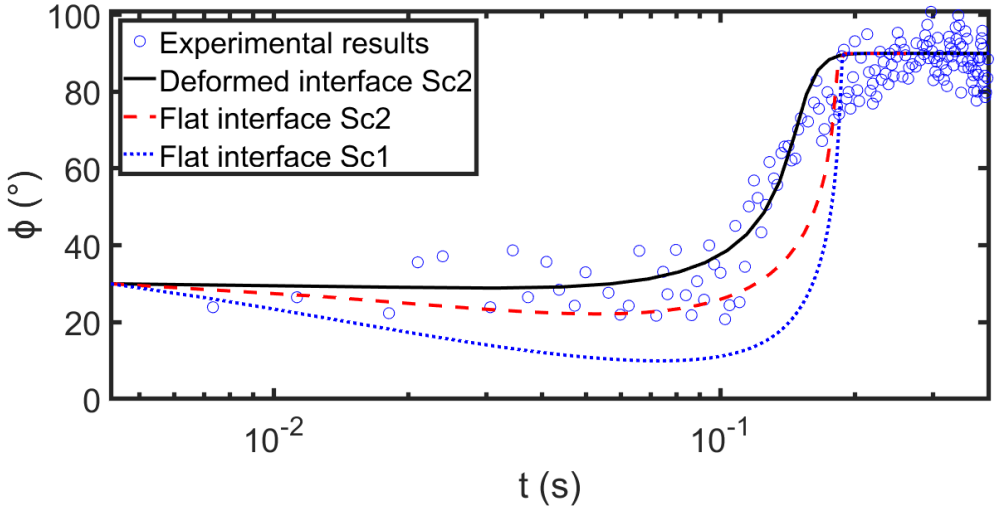

Figure 4-3 Linear-log plot of ϕ vs. t comparing the three theoretical models discussed in the main text for ellipsoids with $m = 4$, $\theta_w = 90°$ with the experimental data of Coertjens *et al.*[43]

solid curve) but not for the flat interface models, suggesting that the interface is deformed rather than flat during particle adsorption. Note that in Figure 4-3, the experimental relaxation data for ϕ is clearly non-logarithmic.

Using the fitted value of β for the black curve ($\beta = 16\ s$) and assuming $\gamma_{ow} = 50mM \cdot m^{-1}$ yields $\lambda = 10^{-2} kg\ s^{-1}$. It is instructive to compare this value for λ with that due to the bulk fluid viscosity. For prolate ellipsoids with $m > 2$, the rotational friction coefficient due to the viscosity of the surrounding medium η can be approximated by[130,131]

$$\mu = \frac{16\pi\eta a^3}{3[2\ln(2m)-1]} \qquad \textbf{(4-8)}$$

Combining the above equation with the ratio $\frac{\mu}{\lambda} = \frac{4(a^2+b^2)}{9}$ assumed in Scaling 2, the translational friction coefficient is given by

$$\lambda = \frac{12\pi\eta a^3}{(a^2+2b^2)[2\ln(2m)-1]} \qquad \textbf{(4-9)}$$

For the experimental system of Coertjens *et al.*[43], $\eta = 20mPa\ s$, $a = 1200nm$, $b = 300nm$ and $m = 4$. Inserting these values into Equation 4-9, we obtain $\lambda = 2.5 \times 10^{-7} kg\ s^{-1}$ which is more than four orders of magnitude smaller than the value

obtained from fitting the experiments in Figure 4-3. This huge discrepancy between the viscous model and experiment suggests that the adsorption dynamics in these experiments is not controlled by viscous forces but (as we shall see in a moment) by contact line forces.

In principle, as the particle approaches the interface and the gap between the particle surface and the interface tends toward zero, the viscous force involved in pushing the liquid out of the gap (i.e., the lubrication force) diverges.[132] However, as the liquid film separating the interface and the particle thins, the film will become unstable due to molecular forces such as van Der Waals interactions, leading to the film inevitably rupturing causing the particle to attach to the interface.

The good fit between our Langevin model and experiment suggests that for this system, we can quantitatively model the effect of contact line pinning by renormalising the friction coefficient of the particle, similar to what was found by Boniello *et al.* for the in-plane diffusion coefficient of particles at a liquid interface.[92] The physical origin of the contact line pinning models is the interaction between the three-phase contact line and nanoscale defects on the surface of a particle. Heterogeneities on the surface of the particle from either surface chemistry or geometric defects, can locally satisfy Young's constant contact angle requirement and cause the three-phase contact line to pin at such sites, requiring an input of energy to overcome the potential barrier in the form of thermal fluctuations. Note that the renormalisation of friction coefficients due to contact line pinning is not merely a phenomenological fitting exercise. Instead, a microscopic basis for this procedure has been provided by Boniello *et al*. [92] who explicitly showed that taking into account the thermally activated fluctuations of the contact line via the fluctuation-dissipation theorem leads to significant enhancements of particle friction coefficients. The underlying assumptions in the derivation of the renormalising

factor being that thermally activated deformations of the interface at the three-phase contact line drive the system out of mechanical equilibrium and result in extra random forces on the particle.

Adapting such an approach to our problem, the contribution from contact line fluctuations to the translational friction coefficient is given by the fluctuation-dissipation theorem as[133]

$$\lambda = \frac{1}{2k_BT}\langle f(0)^2\rangle\tau_c \qquad \textbf{(4-10)}$$

where k_BT is the thermal energy, $f(0)$ is the instantaneous surface tension force exerted by the liquid interface on a triple-line segment of length ℓ_D between neighbouring nanoscale surface defects and τ_c is the correlation time of the fluctuations. The random nature of the fluctuations allows us to write the mean squared force as

$$\langle f(0)^2\rangle \approx n(\gamma_{ow}\ell_D)^2 \qquad \textbf{(4-11)}$$

where $n = 2\pi\left[(a^2+2b^2)/3\right]^{1/2} \Big/ \ell_D$ is the number of uncorrelated triple-line segments around the ellipsoid. On the other hand, the correlation time due to the thermally activated jumps of the contact line has the Arrhenius-like form[134]

$$\tau_c \approx \frac{\eta V_m}{k_BT} exp\left[\frac{\ell_D^2\gamma_{ow}(1+\cos\theta_w)}{k_BT}\right] \qquad \textbf{(4-12)}$$

where $V_m \approx 3\times10^{-29}m^3$ is the molecular volume of water.

Substituting Equations 4-11, 4-12 into Equation 4-10, we obtain an expression for the friction coefficient λ involving only one fitting parameter, namely the distance between surface nanoscale defects ℓ_D. Using the value $\lambda = 10^{-2}kg\ s^{-1}$ obtained from fitting the experimental data in Figure 4-3 and the experimental parameters for ref.[43] discussed above, we obtain $\ell_D \approx 0.9nm$. This nanometric value for ℓ_D is physically reasonable and provides support that contact line pinning is indeed what gives rise to the significantly enhanced value for the friction coefficient.

We next compare our theoretical model with the experiments of Wang *et al.*[44] for polystyrene ellipsoids with polystyrene ellipsoids where $a \approx 2.6\mu m$, $b \approx 1\mu m$, $m \approx 2.6$ at a hexane/water interface under standard conditions. We note that in this set of experiments particles were guided to the interface with an optical trap as opposed to using a density mismatch technique. The adsorption process for this system is much faster, occurring on the $\sim 0.03\ s$ timescale. Once again, for θ_w we use the dynamic contact angle measured for an equivalent sphere on this timescale which is $\theta_w = 45°$[89]. The digital holography technique used by Wang *et al.* is capable of measuring both ϕ and h as a function of time, allowing us to compare theory and experiment for both the dynamics of the individual coordinates (i.e., ϕ and h vs. t) and the adsorption trajectory (i.e., ϕ vs h). The latter representation of the data is particularly useful as it allows us to perform a parameter-free comparison between theory and experiment.

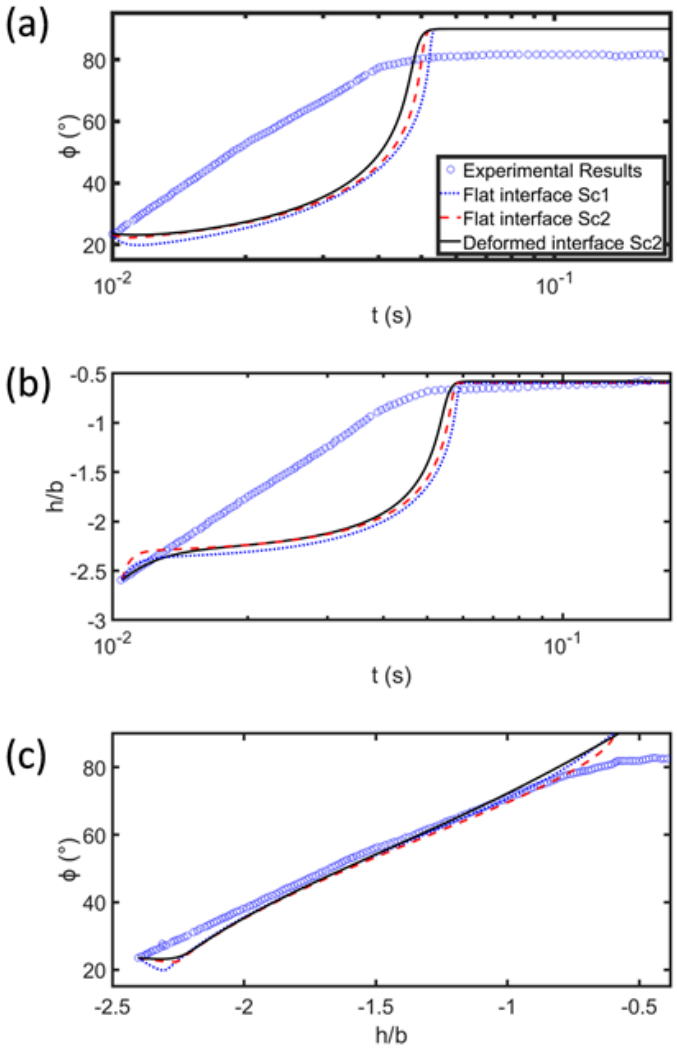

Figure 4-4 Comparison of the three theoretical models discussed in the main text for ellipsoids with $m = 2.6$, $\theta_w = 90°$ with the experimental data of Wang *et al.*[44] for (a) linear-log plot of ϕ vs. t, (b) linear-log plot of h/b vs. t (c) ϕ vs. h/b.

In Figure 4-4 (a, b), we compare all three models discussed above with linear-log plots of the experimental data for the average value of ϕ vs.t (Figure 4-4a) and h/b vs. t (Figure 4-4b). We note that, in contrast to Figure 4-3, the experimental dynamics of the individual adsorption co-ordinates are logarithmic. We also note that none of the three theoretical models can reproduce the experimental data in Figure 4-4, even if we renormalise the friction coefficients to account for contact line pinning. The discrepancy between theory and experiment is perhaps not surprising since, as pointed out in refs.[89,92], it is not possible for a Langevin model where dissipative forces are

parameterised by a handful of friction coefficients to generate the hierarchy of timescales required for logarithmic dynamics. However, the discrepancy between theory and experiment seen in Figure 4-4 also highlights the fact that the contact line dynamics in the experiments of Wang *et al.*[44] is qualitatively different from that of Coertjens *et al.*[43] (Figure 4-3). We will discuss possible reasons for this difference at the end of this section.

However, while the theoretical models are not able to capture the dynamics of the individual adsorption coordinates, in Figure 4-4c we see that they are able to capture adsorption trajectory (i.e., ϕ vs. h/b plot) of the experimental system surprisingly well. In particular, all three models are able to reproduce the essentially linear relationship between ϕ and h found experimentally with no fitting parameters. It is also interesting that apart from small discrepancies in the early-stage dynamics, all three models predicts very similar adsorption trajectories.

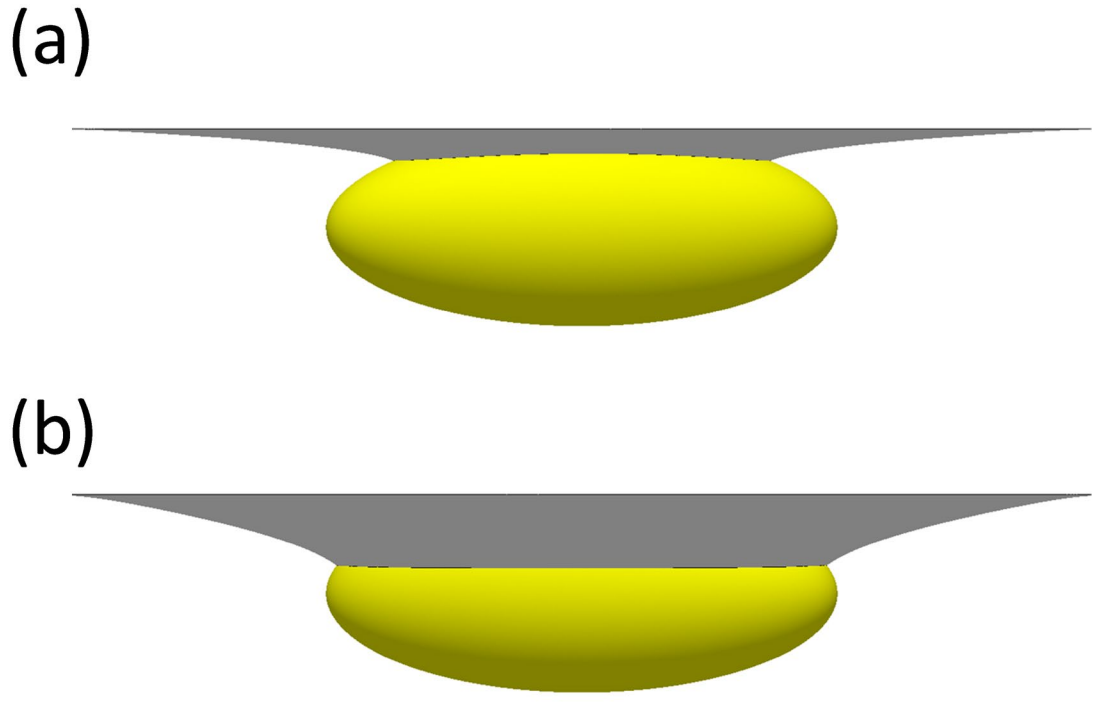

Figure 4-5 Interfacial deformation calculated from Surface Evolver for an ellipsoid with $m = 2.6$, $\phi = \pi/2$, $h = -h_c$ for contact angle (a) $\theta_w = 45°$ and (b) $\theta_w = 90°$.

We believe that the similarity between the flat and deformed interface models (with Scaling 2) in Figure 4-4c is due to the fact that the interfacial deformation during particle adsorption is small when we are far from the neutrally wetting regime (recall that the effective contact angle relevant to the experiments in ref.[44] is $\theta_w = 45°$. This is illustrated in Figure 4-5 where we show the deformed liquid interface around an ellipsoid with $m = 2.6$, $\phi = {}^{\pi}/_{2}$ $h = -h_c$ for contact angle $\theta_w = 45°$ (Figure 4-5a) and $\theta_w = 90°$ (Figure 4-5b). We see that deformation of the liquid interface for $\theta_w = 45°$ is much smaller compared to $\theta_w = 90°$ (average height of contact line is $-0.289b$ and $-0.734b$ in Figure 4-5 a and b respectively). The small interfacial deformation far from the neutrally wetting regime may also explain why the flat interface approximation works so well in modelling the experimental data of Wang *et al*.[44] However, we emphasize that the flat interface approximation is not accurate in general. Specifically, close to the neutrally wetting condition, significant discrepancies emerge between the flat and deformed interface models (see Figure 4-3).

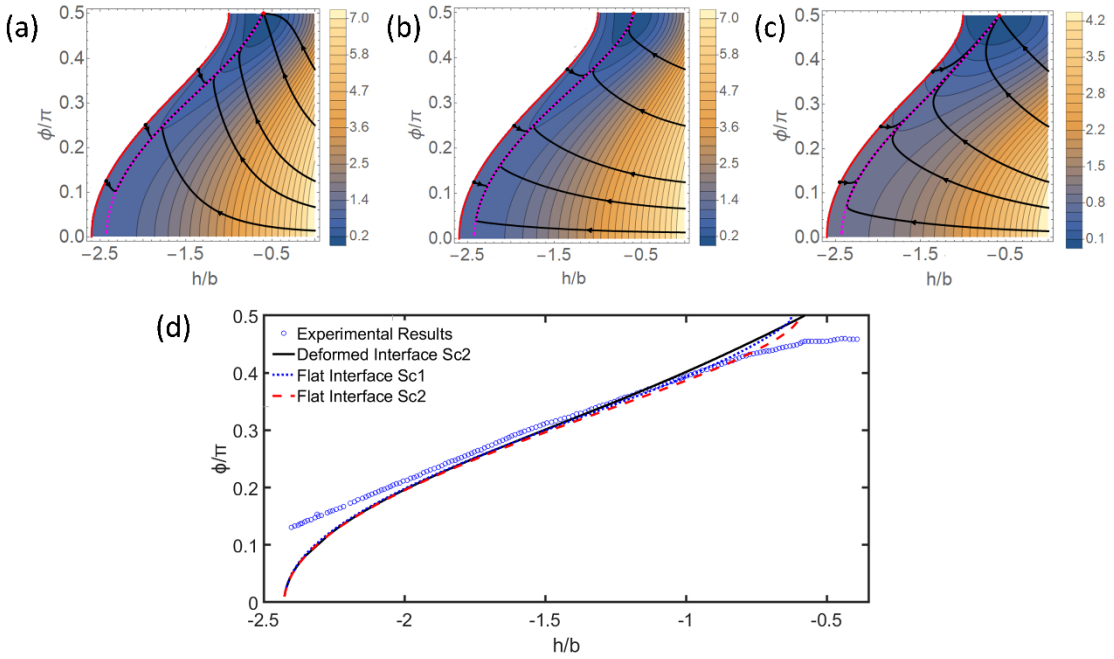

Figure 4-6 (a)-(c) Adsorption trajectories in the (h, ϕ) plane, $h < 0$ (black lines), for ellipsoids with contact angle $\theta_w = 45°$, aspect ratio $m = 2.6$ for (a) flat interface and Scaling 1, (b) flat interface and Scaling 2, (c) deformed interface and Scaling 2. The trajectories are superposed on contour plots of free energy landscapes and the red curve bounding the landscape corresponds to particles touching the interface from the water side. Note that in (a)-(c), the adsorption trajectories converge onto dynamical attractors which roughly lie along the valley of the free energy landscape. (d) Comparison of dynamical attractors from (a)-(c) with the experimental adsorption trajectories for polystyrene ellipsoids from Wang *et al.* [44]

The similarity between the Scaling 1 and Scaling 2 models (with flat interface) in Figure 4-4c is most likely due to the fact that far from the neutrally wetting regime, all particle adsorption flow lines converge onto a 'dynamical attractor' after the initial stages of the adsorption.[21] This is illustrated in Figures 4-6(a-c) where we clearly see the emergence of an attractor in the adsorption flow lines for all three models. The attractor is formally defined as the locus of points in the free energy landscape $F^*(h^*, \phi^*)$ where one of the eigenvectors of the Hessian matrix $\vec{\nabla}\vec{\nabla}^T F^*$ (the one with positive eigenvalue or principal curvature) is parallel to the gradient of the free energy[21] and the resultant attractor is in general sensitive to the dynamic scaling assumed. However, far from the neutrally wetting regime, the free energy landscape develops a narrow valley (see Figures 4-6(a-c)), and since attractors are constrained to be in the vicinity of this valley,

the attractors effectively become insensitive to the dynamic scaling used. This point is illustrated in Figure 4-6d where we see that the attractors from all three models are essentially the same. This explains why, apart from small discrepancies in the early-stage dynamics, the Scaling 1 and Scaling 2 models with flat interface (and indeed Scaling 2 model with deformed interface) predict very similar adsorption trajectories in Figure 4-4c.

The fact that far from the neutrally wetting regime, dynamic attractors are essentially determined by the geometry of the free energy landscape rather than the dynamic scaling model may also explain why in Figure 4-4c, all three theoretical models are able to capture the main features of the experimental adsorption trajectory even though they cannot capture the dynamics of the individual adsorption coordinates. This point is evidenced in Figure 4-6d where we see that, after the initial stages of the adsorption, the experimental adsorption trajectory (data points) largely coincides with the dynamic attractors of all three models (lines).

Another reason why our theoretical models are able to capture the adsorption trajectory in Figure 4-4c even though they cannot capture the time dependence of the individual adsorption coordinates may be because the coupling between ϕ and h in our Langevin model comes from the capillary forces alone, and these forces depend only on particle configuration and are independent of the frictional forces (see Equations 4-3,4-4). This means that these models may still be able to capture the coupling between ϕ and h accurately even if they do not correctly capture the frictional forces resisting particle adsorption.

Finally, we note that the experimental trajectory deviates from the theoretical models in the late stages of the adsorption in Figures 4-4c & 4-6d. This deviation is most likely due to the fact that when the experimental system is close to the equilibrium tilt

angle of $\phi = 90°$ the capillary force driving particle adsorption becomes too small to overcome contact line pinning so that the ellipsoid becomes kinetically arrested and therefore cannot reach the equilibrium tilt angle.[89]

Before leaving this section, we return to the interesting question about why the contact line dynamics seen in the experiments of Wang *et al.*[44] are so different from that of Coertjens *et al.*[43] To frame this discussion in a broader context, it is interesting that contact line dynamics can be modelled by renormalising friction coefficients in some systems, e.g., refs.[43,92] but not others, e.g., refs.[44,89] We speculate that this difference could be due to large differences in the nanoscale surface defect density between the two sets of systems, which in turn lead to very different contact line dynamics. For example, for the polystyrene spheres at the air/water interface studied in ref.[92], the area per defect was determined to be $A = \ell_D \approx 0.2nm^2$, while for the polystyrene spheres at the oil/water interface studied in ref.[89], the area per defect was determined to be in the range $A \approx 5 - 30nm^2$. Interestingly, for the polystyrene ellipsoids studied in ref.[43], from the data in Figure 4-3 we determined a rather small area per defect of $A = \ell_D \approx 0.8m^2$, consistent with our speculation above.

In order to test this hypothesis we use the contact line hopping model of *Kaz et al.*[89] to calculate the contact line dynamics (i.e., particle height vs. time) for the two spherical particle systems discussed above. The configuration of a sphere of radius R at any instant during adsorption can be described by the height of the particle apex above the liquid interface z as illustrated in Figure 4-7. Assuming the liquid interface remains flat during particle adsorption, z is related to the dynamic contact angle θ_D

$$z = R(1 - cos\,\theta_D) \qquad \textbf{(4-13)}$$

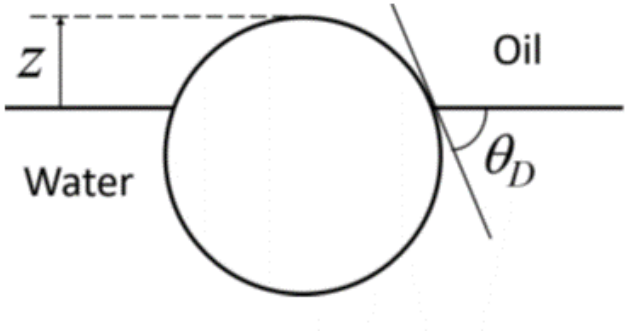

Figure 4-7 Variables used in the model of Kaz *et al.*[89] to characterize the configuration of a sphere adsorbing at a liquid interface.

Using the contact line hopping model of Blake *et al.*[79], Kaz *et al.*[89] derived the following equation of motion for z:

$$R\dot{z} = \sqrt{z(2R - z)}V_0 e^{-U/kT+\gamma A(\cos\theta_D - \cos\theta_E)/2kT} \quad \textbf{(4-14)}$$

where $\dot{z}$ is the z velocity of the particle, kT is the thermal energy, V_0 is the molecular hopping speed, U is the energy barrier to molecular hopping at the contact line due to nanoscale surface defects on the colloid, A is the area per surface defect, γ is the surface tension of the liquid interface, and θ_E is the equilibrium contact angle. Substituting Equation 4-13 into Equation 4-14, we can replace θ_D with z to get

$$R\dot{z} = \sqrt{z(2R - z)}V_0 exp\left[-\frac{U}{kT} + \frac{\gamma A}{2kT}\frac{(z_E - z)}{R}\right] \quad \textbf{(4-15)}$$

where $z_E = R(1 - \cos\theta_E)$. Finally, using scaled variables $\bar{z} = z/R$, $\bar{t} = t/\tau$ where $\tau^{-1} = \frac{V_0}{R} exp\left(-\frac{U}{kT}\right)$, we can write Equation 4-15 more compactly as

$$\frac{d\bar{z}}{d\bar{t}} = \sqrt{\bar{z}(2 - \bar{z})}exp[a(\overline{z_E} - \bar{z})] \quad \textbf{(4-16)}$$

where $a = \frac{\gamma A}{2kT}$ is the dimensionless area per defect. Equation 4-16 is a first-order, separable ODE which can be easily solved to find $\bar{t}$ as a function of $\bar{z}$,

$$\bar{t} = \int_0^{\bar{z}} \frac{d\bar{z}\prime}{\sqrt{\bar{z}\prime}(2 - \bar{z}\prime)exp[a(\bar{z}_E - \bar{z}\prime)]} \quad \textbf{(4-17)}$$

where the range of $\bar{z}$ is $0 \leq \bar{z} \leq \bar{z}_E$.

For the sulphate terminated polystyrene spheres at an oil-water interface studied by Kaz *et al.*[89], $\theta_E \approx 110°$, $A \approx 5\,nm^2$, $\gamma = 37\,mNm^{-1}$, and therefore $a \approx 23$. In Figure 4-8(a) we show the linear-log plot of $\bar{z}$ versus $\bar{t}$ calculated from Equation 4-17 for these parameters. We see that the relatively large value of A in this case leads to an essentially logarithmic time dependence for $\bar{z}$ (or h). On the other hand, for the sulphate or amidine terminated polystyrene spheres at an air-water interface studied by Boniello *et al.*[92], $\theta_E \approx 45°$, $A \approx 0.18\,nm^2$, $\gamma = 71\,mNm^{-1}$, and therefore $a \approx 1.6$. In Figure 4-8(b) we show the linear-log plot of $\bar{z}$ versus $\bar{t}$ calculated from Equation 4-17 for these parameters. We see that the relatively small value of A

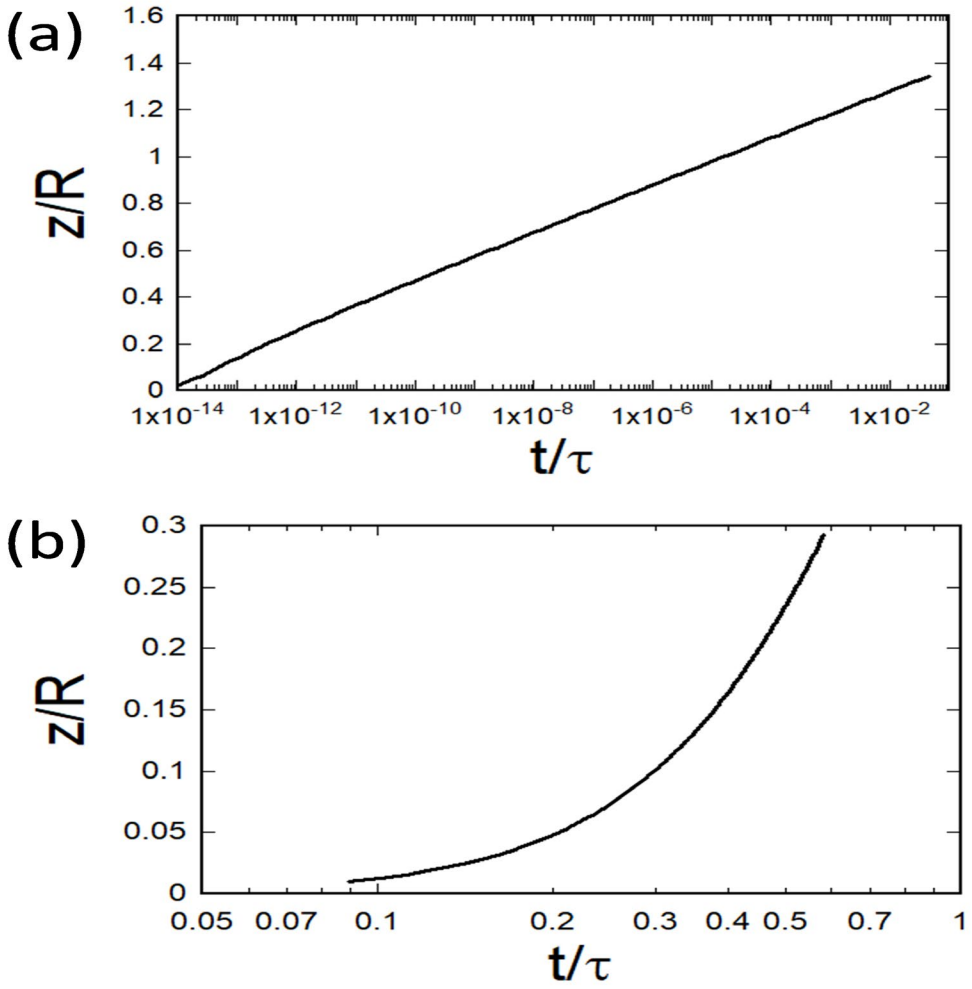

Figure 4-8 Linear-log plot of normalised height $\bar{z}$ vs. normalised time $\bar{t}$ for micro-spheres adsorbing at a liquid interface calculated from contact-line hopping model for experimental parameters from systems studied by (a) Kaz *et al.*[89]and(b) Boniello *et al.*[92]

in this case leads to a nonlogarithmic time dependence for $\bar{z}$ (or h).

Note that contact line pinning may arise from nanoscale surface features due to chemical[89], topological[129] or charge[135,136] heterogeneities. This means that small differences in surface chemistry or sample preparation protocols may lead to large differences in contact line dynamics, even between systems which are nominally similar. Regardless of the exact microscopic origin for the different contact line dynamics, what seems clear from comparing the different experimental data on interfacial colloid dynamics is that while contact line pinning always leads to slower wetting dynamics, the logarithmic time dependence may not be universal but may be system dependent. This may explain why contact line dynamics can be modelled by renormalising friction coefficients in some systems but not others.

4.4 Conclusions

In summary, we have developed a simple Langevin model which accurately captures the deformation of the liquid meniscus and uses the correct ratio for the translational and rotational particle friction coefficients. The effect of contact line pinning is incorporated into the model by renormalising particle friction coefficients and using the appropriate dynamic contact angle. Using this simple model, we were able to reproduce the monotonic variation of particle orientation with time that is observed experimentally. Specifically, we were able to obtain this behaviour by accurately modelling interfacial deformation and particle friction coefficients without the need to explicitly invoke depinning dynamics of the contact line. We were also able to quantitatively model the adsorption dynamics of the individual adsorption coordinates (i.e., adsorption coordinate vs. time) for some experimental ellipsoidal systems but not others. However, even for the latter case, our model was able to accurately capture the adsorption trajectory (i.e., particle orientation vs. height) of the particles.

Our model clarifies the different roles played by capillary, viscous and contact line forces in determining the wetting dynamics of micron-scale objects. Note that since the final equilibrium state of the anisotropic particle is controlled by its adsorption trajectory rather than by the adsorption dynamics of the individual coordinates, our theoretical model can be used as a predictive tool for designing and controlling the assembly of complex particles at liquid interfaces and for future work we plan to use it to study the adsorption of particles with other non-spherical geometries.

Chapter 5 Adsorption Dynamics of Cylindrical Colloids at The Liquid Interface

5.1 Introduction

The adsorption of colloids at liquid interfaces has generated increasing interest in recent years because of potential applications in areas such as emulsification[5], encapsulation[121], nanostructured materials[6,137] and reconfigurable systems.[138] More fundamentally, interfacial colloids have paved the way for the creation of exotic new states of matter such as liquid marbles, bijels and 'dry' water.[123,124,126] Up to now, most of the research in this area has focused on spherical or nearly spherical particles. However, advances in synthetic methods have made possible the fabrication of anisotropic particles such as ellipsoids[10,18,19,48,67,139], cylinders[20,25,45], cubes[39,63,68,98,99] and more complex shapes.[14,16] The behaviour of such shape anisotropic particles at fluid interfaces is richer than that of spherical particles as anisotropic particles can adopt multiple locally stable orientations at the liquid interface.[25,39,45,63,68,98,99] The possible stable orientations of anisotropic particles at liquid interfaces are strongly dependent on the shape of the anisotropic particle. For example, ellipsoidal particles are always 'side-on' (particle long axis parallel to liquid interface)[48,67], cylindrical particles can be either 'side-on' or 'end-on' (particle long axis perpendicular to liquid interface)[25,45] while cubes can be face-up, edge-up or corner-up.[39,63,68,98,99]

The fact that cylindrical colloids can adopt the end-on state at the liquid interface is particularly interesting for many novel applications since arrays of vertically aligned nanorods can be used as epsilon-near-zero or hyperbolic metamaterials[26,140–144], plasmonic cavity resonators[145] or in surface enhanced

Raman spectroscopy (SERS) for sensing applications.[141,146–149] Vertically aligned nanorod arrays are particularly versatile platforms for sensing and enhanced spectroscopies since the nanorods can be constructed from a wide variety of materials, including metals (e.g., gold, silver, aluminum, copper etc.) and dielectrics (e.g., polymers, silica etc.), providing maximum flexibility for tuning the frequency range over which the array has desired properties.[142,150–153] One option for creating vertical nanorod arrays is to use nanolithography[154], but such top-down methods have low throughput, complex fabrication protocols and low scalability. An alternative approach is to use bottom-up self-assembly on solid substrates such as electrodeposition[151–153] or evaporation driven assembly.[148,155–157] These approaches allow one to create high quality vertically aligned nanorod monolayers over large areas (cm-scale), but the solid nature of the substrates used to template the array limits the possibilities for post-processing to vary monolayer properties such as the spacing between nanorods.

In recent years, the self-assembly of particles at liquid interfaces has emerged as a powerful method for creating dimensionally confined nanostructures.[138,158–160] Once these structures have been assembled at the liquid interface, the spacing between particles can be tuned through compression or the use of coated nanoparticles and the final structures can be transferred to a solid substrate and immobilised to create functional nanomaterials.[160–164] For example, Kim *et al.* have recently demonstrated that they can prepare vertically aligned nanorod monolayers through the adsorption of gold nanorods (GNRs) at a liquid interface.[149] Specifically, by exploiting the differential surface chemistry between the tips and sides of their GNRs and by a suitable choice of the two bulk liquid phases, they were able to engineer the end-on state to be the thermodynamic

ground state so that the GNRs spontaneously formed a vertically aligned monolayer at the liquid interface. However, while this assembly method is very attractive due to its simplicity, it is extremely challenging in general to engineer nanoparticles to have specific patchy particle surface chemistries, so this method may be challenging to generalize to other nanorod systems.

A more generic method for assembling vertically aligned nanorods at a liquid interface has been proposed by de Graaf *et al*. which is based on adsorption *kinetics* rather than thermodynamics.[21] Using a simple viscous-based Langevin model, these authors showed that the final orientation of cylindrical colloids at a liquid interface is determined by the 'attack' angle of the cylinder, i.e., the initial orientation of the cylinder when it first contacts the liquid interface. In particular, they showed that for a range of attack angles, the final orientation of the cylinder is the end-on state, even if the side-on state is the thermodynamic ground state. The range of attack angles which lead to the end-on state in turn depends on system parameters such as particle contact angle, aspect ratio and which bulk phase the cylinder approaches the liquid interface from. This assembly method relies on adsorption kinetics rather than the nanoparticles having a specific surface chemistry, therefore it is applicable to nanorod systems made from a wide range of materials and represents a versatile platform for engineering vertically aligned nanorods for specific applications.

While the viscous-based model of de Graaf *et al.* serves as a useful initial guide to experiments, it does not include a number of important effects. Firstly, the model uses a physically unrealistic ratio for the translational to rotational friction coefficients.[21,84] Secondly, it neglects the deformation of the liquid meniscus around the adsorbing particle which is significant for particle adsorption in the low capillary number regime.[18–

[20,25,63,67] Finally, the model neglects the effect of contact line pinning which has been shown to lead to adsorption kinetics which are orders of magnitude slower than what is predicted by viscous-based models.[43,44,89] In principle, some of these limitations can be addressed using particle-based simulations such as Lattice-Boltzmann simulations.[22] However, it is not possible for current simulations to simultaneously achieve the very long timescales required to access the low capillary and Reynolds number regimes that are relevant to the experiments. We refer the reader to Section 2.2 for a more detailed discussion and comparison of the adsorption kinetics of anisotropic particles from both an experimental and theoretical perspective.

In this chapter, we extended the Langevin model of de Graaf *et al*. to incorporate interfacial deformation, the correct ratio for particle friction coefficients and contact line pinning. Specifically, interfacial deformation was accurately captured in our model by coupling Langevin dynamics to a finite element model for the interface. Using this model, we were able to reproduce much of the reported experimental phenomenology for the adsorption of ellipsoidal particles. For example, we were able to quantitatively model the evolution of particle orientation with time in some experimental systems[43], and even for systems where this was not possible, we were able to accurately model the adsorption trajectory (i.e., particle orientation vs. particle height) of the ellipsoids.[44] Since the range of attack angles giving rise to the end-on state is controlled by the adsorption trajectory rather than the dynamics of the individual adsorption coordinates per se (see later), our model allows us to accurately determine the final orientation nanorods at a liquid interface.

The aim of this chapter is to use our Langevin model to study the adsorption kinetics of cylinders at a liquid interface in order to quantitatively determine the conditions required to prepare cylindrical nanorods in the end-on state. Our calculations

will help guide experiments to use adsorption kinetics as a low cost and versatile method for preparing vertically aligned nanorod monolayers as metamaterials.

The rest of the chapter is organised as follows. In Section 5-2, we provide details of the Langevin model we use to study the adsorption kinetics of cylindrical particles at a liquid interface. In section 5-3, we use this theoretical model to determine the conditions required to kinetically assemble cylindrical nanorods into vertically aligned monolayers. Based on these theoretical results, in section 5-4 we discuss the feasibility of using our kinetic assembly method to experimentally prepare vertically aligned cylindrical nanorods at the liquid interface. Finally, in section 5-5 we present our conclusions.

5.2 Theoretical Model

5.2.1 Thermodynamics of Nanorod Adsorption

We consider a cylindrical particle adsorbing at a liquid interface with long and short axis a, b respectively and aspect ratio $m = \frac{a}{b}$ (Figure 5-1). For definiteness, we refer to the top and bottom liquid phases as oil and water respectively. The configuration of the cylinder at any instant during its adsorption is described by two degrees of freedom, namely the height of the particle center relative to the height of the undisturbed interface h, and the angle between the particle's long axis and the normal to the undisturbed interface ϕ. Note that we use the sign convention where the particle centre is in the water phase for $h < 0$ and in the oil phase for $h > 0$. Note also that due to symmetry, we only need to consider ϕ values in the range $0° \leq \phi \leq 90°$.

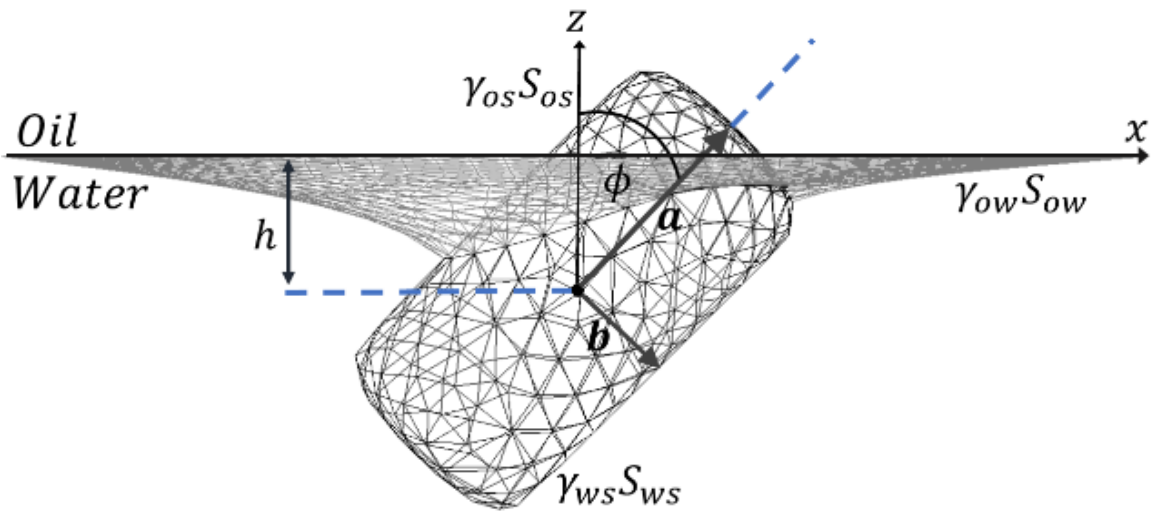

Figure 5-1 Geometry of cylindrical nanorod adsorbing at a liquid interface. The illustrated nanorod has aspect ratio $m = 2.5$ and sharpness parameter $\eta = 20$.

For sub-micron particles, which are the focus of this chapter, gravity is negligible and the free energy of the system is primarily due to interfacial energy and is therefore given by [48,84]

$$F(h,\phi) = \gamma_{ow}S_{ow} + \gamma_{os}S_{os} + \gamma_{ws}S_{ws} \quad \textbf{(5-1)}$$

where γ_{ow}, γ_{os} and γ_{ws} are the interfacial tensions and S_{ow}, S_{os} and S_{ws} are the areas of the oil/water, particle/oil and particle/water interfaces respectively. Using $S_{ws} = S - S_{os}$ where S is the total area of the particle, Young's equation $\gamma_{ow}\cos\theta_w = \gamma_{os} - \gamma_{ws}$ where θ_w is the contact angle and dropping irrelevant constant terms, we can simplify Equation 5-1 to

$$F(h,\phi) = \gamma_{ow}(S_{ow} + \cos\theta_w S_{os}) \quad \textbf{(5-2)}$$

Note that we have neglected line tension contributions in Equations 5-1 and 5-2 as these are sub-dominant compared to interfacial tensions for the typical nanorod systems that we are considering where $a, b > 10nm$.[129]

For a given particle configuration (h,ϕ), the free energy given by Equation 5-2 is calculated using the finite element package Surface Evolver.[25,48,114] One problem with using finite element methods to study cylinders is that they become numerically

unstable when the three phase contact line crosses the sharp edge of the cylinder.[25] To overcome this problem, we approximate the cylinder using the super-ellipsoid equation[117]

$$g(x,y,z) = \left(\frac{x'}{a}\right)^{\eta} + \left(\frac{y'}{b}\right)^{2} + \left(\frac{z'}{b}\right)^{2} = 1 \qquad \textbf{(5-3)}$$

where η is an even integer that controls the sharpness of the cylinder edge, with $\eta = 2$ and $\eta = \infty$ corresponding to the limiting cases of an ellipsoid and a cylinder with infinitely sharp edges respectively. In most of our calculations we use $\eta = 20$ which corresponds to a cylinder with slightly rounded edges (see Figure 5-1), though we also consider lower values of η in section 5.3.3 to model experimentally realistic cylinders which have more rounded edges. In Equation 5-3, x, y, z correspond to lab frame coordinates where z and x, y lie perpendicular and parallel to the unperturbed liquid interface respectively (see Figure 5-1), x', y', z' to particle frame coordinates where z' and x', y' lie along the long and short axes of the particle respectively, and the two coordinate systems are related to each other through a rotation of angle ϕ about the y-axis.[62] The particle height when it first contacts the liquid interface, $h_c(\phi)$, is a key quantity in the adsorption process and can be determined from the condition that at the point of contact, the particle surface normal vector $\boldsymbol{\nabla} g(x,y,z)$ is parallel to the z direction, where $\boldsymbol{\nabla}$ is the 3D grad operator in the lab frame and the function g is given by Equation 5-3. Solving the three simultaneous equations $\frac{\partial g}{\partial x} = \frac{\partial g}{\partial y} = 0$ and Equation 5-3 allows us to find the coordinates of the contact point and $h_c(\phi)$ is given by the z contact coordinate.

The interfacial areas and free energy in Equation 5-2 depend sensitively on the boundary condition at the three-phase contact line. The original study by de Graaf *et al*. assumed that the liquid meniscus remains flat.[21] A more realistic

boundary condition is that the liquid meniscus is deformed due to the constant contact angle requirement.[19,20,25,45,63,67,84] We call these boundary conditions 'flat interface' and 'deformed interface' respectively and consider both limiting cases in our study. For both cases, the interfacial energy $F(h,\phi)$ is first calculated for (h,ϕ) values on a 101×37 non-equidistant grid for $h \in [-h_c(\phi), h_c(\phi)]$ and $\phi \in [0,\pi/2]$. The data on this grid are then interpolated with a third order interpolation scheme to yield the full energy landscape. To check that this grid resolution is sufficient, for selected cases we performed calculations on a higher resolution 202x180 grid and found no discernable differences in the final result.

5.2.2 Kinetics of Nanorod Adsorption

The adsorption trajectory of the cylinder is found by solving the Langevin equation for the particle at the liquid interface in the same manner as detailed in Section 4.2. In the low Reynolds number regime where inertial forces are negligible, this is given by the scaled coupled differential equations

$$\frac{dh^*}{dt^*} = -\frac{\partial}{\partial h^*} F^*(h^*,\phi^*) \qquad \textbf{(5-4)}$$

$$\frac{d\phi^*}{dt^*} = -\frac{\partial}{\partial \phi^*} F^*(h^*,\phi^*) \qquad \textbf{(5-5)}$$

We refer the reader to Section 4.2 for a full derivation and explanation of Equations 5-4 & 5-5 and note that in the following we use an identical approach.

By solving Equations 5-4 & 5-7, we obtain the adsorption trajectory $(h(t),\phi(t))$ for different attack angles, i.e., the initial orientations of the cylinder when it first contacts the liquid interface. In ref.[84], we showed that the most accurate results for the adsorption trajectories of ellipsoids were obtained for the deformed interface boundary condition and Scaling 2. However, in order to compare our results with the previous work of de Graaf *et al.* and to study the impact of different contact line boundary

conditions and dynamical scaling's on the adsorption kinetics of cylinders, in what follows we calculate the adsorption trajectories for three scenarios, a flat interface with Scaling 1, a deformed interface with Scaling 1 and a deformed interface with Scaling 2. In what follows, we refer to these three scenarios as models 1, 2 and 3 respectively.

5.3 Results

5.3.1 Stable States of Cylinders at a Liquid Interface

Before calculating the adsorption trajectories of cylindrical particles, we first calculate the stable states of the particles at a liquid interface (i.e., local or global energy minima) as these represent the end points of the adsorption trajectories. In Figure 5-2, we show the interfacial energy as a function of tilt angle ϕ for cylinders with different contact angles and aspect ratios, where the interfacial energy at each ϕ is minimised

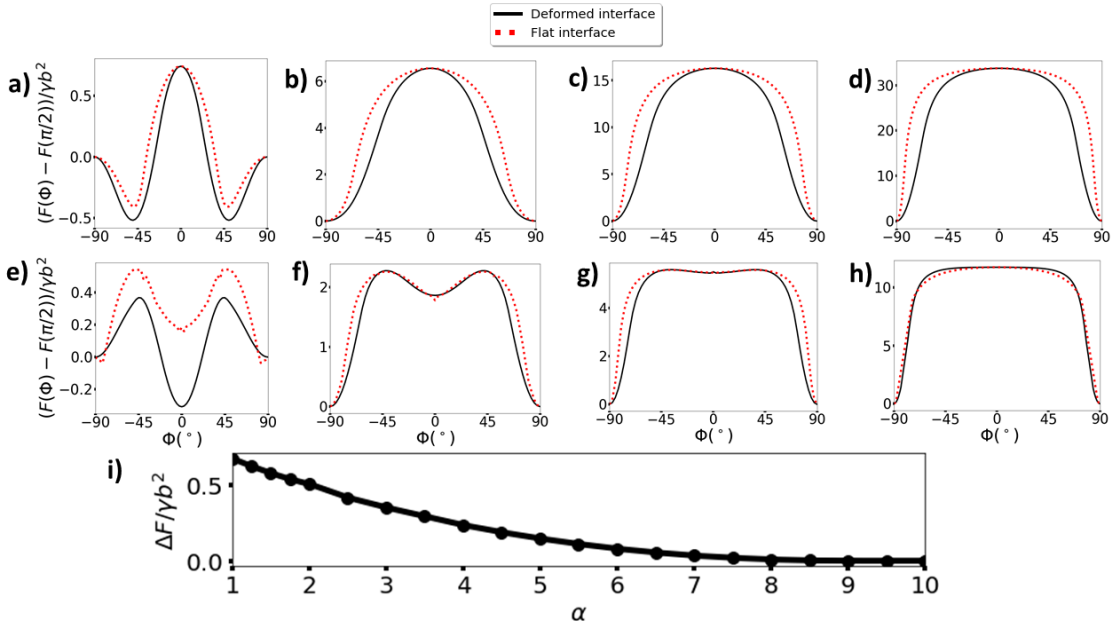

Figure 5-2 (a-h) Interfacial energy as a function of tilt angle ϕ for cylinders with $\eta = 20$, where the interfacial energy at each ϕ is minimised with respect to the particle height h, for contact angles $\theta_w = 90°$ (top row) and $\theta_w = 120°$ (bottom row) and for aspect ratios $m = 1$ (a, e), $m = 2.5$ (b, f), $m = 5$ (c, g) and m=9.5 (d, h). The dashed red lines and solid black lines are calculated using the flat interface model and deformed interface model respectively. (i) Energy barrier for transition from end-on state to side on state as a function of aspect ratio for cylinders with $\eta = 20$, $\theta_w = 120°$ calculated using the deformed interface model.

with respect to the particle height h. The top and bottom rows show results for neutrally wetting cylinders ($\theta_w = 90°$) and hydrophobic cylinders (illustrated by $\theta_w = 120°$), while the first, second, third and fourth columns show results for aspect ratios $m = 1, 2.5, 5, 9.5$. The dashed red lines and solid black lines are calculated using the flat interface model and deformed interface model respectively. We see that the deformed interface model generally yields a lower energy compared to the flat interface model at any given value of ϕ. This is not surprising since the constant contact angle condition comes from minimizing interfacial energy. Note that the stable states of the system are independent of the assumed dynamical scaling model.

For neutrally wetting cylinders (Figure 5-2(a)-(d)), both the flat and deformed interface models predict that there is only one stable orientation for the cylinder. Specifically, for $m = 2.5$ and 5, the equilibrium state is the side-on state $\phi = \pm 90°$ while for $m = 1$, the equilibrium state is the tilted state, with a tilt angle $\phi = \pm 49.6°$ for the deformed interface model (note that positive and negative ϕ represent equivalent states). These results are in good agreement with a previous study[25] where it was shown that below a critical aspect ratio of $m_c = 2.3$, the equilibrium orientation of neutrally wetting cylinders at a liquid interface transitions from the side-on state to the tilted state.

In contrast, for hydrophobic cylinders (Figure 5-2(e)-(h)), both models predict that, provided the aspect ratio is not too large, there are two stable cylinder orientations, namely the side on state $\phi = \pm 90°$ and the end-on state $\phi = 0°$ with the cylinders being mainly immersed in the oil phase in both states, i.e., $h > 0$, see Figure 5-3(b)-(d). For small aspect ratio cylinders $m = 1$, the deformed interface model predicts that the end-on state is the ground state and the side-on state is metastable. On the other hand, for larger aspect ratio cylinders $m = 2.5, 5$, both models predict that the side-on state

is the ground state, and the end-on state is metastable. In Figure 5-2(i), we plot the energy barrier stabilising the end-on state against the side-on state as a function of aspect ratio calculated using the deformed interface model. We see that the energy barrier decreases with increasing aspect ratio and indeed disappears altogether for $m = 9.5$ (Figure 5-2(h)) so that only the side-on state is stable for $m \geq 9.5$. Finally, we note that a hydrophilic cylinder whose contact angle is the same distance away from the neutrally wetting condition (i.e., $\theta_w = 60°$ in this case) would have exactly the same orientational energy landscape as shown in Figure 5-2(e)-(h) except for the fact that the stable states of the cylinder would now be mainly immersed in the water phase, i.e., $h < 0$.

The end on state is meta-stable for non-neutrally wetting particles while the adsorbtion energy decreases for non-wetting particles as is evidenced in Figure 5-2. An implication here is that given a slight deviation from the globally stable state, say from transient contact line pinning site, there is a larger thermodynamic driver toward equilibrium for the non-neutrally wetting system than for the non-wetting system for equivilent parameters. For example, if we inspect Figure 5-2 tiles(b) & (f) and imagine both systems are transiently pinned at $\phi = 45°$ then the energy difference relative to the ground state is aprroximately $2\gamma b^2$ for the wetting particle and $4\gamma b^2$ in the non-wetting case.

5.3.2 Adsorption Kinetics of Cylinders at a Bare Liquid Interface

For convenience, we represent the adsorption trajectories of the cylindrical system using phase plane diagrams.[21,84,165] This is illustrated in Figure 5-3(a) where we show the adsorption trajectories for a hydrophobic cylinder with aspect ratio $m = 2.5$ for model 3 (deformed interface + Scaling 2) in the h vs. ϕ plane for $h \in$

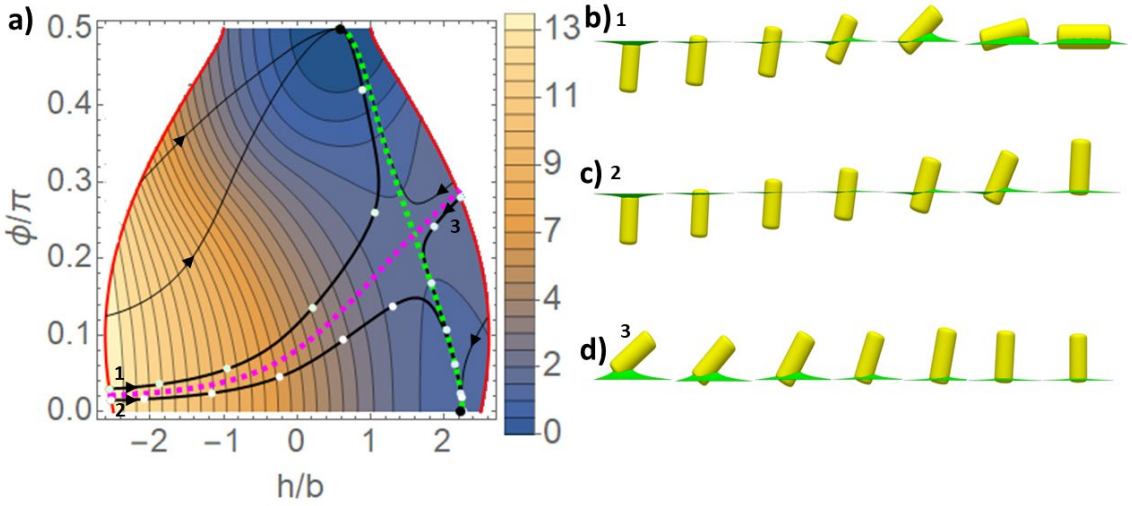

Figure 5-3 (a) Adsorption trajectories for a cylindrical nanorod with $\theta_w = 120°$, $m = 2.5$, $\eta = 20$ calculated from model 3 (i.e., deformed interface + Scaling 2) in the h vs. ϕ phase plane. The solid red curves represent the height of the cylinder when it first contacts the liquid interface as a function of particle orientation $h_c(\phi)$. The black dots represent the stable states of the cylinder, the solid black curves are the adsorption trajectories, the dashed green curve is the dynamical attractor and the purple dashed line is the separatrix. The trajectories are superposed on contour plots of the free energy landscape. To help visualize what the adsorption trajectories mean physically, in (b) – (d) we show snapshots of the cylinder at different stages of the adsorption process along the three trajectories highlighted in (a).

$[-h_c(\phi), h_c(\phi)]$ and $\phi \in [0, \pi/2]$. The solid red curves represent the height of the cylinder when it first contacts the liquid interface as a function of particle orientation $h_c(\phi)$, with the left and right curve representing contact from the water and oil side respectively. The two black dots represent the stable states of the cylinder calculated in the previous section, with the dots at $\phi = 0°, 90°$ representing the end-on and side-on states respectively. The solid black curves are parametric plots of the adsorption trajectories of the cylinder $(h(t), \phi(t))$, with all trajectories starting from the contact curves and flowing towards one of the two stable states as indicated by the arrows. To help visualize what these trajectories mean physically, in Figure 5-3(a) we have highlighted three trajectories in bold and show snapshots of the cylinder at different stages of the adsorption process along these trajectories in Figure 5-3(b)-(d). The dashed green line represents the 'dynamical attractor' to which many adsorption trajectories

are attracted at the later stages of the adsorption process. Figure 5-3(a) shows us that the range of faverable angles resulting in the end on state depends on the starting phase of adsorbtion. There is no reason why the faverable angle range should be the same for both phases outside of the neutrally wetting regime as we know that the molecular interactions between say, a hydrophobic particle and oil, are different from the same hydrophobic particle and water.

All the features in the phase plane that have been discussed so far also appear for adsorbing ellipsoids.[165] However, as non-neutrally wetting cylinders possess two stable states rather than just one, a new feature emerges called the 'separatrix' which is given by the dashed pink line. The separatrix divides the phase plane into two attractive regions such that all flow lines originating from points in a given region will flow towards the stable point associated with that region, see Figure 5-3. Recall that the main aim of this chapter is to use adsorption kinetics to prepare cylinders in the end-on state. We are therefore particularly interested in where the separatrix intersects the two contact lines. These intersections are the boundary attack angles ϕ_0 which tell us the range of particle attack angles which will lead to the end-on state.

In principle, the attractor and the separatrix lines are defined as the locus of points in (h, ϕ) space where the eigenvectors of the Hessian matrix $\boldsymbol{\nabla}\boldsymbol{\nabla}^T F^*$ with positive and negative eigen values respectively (i.e., with positive and negative principle curvatures respectively) are parallel to the gradient of the free energy $\boldsymbol{\nabla} F^*$, where $\boldsymbol{\nabla} = \left(\frac{\partial}{\partial h^*}, \frac{\partial}{\partial \phi^*}\right)$ is the grad operator in (h^*, ϕ^*) space.[21,84] However, since calculating second derivatives is very noisy numerically, we instead calculate these lines by calculating the adsorption trajectories for multiple attack angles in order to identify the boundary attack angles at each of the two contact lines. The trajectories starting from attack angles just above and just

below these boundary angles will then essentially trace out the separatrix and attractor lines.

From section 5.3.1, we saw that only non-neutrally wetting cylinders can exist in the end-on state that we are targeting in this study. Therefore the focus of this chapter will be on the adsorption trajectories of non-neutrally wetting cylinders. However, for completeness the adsorption of neutrally wetting cylinders is discussed in the following. In Figure 5-4, we present the adsorption trajectories for neutrally wetting cylinders ($\theta_w = 90°$) with different aspect ratios calculated using different assumptions. Specifically, the top, middle and bottom row show results for aspect

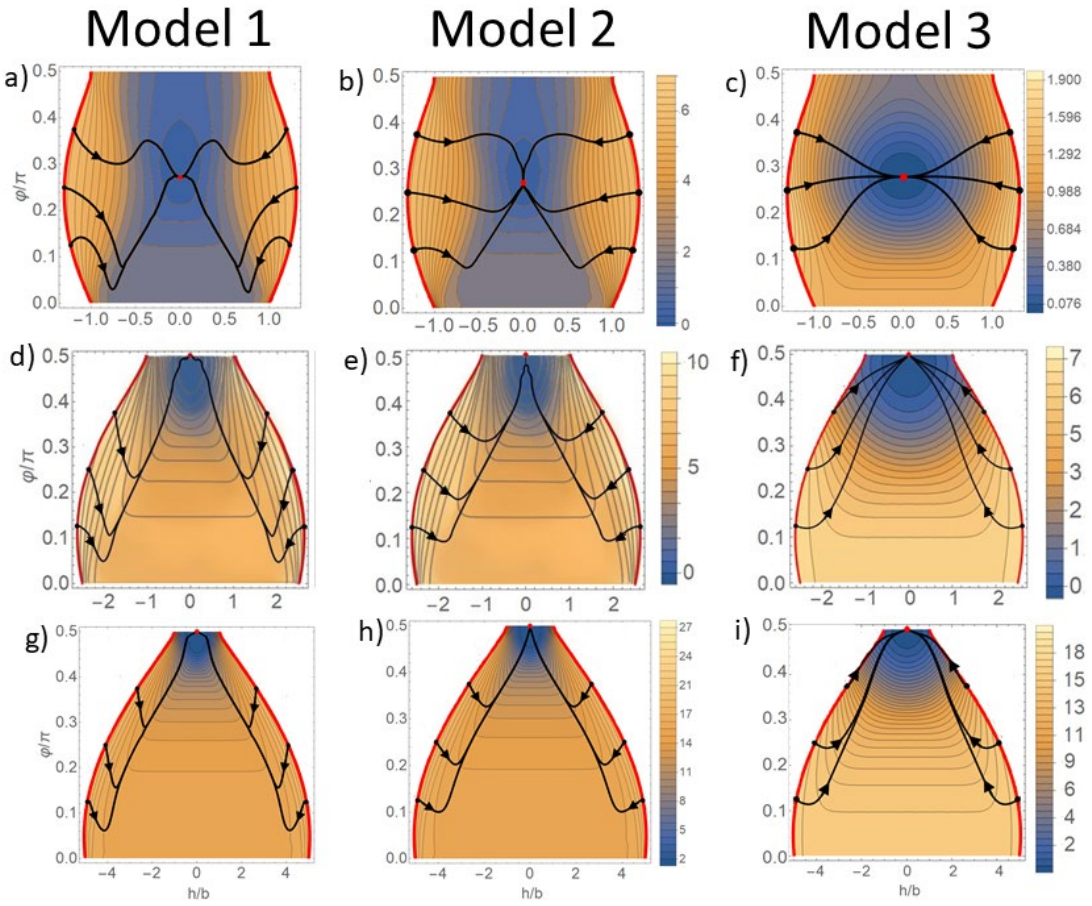

Figure 5-4 Adsorption trajectories of cylindrical nanorods with $\theta_w = 90°$, $\eta = 20$ for aspect ratio $m = 1$ (top row), $m = 2.5$ (middle row), $m = 5$ (bottom row) calculated from model 1 (left column), model 2 (middle column) and model 3 (right column). The solid red curves are the height of the cylinder when it first contacts the liquid interface as a function of particle orientation $h_c(\phi)$, the red dots are the stable states of the nanorod and the solid black curves are the adsorption trajectories. The trajectories are superposed on contour plots of the free energy landscape.

ratios $m = 1, 2.5$ and 5 respectively. On the other hand, the left, middle and right columns show the results for model 1 (flat interface + Scaling 1), model 2 (flat interface + Scaling 2) and model 3 (deformed interface + Scaling 2). For $m = 2.5$ and 5, the equilibrium state is the side-on state $\phi = \pm 90°$ while for $m = 1$, the equilibrium state is the tilted state, with a tilt angle $\phi = \pm 49.6°$ for the deformed interface model. These stable states are represented by the red dots in Figure 5-4. Since there is only one stable state in each case, the phase plane diagram for neutrally wetting cylinders dose not possess a separatrix.

We next consider the impact of the calculational model used on the adsorption process of cylinders. For all the aspect ratios shown in Figure 5-4, we see that for model 1, there is generally strong non-monotonic variation of the particle orientation ϕ along the adsorption trajectory, with ϕ initially moving away from the stable state orientation before moving towards the stable state value at the later stages of the adsorption. However, as we go to model 2 then to model 3, the non-monotonic variation of ϕ is either strongly reduced or disappears altogether. Finally, we note that for neutrally wetting cylinders with $m = 2.5$ & $m = 5$ the adsorption trajectories of particles approaching the liquid interface from the oil side do not converge onto the same dynamical attractors as particles approaching from the water side. Indeed, dynamical attractors are absent altogether for neutrally wetting cylinders where $m = 1$. Note that the absence of dynamical attractors for neutrally wetting particles is consistent with what we observed for the adsorption of ellipsoids at liquid interfaces in the previous chapter.

We now turn our attention to hydrophobic particles with contact angle $\theta_w = 120°$, but as we shall see later, our results can be readily generalized to hydrophilic

particles. We consider the idealized case of a cylinder with a relatively sharp edges (sharpness parameter $\eta = 20$) adsorbing at a bare liquid interface. In the next section, we will extend this simple model to include experimentally relevant factors such as the rounding of the cylinder edge and interactions with other nanorods for nanorods adsorbing at an interface with pre-adsorbed nanorods.

In Figure 5-5, we present the adsorption trajectories for hydrophobic cylinders with different aspect ratios calculated using several different assumptions. Specifically, the top, middle and bottom row show results for aspect

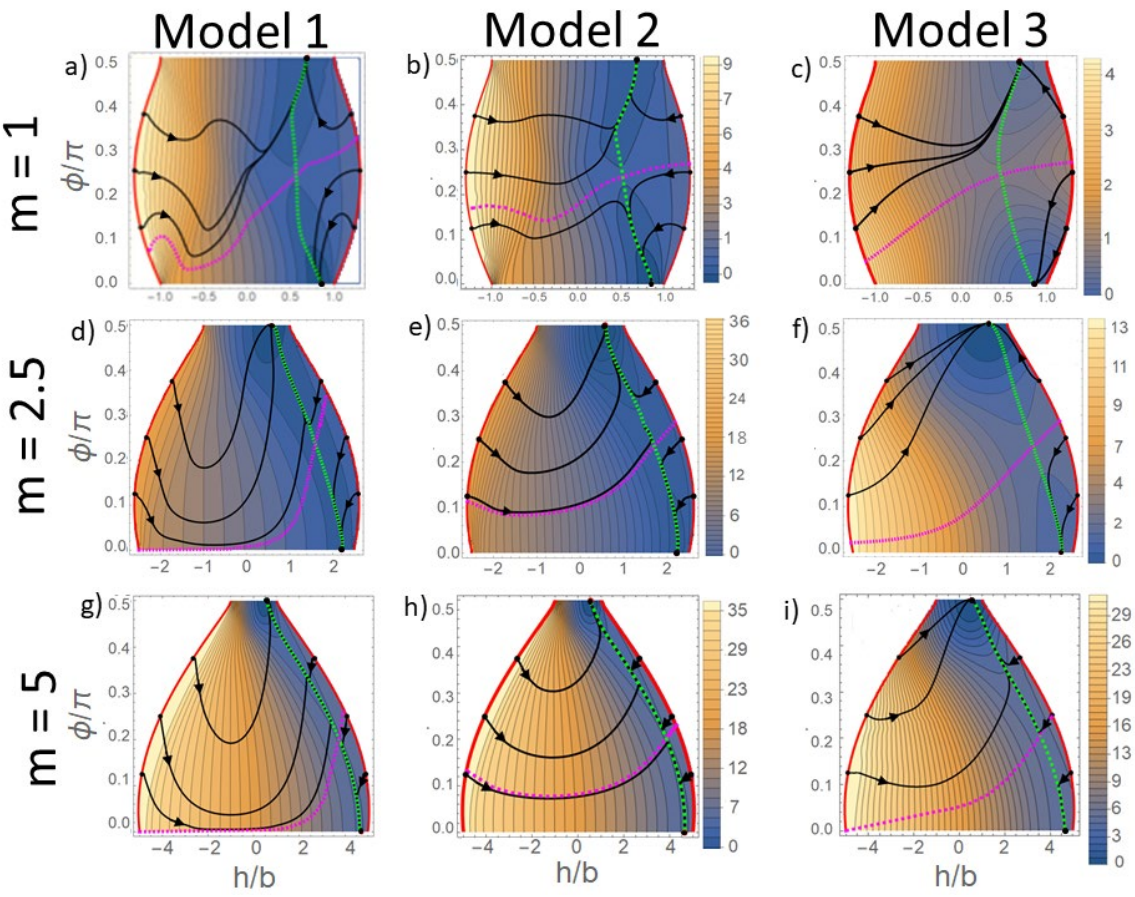

Figure 5-5 Adsorption trajectories of cylindrical nanorods with $\theta_w = 120°$, $\eta = 20$ for aspect ratio $m = 1$ (*top row*), $m = 2.5$ (*middle row*), $m = 5$ (*bottom row*) calculated from model 1 (*left column*), model 2 (*middle column*) and model 3 (*right column*). The solid red curves are the height of the cylinder when it first contacts the liquid interface as a function of particle orientation $h_c(\phi)$, the black dots are the stable states of the nanorod, the solid black curves are the adsorption trajectories, the dashed green curves are the dynamical attractor and the purple dashed lines are the separatrices. The trajectories are superposed on contour plots of the free energy landscape.

ratios $m = 1, 2.5$ and 5 respectively. On the other hand, the left, middle and right columns show the results for model 1 (flat interface + Scaling 1), model 2 (flat interface + Scaling 2) and model 3 (deformed interface + Scaling 2) respectively. For all the aspect ratios shown in Figure 5-5, we see that for model 1, there is generally strong non-monotonic variation of the particle orientation ϕ along the adsorption trajectory, with ϕ initially moving away from the stable state orientation before moving towards the stable state value at the later stages of the adsorption. However, as we go to model 2 then to model 3, the non-monotonic variation of ϕ is either strongly reduced or disappears altogether. This trend was also seen in our earlier study of ellipsoids where we found that the non-monotonic variation in ϕ was strongly suppressed in going from model 1 to model 3.[84] We also note that model 3 agrees best with experiments on ellipsoid adsorption which found that particle orientation varied monotonically with time during the adsorption process.[43,44]

Interestingly, for the aspect ratios shown in Figure 5-5, all three models showed very similar dynamic attractor lines. This result is again consistent with our earlier results for ellipsoids where we found that, far from the neutrally wetting regime, the attractor line becomes essentially insensitive to the assumed dynamic scaling model or contact line boundary condition.[84] In contrast, the specific calculational model used has a strong impact on the shape of the separatrix line. Specifically, in going from model 1 to model 2, the boundary attack angle on the left contact line (i.e., particle attaching from water side) is significantly increased, while in going from model 2 to model 3, that boundary angle is significantly decreased again. On the other hand, there is very little change in the boundary attack angle on the right contact line (i.e., particle

attaching from the oil side) in going from model 1 to model 2 to model 3. The net result is that when we change *both* the dynamical scaling model from Scaling 1 to Scaling 2 *and* the contact line boundary condition from flat to deformed interface, there is little change in the left and right boundary attack angles, suggesting that there is a cancellation of errors between these two model assumptions.

We next consider the impact of particle aspect ratio on the adsorption process of cylinders. Since we have shown previously in chapter four that model 3 yields the most accurate results, we will focus on model 3 for this discussion (i.e., right column of Figure 5-5). From Figure 5-5, we note that for all aspect ratios, the left boundary attack angle is always smaller than the right boundary attack angle. Furthermore, as we increase the aspect ratio from $m = 1$ to $m = 5$, the left boundary attack angle is reduced from $\phi_0 \approx 10°$ at $m = 1$ to $\phi_0 \approx 0°$ for $m = 5$. In contrast there is very little change in the right boundary attack angle, with the attack remaining essentially constant at $\phi_0 \approx 50°$ as we increase the aspect ratio from $m = 1$ to $m = 5$. Finally, we note that although our discussion so far has focussed on hydrophobic cylinders, all our conclusions also apply to hydrophilic cylinders so long as we recognise that the phase plane diagrams in this case should be reflected about the $h = 0$ line. In particular, this means that in order to maximize the range of attack angles leading to the end-on state, hydrophilic cylinders should be adsorbed onto the liquid interface from the water side.

Based on our discussion above, we conclude that the optimum condition for preparing cylindrical nanorods in the end-on state is to adsorb the nanorods from their energetically favorable phase, i.e., hydrophobic particles should be dispersed in the oil phase and hydrophilic particles in the water phase. Surprisingly, when particles

adsorb from the energetically favorable phase, the range of attack angles giving rise to the end-on state is only weakly dependent on the aspect ratio of the cylinders. This means that it should be possible to use the kinetic assembly method to prepare vertically aligned cylindrical nanorods with different aspect ratios, giving us the flexibility to tune the aspect ratio for different application (e.g., tune plasmonic modes for sensing applications). The caveat is that, while the aspect ratio may not be limited by adsorption kinetics, the end-on state becomes kinetically unstable when the aspect ratio of the cylinders $m \geq 10$. This effect sets the main limiting factor for the cylinder aspect ratios that can be assembled using our kinetic method.

5.3.3 Adsorption Kinetics of Experimentally Realistic Nanorods

In the previous section we considered the adsorption of cylinders with sharp edges at a bare liquid interface. In real experimental systems, the nanorods generally have more rounded edges and adsorption often occurs at a crowded monolayer where interactions with other pre-adsorbed nanorods could be important. In this section, we study the impact of these factors on nanorod adsorption.

We first consider the effect of edge rounding. In Figure 5-6(a), we show a transmission electron micrograph of a GNR from ref.[11] with diameter $48nm$, length $120nm$ and aspect ratio $m = 2.5$. We also superpose on the micrograph outlines calculated from the super-ellipsoid Equation 5-3 for the same aspect ratio and various sharpness parameter values η. From Figure 5-6(a), we see that the edges of the GNR are

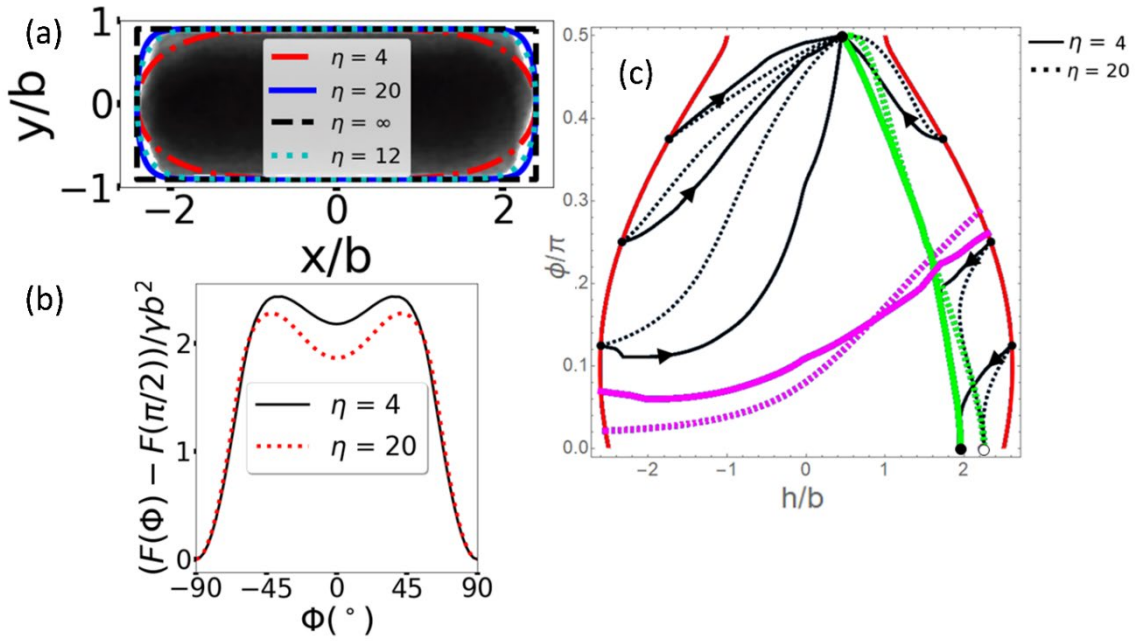

Figure 5-6 (a) Transmission electron micrograph image(reproduced from [11]) of experimental GNR with aspect ratio m=2.5 from ref.11 together with outlines calculated from the super-ellipsoid equation Eq.5-3 for the same aspect ratio and various sharpness parameter values η. (b) interfacial energy as a function of tilt angle ϕ for cylindrical nanorods with aspect ratio $m = 2.5$, contact angle $\theta_w = 120°$ and sharpness parameter $\eta = 4$ (solid black line) or $\eta = 20$ (dashed red line), where the interfacial energy at each ϕ is minimised with respect to the particle height h. (c) Adsorption trajectories of nanorods with $m = 2.5$, $\theta_w = 120°$ and $\eta = 4$ (solid lines) or $\eta = 20$ (dashed lines). The black and open dots represent the stable states for $\eta = 4$ and 20 respectively, while the black, green and purple lines are respectively the adsorption trajectories, dynamic attractor and separatrix.

more rounded than $\eta = 20$. Although it is difficult to assign a unique η value to the GNR because it does not fully conform to the super-ellipsoid shape (indeed there is evident faceting of the GNR ends in this system), we can see that the GNR has an effective sharpness parameter lying between $4 \leq \eta \leq 12$. In what follows we set $\eta = 4$ to give us an upper bound estimate for the influence of edge rounding on the adsorption trajectory of cylindrical nanorods and we compare these results to the case $\eta = 20$ that we considered in the previous section.

In Figure 5-6(b), we show the interfacial energy as a function of tilt angle ϕ for cylindrical nanorods with aspect ratio $m = 2.5$, contact angle $\theta_w = 120°$ and sharpness parameter $\eta = 4$ (solid black line) and $\eta = 20$ (dashed black line) where the interfacial energy at each ϕ is once again minimised with respect to the particle height h. Surprisingly, even though the edge is strongly rounded for $\eta = 4$ (see Figure 5-6(a)), the end-on state is still a metastable state. In addition, although edge rounding clearly reduces the energy barrier stabilising the end-on state, the barrier for $\eta = 4$ is still significant. For example, for a nanorod system with $\eta = 4$, $m = 2.5$, $\theta_w = 120°$, $\gamma_{ow} \approx 30$ mN/m and $b = 25$ nm, the energy barrier is $\Delta F \approx 1000kT$ so that the end-on state is still kinetically stable. Evidently even for $\eta = 4$, the nanorod end is sufficiently flattened to stabilize the endo-on state. In contrast, the end-on state is unstable for ellipsoids due to the absence of a flattened end.[21,22,84]

In Figure 5-6(c), we show the phase plane diagram for the adsorption of nanorods with $m = 2.5$, $\theta_w = 120°$ and $\eta = 4$ (solid lines) or $\eta = 20$ (dashed lines). The black and open dots represent the stable states for $\eta = 4$ and 20 respectively and we see that increasing the rounding of the edges reduces the heights of both the side-on stable state (dots at $\phi = \pi/2$) and end-on stable state (dots at $\phi = 0$). This reduction is not surprising since when the edges are rounded, the hydrophobic nanorod

can satisfy the constant contact angle condition by being immersed in the lower water phase more (see Figure 5-6(a)). We also see that changing the rounding of the edges leads to discernable changes in the adsorption trajectories (black lines), dynamic attractor (green lines) and separatrix (pink lines). In particular, the range of attack angles leading to the end-on state is slightly decreased and increased respectively for particles approaching from the oil side and the water side. However, the changes in Figure 5-6(c) are relatively small and none of the key features in in the phase plane diagram are changed qualitatively when we decrease η. We therefore conclude that the adsorption process is not significantly affected by edge-rounding and the sharp cylinders we have considered in the previous section therefore provide a good description for the adsorption kinetics of nanorods with experimentally realistic rounding.

5.3.4 Adsorption Kinetics of Cylindrical Nanorods at a Populated Interface

We now consider the effect of interactions with pre-adsorbed nanorods on the adsorption kinetics. In principle, we can calculate this effect by including many pre-adsorbed nanorods in our simulation and doing an ensemble average over the configurations of these nanorods. However, since such a calculation is too expensive in Surface Evolver, we instead use a simplified model to mimic the effect of the other nanorods. Specifically, as shown in Figure 5-7(a), we assume that the x, y-coordinate of the centre of the adsorbing nanorod (colored in green) is in the center of a hexagonal lattice with lattice constant S while the pre-adsorbed nanorods (coloured in yellow), assumed to be in the end-on state, are represented by the nearest and next-nearest neighbors in the hexagonal lattice. For definiteness, we further assume that the projection of the long axis of the adsorbing particle on the x, y-plane is parallel to one

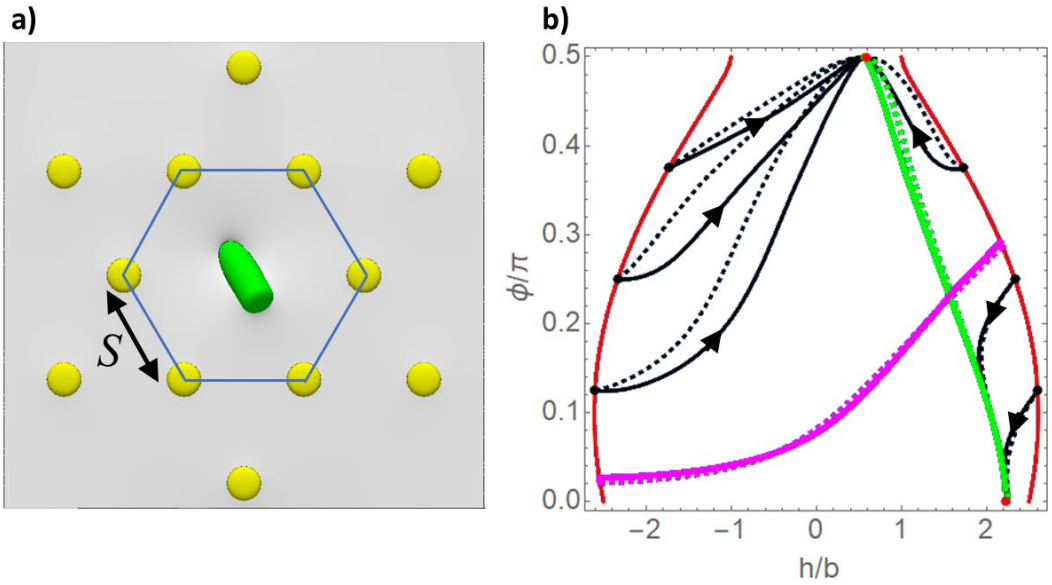

Figure 5-7 (a) Top view of simplified model used to study the adsorption kinetics of a nanorod at a monolayer with pre-adsorbed nanorods. The adsorbing nanorod (colored in green) is in the center of a hexagonal lattice with lattice constant S while the pre-adsorbed nanorods (coloured in yellow), assumed to be in the end-on state, are represented by the nearest and next-nearest neighbors in the hexagonal lattice. (b) Adsorption trajectories of nanorods with $\mathrm{m} = 2.5$, $\theta_w = 120°$ and $\eta = 20$ for a monolayer with $\mathrm{S} = 3\mathrm{a}$ (solid lines) or for a bare interface (dashed lines). The stable states for the monolayer and the bare interface are represented by the red and green dots respectively, but only the red dots are visible as the stable states in both cases are essentially the same. The black, green and purple lines are respectively the adsorption trajectories, dynamic attractor and separatrix.

of the lattice vectors of the hexagonal lattice and consider a moderately dense monolayer with $S = 3a$. We remark here that our goal in this highly simplified ensemble model is to probe what the effect of pre-absorbed, equilibrated particles may have on particles in the process of adsorbing. As such we are constrained by the chosen methodology to make a choice as to the specific configuration of the preabsorbed particles. Should we have chosen even a single cylinder in its globally stable state, along with its quadrupolar deformation, its in plane orientation would also need to be decided upon and the associated effects on its neighbors. We hope it is clear that this situation would rapidly result in an exponential increase in the degrees of freedom for the simulations which the model is not suited to study due to the computational cost such

a change introduces. We justify such a choice firstly, as our stated goal is to build a simplistic model which captures the salient physics of the system in order to reproduce such nanorod forests. Secondly, we only hope to parameterize boundary conditions for experiments to try to achieve such states. A deeper analysis would be far more suited to alternate simulation methods such as Monte Carlo simulations or lattice Boltzmann studies. Finally, we note that the open lattice shown in Figure 5-7(a) is not the final equilibrium state of the system but represents a transient arrangement of the rods during the adsorption process.

In the following, we estimate the range of dispersion forces for gold nanorods (GNRs) adsorbed at or approaching an oil/water interface in order to verify they can be safely neglected for interparticle distances under consideration. For vertical hydrophilic nanorods with length $L = 2a$, radius b which are attached to the oil/water interface and primarily immersed in the water phase, the dispersion interaction energy between two nanorods with surface-to-surface separation d through the water phase is given by[166]

$$U(d) = -\frac{A_{AuWAu} L b^{1/2}}{24 d^{3/2}} \qquad \textbf{(5-6)}$$

where A_{AuWAu} is the Hamaker constant for gold interacting with gold through water. By setting the interaction energy in Equation 5-6 to the thermal energy kT and rearranging, we find that the critical distance between two GNRs below which dispersion forces become significant is

$$d_{c1} = \left(\frac{A_{AuWAu} L b^{1/2}}{24 kT}\right)^{2/3} \qquad \textbf{(5-7)}$$

For $L = 120$ nm, $b = 25$ nm and $A_{AuWAu} = 4 \times 10^{-20}$ J[166] we find $d_{c1} \approx 200$ nm. We estimate that the dispersion forces between the GNRs only become significant for nanorod separation $\lesssim 200$ nm. Dispersion forces therefore do not play a significant role

in the initial and intermediate stages of the adsorption process when the typical separation between nanorods is much greater than this value.

For a hydrophilic GNR approaching the oil/water interface from the water side, if we approximate the nanorod tip closest to the interface as a sphere of radius b, the dispersion interaction energy between the nanorod and the oil phase with surface-to-surface separation d is[166]

$$U(d) = -\frac{A_{AuWO}b}{6d} \quad \textbf{(5-8)}$$

where A_{AuWO} is the Hamaker constant for gold interacting with oil through water which can be calculated from $A_{AuWO} = \sqrt{A_{AuWAu}A_{OWO}}$ where A_{OWO} is the Hamaker constant for oil interacting with oil through water.[166] Setting the interaction energy in Equation 5-8 to the thermal energy, we find the critical distance between the GNR and the interface below which dispersion forces become important to be

$$d_{c2} = \frac{A_{AuWO}b}{6kT}. \quad \textbf{(5-9)}$$

For $A_{OWO} = 0.5 \times 10^{-20}$ J[166] and $b = 25$ nm we find $d_{c2} \approx 40$ nm. Similarly, for a hydrophilic GNR approaching the oil-water interface from the water side, we estimate that the dispersion force between the GNR and the oil phase is significant only for surface-to-surface separations $\lesssim 40$ nm. Dispersion forces therefore only attract the GNR towards the interface when the GNR is quite close to the interface. They are also sub-dominant compared capillary forces once the nanorods have adsorbed onto the interface[158] and therefore do not play a significant role in determining the adsorption trajectory of the nanorods. However, dispersion forces will play a significant role in the final stages of the adsorption process as the final equilibrium separation is determined by balancing the attractive dispersion forces and repulsive forces (e.g., steric forces due to polymeric coatings) between nanorods. Finally, we note that since the energy barrier

stabilizing the end-on state of typical nanorods is much greater than the thermal energy as discussed earlier, we anticipate that the effect of orientational fluctuations of the neighboring nanorods on our calculations will be small.

In Figure 5-7(b), we show the phase plane diagram for particle adsorption at the monolayer described above (solid lines) and at a bare liquid interface (dashed lines). The stable states for the monolayer and the bare interface cases are represented by the red and green dots respectively but note that only the red dots are visible as the stable states in both cases are either very close or the same. The fact that the end-on state is the same for both monolayers and bare interfaces is as we expect since nanorods in the end-on state do not generate any interfacial deformations and hence no capillary interactions between the adsorbed and pre-adsorbed rods. We also see that interactions with pre-adsorbed nanorods lead to discernable changes in the adsorption trajectories (black lines) but hardly any changes to the dynamic attractor (green lines) and separatrix (pink lines). In particular, the range of attack angles leading to the end-on state is essentially unchanged for particles approaching from either the oil side or the water side, and none of the key features in in the phase plane diagram are changed qualitatively for nanorod adsorption at a dense monolayer. From our analysis in this section, we therefore conclude that the adsorption of cylinders with sharp edges at a bare liquid interface serves as an accurate predictive model for particle adsorption in experimentally realistic nanorod systems.

5.4 Discussion

Based on our results in the previous section, we now discuss the feasibility of using adsorption kinetics to experimentally prepare vertically aligned cylindrical nanorods at the liquid interface. As we shall see later, it is easier to use an external electric field to

align metallic nanorods when they are in the more polar medium. In our following discussion, we therefore consider hydrophilic GNRs with long and short axis $a = 25\ nm$ and $b = 10\ nm$ respectively (i.e., $m = 2.5$) approaching the interface from the water side. Our earlier calculations showed that the final state of such GNRs is the end-on state for initial attack angles less than $\phi_0 \approx 50°$. We can visualise the initial orientation of the GNR as a point on a hemisphere with radius unity (hemisphere since the range of ϕ is $0° \leq \phi \leq 90°$). Since the initial orientation of these sub-micron particles is essentially random due to Brownian motion, the ensemble of initial GNR orientations can be represented by points which are uniformly distributed over the hemisphere. The fraction of particles contacting the interface that will end up in the end-on state f_0 is therefore the fraction of the hemisphere occupied by a spherical cap which subtends an angle of ϕ_0 at the centre of the hemisphere, i.e.,

$$f_0 = \frac{2\pi \int_0^{\phi_0} \sin\phi d\phi}{2\pi} = 1 - \cos\phi_0 \qquad \textbf{(5-10)}$$

For $\phi_0 = 50°$, this yields $f_0 = 0.36$. Although substantial, this fraction is too small to create high quality vertically aligned monolayers.

We can increase this fraction by pre-aligning the GNRs in the bulk phase with an external electric field that is perpendicular to the liquid interface (see Figure 5-8) so that more GNRs have attack angles less than ϕ_0 when they approach the interface. In the presence of such a field, the energy of a GNR as a function of its orientation is given by[130]

$$U(\phi) = -\frac{1}{2}\Delta\alpha(E\cos\phi)^2 \qquad \textbf{(5-11)}$$

where E is the electric field strength and $\Delta\alpha = \alpha_{\parallel} - \alpha_{\perp}$ is the difference in the polarizability of the GNR along the long and short axis. Equation 5-11 predicts that, as we would expect, the lowest energy state occurs when the GNR is parallel to the electric field. In order to estimate $\alpha_{\parallel}$, $\alpha_{\perp}$, we approximate the GNR is an ellipsoid, allowing us to

calculate the polarizabilities analytically.[167] This approximation is reasonable given the significant rounding of the GNRs edges in typical experimental systems (see Figure 5-6(a)). In this case we have[167]

$$\alpha_{\parallel} = \varepsilon_r \varepsilon_0 \frac{V}{n_{\parallel}} \quad \textbf{(5-12)}$$

$$\alpha_{\perp} = \varepsilon_r \varepsilon_0 \frac{V}{n_{\perp}} \quad \textbf{(5-13)}$$

where ε_r is the relative permittivity of the bulk phase, ε_0 is the permittivity of vacuum, $V = \frac{4}{3}\pi a b^2$is the volume of the ellipsoid, $n_{\parallel}$, $n_{\perp}$ are depolarizing factors along the long and short axis given by

$$n_{\parallel} = \frac{1-\epsilon^2}{2\epsilon^3}\left(\ln\frac{1+\epsilon}{1-\epsilon} - 2\epsilon\right) \quad \textbf{(5-14)}$$

$$n_{\perp} = \frac{1}{2}(1 - n_a) \quad \textbf{(5-15)}$$

and $\epsilon = \sqrt{1 - 1/m^2}$ is the eccentricity of the ellipsoid.

In the presence of an electric field, the fraction of GNRs with attack angles in the range ϕ to $\phi + d\phi$ is given by the Boltzmann factor

$$P(\phi)d\phi = Ae^{-U(\phi)/kT} 2\pi \sin\phi \, d\phi \quad \textbf{(5-16)}$$

where A is a normalisation constant given by the condition $\int_0^{\pi/2} P(\phi)d\phi = 1$ and $U(\phi)$ is given by Equation 5-11. The fraction of GNRs with attack angles less than ϕ_0 is therefore given by

$$f = \int_0^{\phi_0} P(\phi)d\phi \quad \textbf{(5-17)}$$

Substituting the above equations into Equation 5-17 and changing variables to $u = \cos\phi$, the fraction of GNRs contacting the interface that end up in the end-on state as a function of the applied electric field is therefore given by

$$f(\kappa) = \frac{\int_{u_0}^{1} e^{\kappa u^2} du}{\int_{0}^{1} e^{\kappa u^2} du} \quad \textbf{(5-18)}$$

where $u_0 = \cos\phi_0$ and

$$\kappa = \frac{\Delta\alpha E^2}{2kT} \quad \textbf{(5-19)}$$

In Figure 5-8, we plot f as a function of the effective field strength κ for $\phi_0 = 50°$. We see that f increases with increasing κ as we would expect, starting at $f = f_0$ at $\kappa = 0$ and saturating at $f = 1$ for large κ. Specifically, $f = 0.995$ for $\kappa = 10$. From Equation 5-21, since $\Delta\alpha \propto \varepsilon_r$, for a given electric field E we obtain stronger alignment of the nanorods in the more polar medium. This is why we have considered hydrophilic GNRs approaching the liquid interface from the water side in this section. Specifically, for $\kappa = 10$, $b = 25$ nm, $m = 2.5$, $\varepsilon_r = 80$ (permittivity of water) and $T = 300$ K, from Equation 5-21 we find $E \approx 10^4\ Vm^{-1}$, i.e., applying this field in the water phase allows us to achieve 99.5% vertical alignment for the final state of the adsorbed nanorods. This is a modest electric field which is orders of magnitude smaller than the dielectric strength of de-ionised water ($70 \times 10^6\ Vm^{-1}$)[168] and is easily achievable experimentally. Note that a common way to enhance the local electric field near a liquid-liquid interface is to add electrolytes to the two bulk phases and polarise the interface using an external

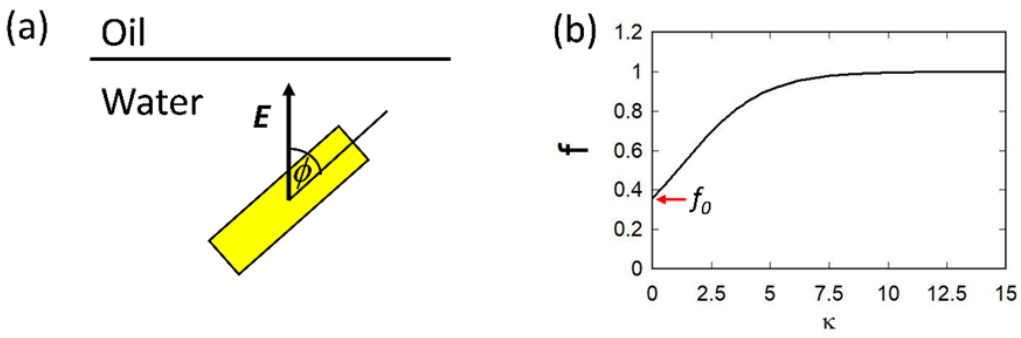

Figure 5-8 (a) Pre-alignment of GNR in the water phase using an electric field E prior to particle attachment to the liquid interface. (b) Fraction of GNRs with attack angle less than $\emptyset_0$ as a function of the effective electric field strength κ.

field.[169–171] Using this so-called interface between two immiscible electrolyte solutions (ITIES) arrangement would allow us to lower the external field required to pre-align the GNRs even further. We therefore conclude that it is feasible experimentally to use our kinetic assembly method to prepare high quality vertically aligned cylindrical nanorod monolayers at the liquid interface.

Finally, we note that applying an external electric field (either in the absence or presence of added electrolytes) will create polarization charges at the liquid interface which may significantly modify the interfacial tension of the liquid interface.[169–171] However, since interfacial tension only affects the timescale of the adsorption (via the scaling factor β, see Section 5.2.2) but not the adsorption trajectory itself (i.e., particle orientation vs. particle height), applying an external electric field across the liquid interface should not in principle affect the main result of our free energy calculation, namely the range of particle attack angles which will lead to the end-on state of GNRs.

5.5 Conclusion

We have used Langevin dynamics coupled to a finite element model to study the adsorption kinetics of cylindrical nanorods at an oil/water interface in order to determine the optimum conditions for using adsorption kinetics to assemble nanorods into vertically aligned monolayers. Our Langevin model is more accurate compared to previous models as it accurately captures the deformation of the liquid meniscus during particle adsorption and uses the correct ratio for the rotational to translational friction coefficients for the nanorod.

We find that the end-on state is stable only for non-neutrally wetting cylindrical nanorods. We also find that the final orientation of the nanorods at the oil/water interface is determined by their initial attack angle when they contact

the liquid interface. In particular, the range of attack angles leading to the end-on state is maximised when nanorods adsorb onto the liquid interface from the energetically favorable phase, i.e., hydrophobic particles from the oil phase and hydrophilic particles from the water phase. Surprisingly, we find that the range of attack angles is only weakly dependent on particle aspect ratio, thus allowing us to use adsorption kinetics to assemble vertically aligned nanorods for a wide range of aspect ratios. However, we also find that the energy barrier stabilizing the (metastable) end-on state decreases with increasing aspect ratio and/or decreasing radius of the cylinder. This effect sets a practical limit of $m \leq 10$ on the cylindrical nanorods that can be assembled into vertically aligned monolayers using our kinetic assembly method.

Since only attack angles smaller than a threshold value lead to the end-on state, in the absence of an external field, only a fraction of nanorods that contact the liquid interface end up in the end-on state (typically $\lesssim 40\%$ under optimum conditions). However, by pre-aligning the nanorods in the more polar bulk phase with experimentally achievable electric fields, we can increase this fraction to be effectively 100%. Our kinetic assembly method is generic and can be used to assemble nanorods with a range of diameters, aspect ratios and materials (e.g., gold, silver, aluminium, copper, polymer, silica etc.). As such, it represents a versatile, low-cost and powerful platform for fabricating vertically aligned monolayers of nanorods for metamaterial applications.

Chapter 6 Directing Self-Assembly Through Particle Geometry

6.1 Introduction

In this chapter we progress from the role particle morphology and interfacial deformation plays in the adsorption process and investigate how these factors affect the self-assembly of particles adsorbed at a liquid-liquid interface. Colloids exhibit a wide variety of attractive and repulsive interactions over a range of length scales. In the bulk these can take the form of electrostatic[29,30] or magnetostatic[172,173] interactions, steric forces[27,28] or excluded volume repulsions.[174] When adsorbed at an immiscible interface capillary interactions play a key role.[19,32,33] Through relatively minor modifications of colloidal properties, such as shape or wettability, it is possible to tune the capillary interactions and in turn direct their self-assembly.[35,42,159,175] With advancement of particle synthesis techniques[10,13,14,176] and stereolithography[177] it has become possible to control colloidal geometry at sub-micron scales with feature sizes on the nanoscale. When combined with immobilization and substrate transfer techniques[101,164] a powerful platform emerges for creating novel nanomaterials. Colloidal systems therefore not only serve as an ideal platform to study the general phenomenon of self-assembly, but also unlocks the possibility of artificially engineering metamaterials with unique optical, acoustic, thermal, electromagnetic and plasmonic properties.[29,30,172,173,178,179]

We briefly reiterate here the relevant principles with respect to the effect of particle morphology on meniscus deformation. We refer the reader to the theoretical background and literature survey presented in chapter two for more detail. Our goal, as we demonstrate later, is to study how particle shape affects self-assembly. Specifically, we design particle morphologies which favor certain configurations when interacting

due to the interplay of far and near-field meniscus deformations. The differentiation from the current body of literature is that these favored orientations originate solely from shape rather than surface chemistry.

The constant contact angle requirement at the three phase contact line can lead to large deformations of the meniscus surrounding adsorbed anisotropic particles and in turn, strong capillary interactions between them.[18,19,67] We refer the reader to Section 2.12 for a mathematical description and discussion of the meniscus shape along with the leading order modes. Briefly, consider a freely moving three phase contact line, the intersection of particle, liquid and vapor, able to traverse over a perfectly smooth and chemically homogenous particle. In order to satisfy Young's constant contact angle constraint, contact line undulations and interfacial deformation can arise from particle anisotropy.[19,20] Save for a few special cases, such as perfectly smooth spheres, the leading order term describing the interfacial deformation at equilibrium is the quadrupole.[64,65]

Adsorbed particles can interact when the deformations from nearby particles overlap. The range of such interactions is dependent on the leading order mode, with higher order modes decaying much faster. It costs energy to deform an interface, therefore overlapping deformations having the same signed curvature reduces the interfacial area which in tun reduces the free energy of the system, decreasing further as these regions approach.[65] The inverse is also true, overlapping opposite signs increases the free energy of the system and results in particle repulsion. It is well reported in the literature, colloidal systems aligning and aggregating but equilibrating in different configurations depending on the specific modal superposition.[34,36,39,180]

Yao *et al.*[181] demonstrated that not only is it possible to direct self-assembled structures through a suitable choice of particle morphology and wetting characteristics, but it is also possible to control near-field interactions by introducing small undulations to the particle geometry. Building on the work of Lucassen[176], the group used bent, corrugated sheet shaped particles and were able to tailor the equilibrium distance of approach of their particles by altering the amplitude and phase of the corrugations. The leading order mode of the meniscus was a quadrupole, originating from the bent sheet, providing the attractive force while the near field repulsion came from the corrugations therefore controlling the interplay of the attractive and repulsive forces entirely via particle shape.[176,181]

In an early experimental demonstration of directed self-assembly, Whiteside's *et al.* used millimeter scale hexagonal plates, which had a hexapolar meniscus, at an oil-water interface and changed the surface chemistry of the facets in various configurations.[103] Changing the surface chemistry altered the contact angle of specific facets which in turn changed the position of the three-phase contact line and therefore the interfacial deformation (see Section 2.3.5). Doing so allowed them to customize the modes of the meniscus deformation which altered the capillary interactions and ultimately the final self-assembled structures. Such an approach resulted in open and closed pack structures, linear chains, branched chains, dimers and tetramers depending on the specific choice of functionalized facets.[35,103] While an elegant experimental proof of concept, this approach becomes incredibly difficult to scale down due to the difficulties in particle synthesis of tightly controlling both geometry *and* specific facet surface chemistry.

The aim of this chapter is to build on and extend the work of Whiteside's by demonstrating that it is possible to direct colloidal self-assembly through particle shape alone. In a similar fashion we also use polygonal plates however, instead of using functionalized facets to control meniscus deformations we use undulating edges. The hexagonal shape in the $x-y$ plane controls the longer-range capillary interactions and the undulation in the z direction introduces higher order modes in order to precisely control the near-field capillary interactions. There are multiple advantages in taking this approach as opposed to using functionalized facets. Using plates results in a single stable orientation as opposed to multiple stable states when using cubic or cylindrical particles.[25,63] Secondly, the contact line is pinned to the undulating edge of the plate giving superior control over the meniscus shape when compared to ellipsoids, cylinders or cubes. This is because for 3D shapes the contact line is movable therefore it is not as straightforward to get a specific contact line undulation. Finally, due to significant advancements in 3D printing techniques it is possible to control particle shape with feature sizes on the nanoscale[182], and significantly easier than controlling the surface chemistry of specific particle facets down to micron or even nanoscale.

6.2 Theoretical Model

6.2.1 Geometry of Undulating Plates

In this section we present the mathematical model we use to define the platelets geometry within our simulations. We simulate five variants in this chapter but all can be described by a modified version of the super-ellipsoid equation.[117] Equation 6-1 enables us to represent a generic polygonal shape with rounded edges which can be customized by a suitable choice of coefficients.

$$\left(\frac{Ax''+By''}{a}\right)^{\eta_1}+\left(\frac{y''}{b}\right)^{\eta_2}+\left(\frac{Cx''-Dy''}{c}\right)^{\eta_3}+\left(\frac{(z''-z_0(\theta))}{d}\right)^{\eta_4}=1 \qquad \textbf{(6-1)}$$

In Equation 6-1 $x"$, $y"$ and $z"$ are the Cartesian coordinates having undergone two rotational transforms we illustrate shortly. The coefficients of x, y in the numerator of the first and third terms in Equation 6-1 are chosen such that $Ax + By = 1$ is a straight line of slope $\sqrt{3/2}$, 0 and $-\sqrt{3/2}$ respectively. This choice of coefficients describe the hexagonal plate shown in Figure 6-1(a). Finally, the denominators a, b, c control distance of these straight lines from the origin while d sets the thickness of the platelet.

A source of difficulty when using FEA to study interfacial systems is that when the three phase contact line passes over sharp edges the system becomes numerically unstable.[116] Equation 6-1 circumvents this issue because η_1, η_2, η_3 control the sharpness of the edges in the x, y plane and η_4 sets the curvature of the sides of the platelet in the x, z plane. Finally, within Equation 6-1 we use $z_0(\theta)$ to control the undulations of the plate such that

$$z_0(\theta) = A\, r_c \cos\big(3(\theta - \theta_0)\big) \qquad \textbf{(6-2)}$$

where θ_0 is an offset to phase shift the undulations and

$$r_c = \sqrt{x"^2 + y"^2} \qquad \textbf{(6-3)}$$

The hexagonal platelet illustrated in Figure 6-1, described by Equation 6-1, has denominators $a = b = c = 1$, and $d = 0.1$. In the figure, x, y, z correspond to lab frame co-ordinates with z perpendicular to the unperturbed liquid interface as illustrated. Applying two coordinate transforms, as detailed in Chapter 3, the first a tilt of θ_t about the x axis and second a rotation of θ_r about the z' axis, enables us to configure the particle in any desired orientation.

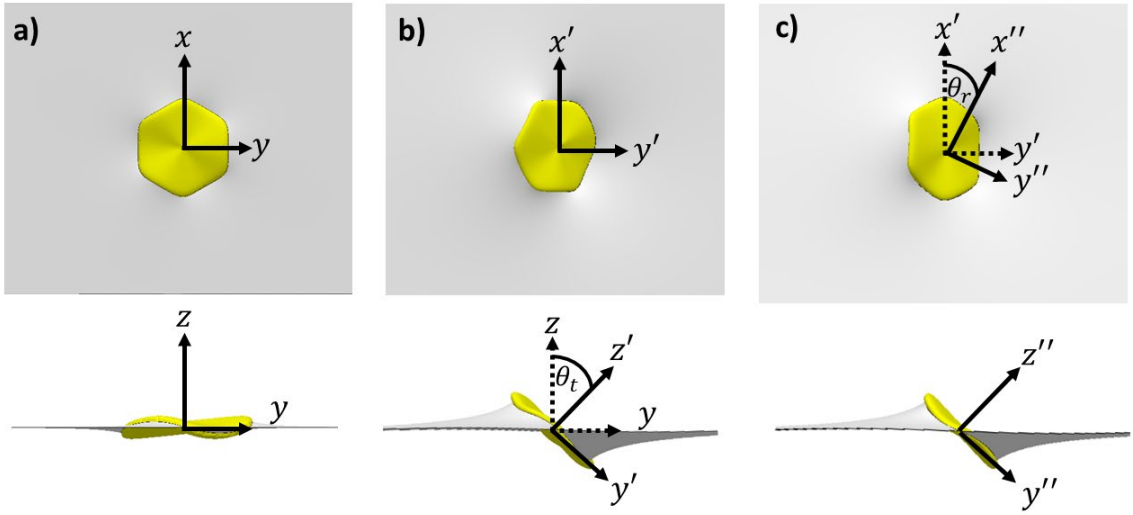

Figure 6-1 Definitions of rotational angle θ_r and tilt angle θ_t with respect to the particle centred at the origin. Top down (*top row*) and in plane (*bottom row)* views illustrating the lab from coordinates (a) followed by a tilt about the x axis of $\theta_t = 45°$ (b) then a rotation about the z' axis $\theta_t = 30°$ (c).

In order to study the interplay between short-range steric repulsion and long-range capillary interactions on self-assembly, we consider two different variations of the hexagonal plate Illustrated in Figure 6-1, which we refer to as Plate 1 and Plate 2. Plate 1 has sinusoidal undulations in z whose peaks correspond with the corners of the hexagon. Plate 2 on the other hand, has undulations phase shifted by $\pi/6$ such that the peaks of the undulations are at the center of the straight edges of the hexagonal plate. We finally consider three versions of a distorted Plate 2 which more closely resembles a truncated triangular platelet. For visual aids see Figures 6-4 & 6-11.

6.2.2 Thermodynamics

In the following we outline a similar theoretical treatment of the thermodynamic potentials of interacting particles akin to Soligno *et al.*[39,63,68] With no particle adsorbed an immiscible, fluid-fluid interface of area A is the flat plane $z = 0$. We introduce N rigid, smooth, uncharged particles of fixed positions and orientations which are specified by $\Omega = \{z_{ci}, \varphi_i, \psi_i, x_i, y_i, \alpha_i\}_{i=1}^{N}$. Here, z_{ci}, x_i, y_i refer to the Cartesian coordinates of the center of mass of the i^{th} particle and $\varphi_i, \psi_i, \alpha_i$ to its polar, internal Euler and azimuthal angles respectively. As we are considering particles between $10nm$ and $10\mu m$ we can

safely neglect gravity and line tension. The thermodynamic potential of this system is given by[183]

$$E_N(\Omega) = \gamma[S(\Omega) - A + W(\Omega)\cos\theta_w] \quad \textbf{(6-4)}$$

In Equation 6-4 $S(\Omega)$ is the total area of the interface with particles present and A the total area without, where γ is the fluid-fluid surface tension. The contact angle is denoted θ_w where $W(\Omega)$ is the total surface area of the particle(s) in contact with the fluid above the interface.

Considering a single, isolated particle E_1, the interface shape which minimizes Equation 6-5 will be the equilibrium shape of the fluid-fluid interface i.e., the solution of the Young-Laplace equation with Young's law as a boundary condition.[63,183] For N particle systems the capillary interaction energy per particle is defined as[63]

$$\tilde{E}_N \equiv \frac{E_N}{N} - E_1 \quad \textbf{(6-5)}$$

We use Equation 6-5 to study the dependance on particle-particle separation (S) for a selection of configurations of two approaching particles, $\tilde{E}_2$. We then progress to make the periodic extension ($N \to \infty$) and calculate $\tilde{E}_\infty$ for a lattice unit cell for honeycomb, hexagonal close packed, square and kagome lattice structures. Finally, we consider the interaction potential between two particles comparing our Surface Evolver results to a purely theoretical treatment of interacting multipoles of arbitrary order presented by Danov *et al.*[32] The specific details of this treatment are detailed in section 6.4.2 after we have presented results which clarify our specific choice of parameters.

6.2.3 Surface Evolver

All simulations are of neutrally wetting particles, i.e., $\theta_w = 90°$. We use Surface Evolver (SE) to simulate a large, $24r \times 24r$, square simulation box. The particle is centered at the origin and we allow the interface to move freely in the z direction in

order to fully equilibrate. This no different to allowing the particle center of mass to vary freely and, if the simulation cell is large enough, enforces a planar interface far from the particle.[25,48] The Boundary is effectively a Neumann boundary condition because we assume the simulation walls are neutrally wetting, having a contact angle of $\theta_w = 90°$ at the outer boundary.[20]

For a detailed discussion of the workings of Surface Evolver we refer to chapter 3 but briefly, SE tessellates a user defined surface and calculates the force on each vertex. Next it uses a gradient decent to move the vertex in this direction, iterating this process to find the lowest free energy permitted by a given configuration.[114] In the final stage of surface evolution, we change from a linear tessellation regime to a quadratic one in order to model the surface with greater precision. All dimensions are normalized to units of $r = 1$, which is the distance from the center to the vertex of a plate, with the underlying assumption that the results can be scaled within the size ranges outlined prior.

In the following we study the free energy landscape of an isolated plate then move on to pairwise interactions before finally investigating periodic systems for both Plates 1 and 2. Finally, in order to study the impact of changing the interplay between short-range steric repulsion and long-range capillary interactions on self-assembly, we consider a distorted version of the hexagonal plate in the same fashion.

6.3 Results

6.3.1 Isolated Hexagonal Plate

Before we try to tailor the interplay between the short and long-range capillary interactions by introducing symmetric undulations to our plate like geometries, it is first necessary to verify that introducing these small undulations doesn't affect the particles

equilibrium configurations. If this were the case, we would be potentially altering the leading order modes of the meniscus deformation. We verify that this is not the case by performing 1620 SE calculations of the free surface energy for particle orientations over the ranges $-90° \leq \theta_t \leq 90°$ and $0° \leq \theta_r \leq 90°$ in one degree increments. The free energy is then normalized such that $E_1 = E(\theta_t, \theta_r) - E(\theta_t = 0, \theta_r = 0)$ and the resulting energy landscape plotted in Figure 6-2.

The normalized free energy landscape illustrated in Figure 6-2 has three main features. Firstly, the main valley located along the line corresponding to $\theta_t = 0°$. When the plate is flat at the interface such that the tilt angle is zero, changing the rotation angle over the range $0° \leq \theta_r \leq 90°$ has no effect on the free energy of the system for the isolated plates because the states are all equivalent. In contrast a ripple in the free energy landscape is observed for $0° \leq \theta_r \leq 90°$, having the greatest amplitude at $\theta_t = \pm 90°$. In this configuration the hexagonal plate is perpendicular to the interfacial plane and the undulation in the landscape is consistent with the corners of the plate dipping

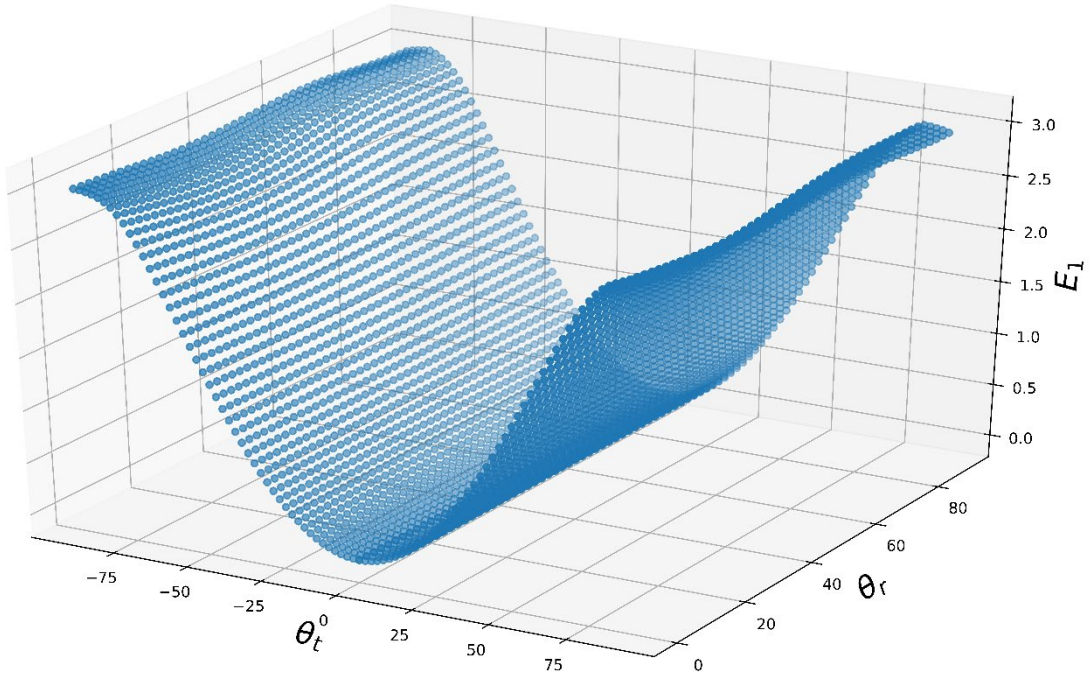

Figure 6-2 Normalised (see text) free energy landscape for Plate 1 as a function of tilt angle θ_t and rotation angle θ_r as defined in Figure 6-1.

in and out of the interface, repeating every sixty degrees of rotation and resulting in the small fluctuations as shown.

One final remark is that setting $\theta_r = 0°$ and tilting $0° \leq \theta_t \leq 90°$ increases the free energy as there is increasingly less interfacial area removed by the disk as it tilts from being parallel with the interface to perpendicular. Therefore, we conclude that the equilibrium configuration of plate like geometry with symmetric undulations is $\theta_t = 0°, \theta_r = 0°$, and that the introduction of the symmetric undulations does not change the equilibrium orientation of the plate.

It follows from the constant contact angle constraint that varying the magnitude of the undulations above some threshold could cause the meniscus to no longer be pinned at the particles edge. In such a case, the three-phase contact line may start to migrate underneath the particle, reducing the effectiveness of the undulations in controlling the meniscus shape. In Figure 6-3 we Illustrate a cross sectional slice in the x, z plane of several different undulation amplitudes A and how the interface meets

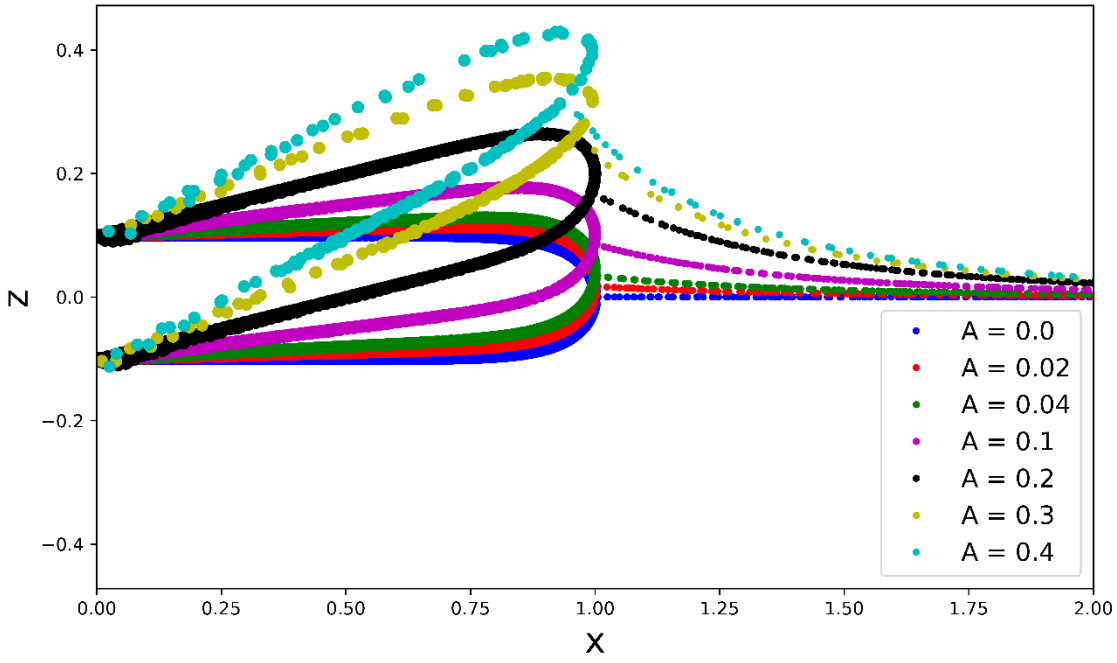

Figure 6-3 Cross section of a particle centred at the origin and the equilibrated interface for varying undulation amplitudes. Amplitudes expressed as multiples of r. As can be seen, larger amplitudes lead to the interface migrating below the tip of the particle.

them for a contact angle $\theta_w = 90°$. We express the amplitude of the undulations in terms of multiples of r and can see that in the limiting case $A = 0r$ (blue dots) both the plate and the interface are perfectly flat. As the amplitude steadily increases so does the height of the meniscus and at $A{\sim}0.4r$ (cyan dots) the interface starts to meet the particle on its underside. This migration of the three-phase contact line to the underside of the particle is problematic for our end goal as it means that the undulation of the liquid meniscus no longer faithfully follows the particle edge. Finally, as illustrated in Figure 6-3, larger undulation amplitudes result in large deformation amplitudes. However, it is desirable to keep the amplitude of deformations small so that deformation of the interface remains in the linear regime where linear superposition applies. Therefore, in the following we choose an undulation amplitude $A = 0.1r$. We note here that it would not be expected that the equilibrium configuration $\theta_t = \theta_r = 0°$ should change for larger amplitudes because of the symmetry of the particle. Any force introduced by increasing the amplitude for an undulating peak would be counter balanced on the opposing side by a corresponding but reversed force due to an undulation's trough. Finally, we reiterate that in order for the contact line to be pinned at the particle edge and faithfully reproduce the undulations in the meniscus we require a neutrally wetting particle, equilibrated with its surroundings and that the undulations amplitude be no larger than 10% of plate thickness.

In order to form honeycomb or kagome lattice structures using capillary interactions a leading order hexapole is desired. In Figure 6-4 we present contour plots of hexagonal Plate 1 (a) and Plate 2 (c) for visualization and define the circular coordinates R, θ. The peaks and troughs of the hexapole correspond to the corners of Plate 1 in (a) whereas they are phase shifted $\pi/6$ to the middle of the straight edges for Plate 2 (c), as shown in the contour plots. The relevance of this will become apparent in the following section when we study pairwise interactions. In Figure 6-4 (b, d) we extract the interfacial height of the meniscus, z, at fixed radii $R = 1.5r$ and $R = 5r$ from the particle center (solid black dots and solid blue line respectively) and fit a pure hexapole to it (solid magenta line) of the form $z(R, \theta) = 3 \sin 3\theta$ for Plate 2 and $z(R, \theta) = 3 \cos 3\theta$ for Plate 2. The contour plots (a) and (c) are cropped in size for visual clarity when in reality the simulation cell is significantly larger. It can be seen in both (b) and (d) that the hexapolar mode of the meniscus is essentially perfect at $R = 1.5r$, rapidly decaying at a distance of $R = 5r$ as would be expected from theory. Note that the small

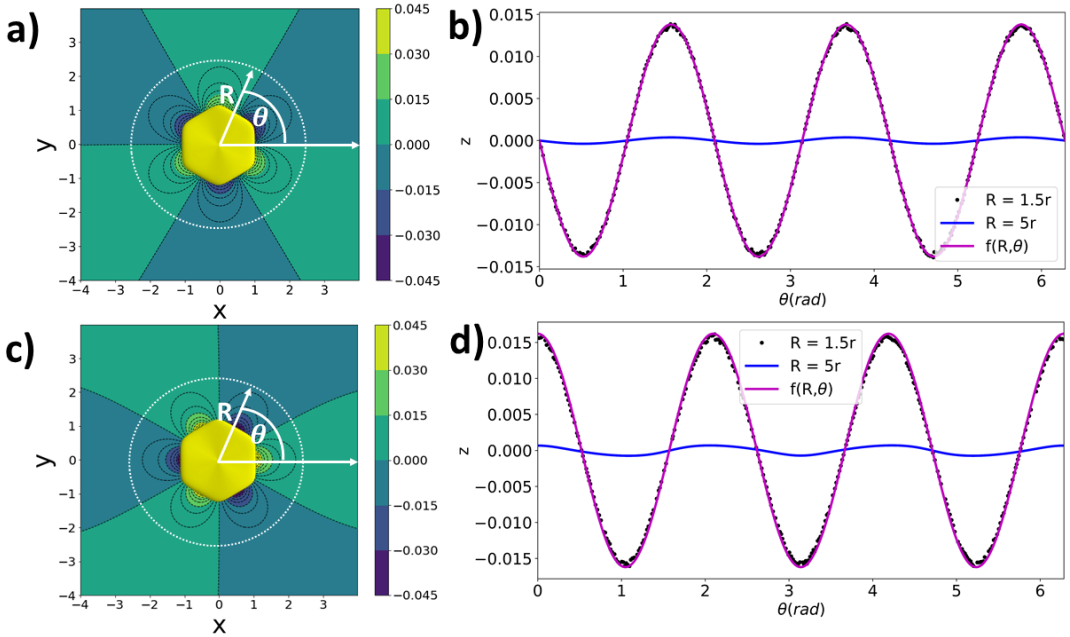

Figure 6-4 Contour plots of the meniscus deformation for Plate 1 (a) and Plate 2 (c) with the hexagonal plates superimposed on top, alongside the definitions of the circular coordinates R, θ. Right column, the meniscus height profiles as a function of θ at fixed R values for Plate 1 (b) and Plate 2 (d) are also shown with an ideal hexapolar fit (magenta lines). See text for Fitting details.

degree of noise in the black dots in tiles (b) and (d) is an artifact of the data extraction method as we need to extract vertices within a thin shell. Having considered the isolated case for both Plate variants we now progress to study the capillary interactions between two plates.

6.3.2 Pairwise Interactions Between Hexagonal Plates

To study the capillary interactions between two plates we firstly discuss some nomenclature and then study several relative orientations. As demonstrated in Section 6.3.1 the leading order mode of the meniscus is a hexapole. In Figure 6-5 we illustrate some of the relative orientations for two interacting plates with hexapolar interface deformations and, continuing from the contour plots in Figure 6-4, indicate a rise in the interface height profile with a green spot and a depression with a blue spot. The two plates have a center-to-center plate separation s, expressed in multiples of r. For succinctness we refer to interactions in which two spots overlap as “dipole-dipole” interactions (D-D), interactions where three spots overlap a “tripole-tripole” (T-T) and interactions in which two spots interact with three a “dipole-tripole”. We note that the

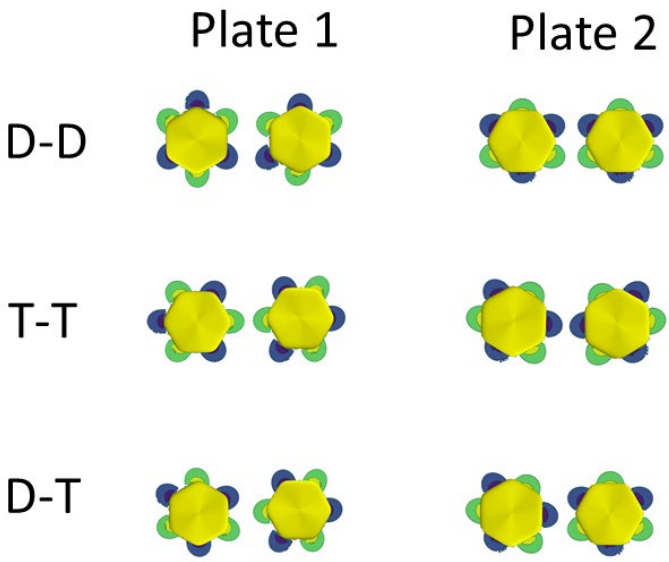

Figure 6-5 Illustrations of three different configurations of two interacting plates. A blue spot indicates an interfacial depression and a green spot indicates a rise with respect to the planar interface. We show the dipole-dipole (top row), tripole-tripole (middle row) and dipole-tripole (bottom row) for Plate 1 (left column) and Plate 2 (right column).

T-T configuration is attractive for both plates 1 & 2 but it is favorable for plate two because the orientation of the antinode of the contact line undulation means that the closest distance of approach between the two plates is achieved for the T-T interaction in this configuration.

Having illustrated some of the relative orientations for two interacting plates we now calculate the free energy as a function of center-to-center particle separation for Plates 1 & 2. Figure 6-6 shows the normalized free energy as a function of centre-to-centre expressed in terms of r for Plate 1 in attractive (a) and repulsive (b) configurations. The dashed lines indicate the contact distances for each configuration with red the tripole-tripole, blue the dipole-dipole and black the dipole-tripole. The free energy is normalised such that $\tilde{E}_2 = E(r = \infty) - E_2(r)$. As can be seen in the plots, the plates start to interact at $r \approx 2$ and the normalized free energy starts to drop off

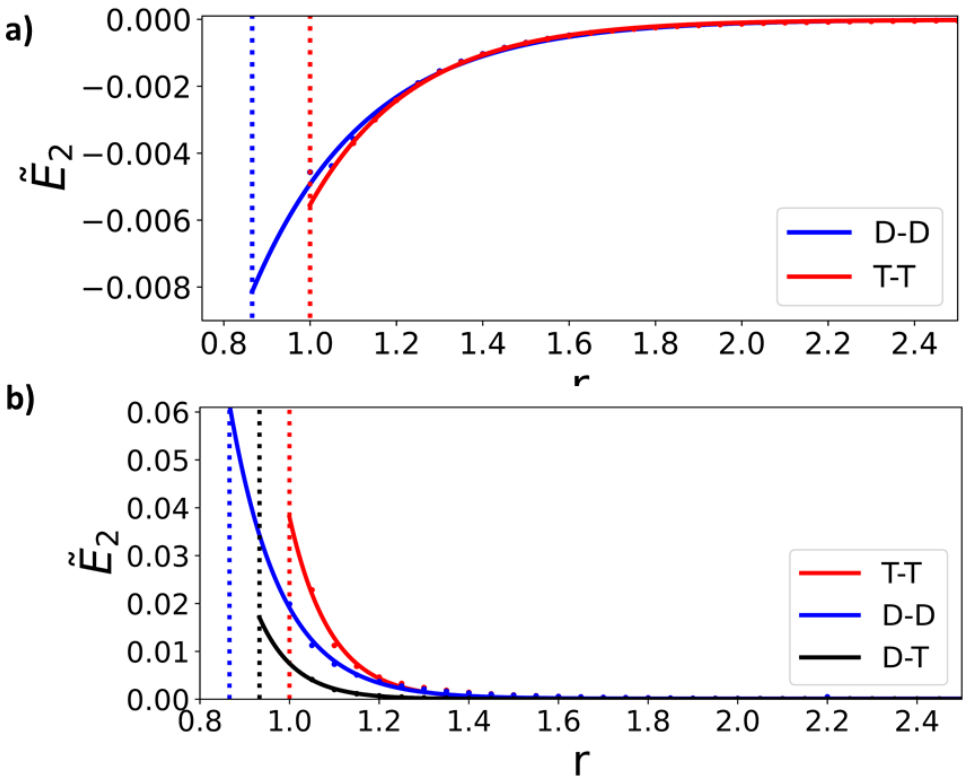

Figure 6-6 Normalised free energy calculations as a function of centre-to-centre expressed in terms of r for Plate 1. Attractive configurations (a) and repulsive interactions (b). The colour coordinated dashed lines indicate the contact distances for each configuration.

slowly at first, then more rapidly as the inter-particle distance decreases. As discussed, a colloidal system can minimize its free energy by overlapping interfacial deformations of the same sign. As the particles approach in Figure 6-6 (a) the T-T interaction lowers the free energy more than the D-D interaction (or increases in the repulsive case (b)) because there is a greater area of deformation which can interact. However, due to undulations on the particle being sited at the corners of the hexagonal plate, this fixes the contact distance for the T-T interaction at r, whereas for the D-D interactions the contact distance is $\sqrt{3}/2\, r$. Therefore, because the D-D can get physically closer it has the lowest energy of the two, we shall show in the following section that this is the reason that Plate 1 favors HCP as the ground state in crystallization. In plot (b) of Figure 6-6 we show the repulsive versions of the same T-T and D-D interactions along with the D-T interaction. The results are in very good qualitative agreement with the results of Soligno *et al.*[63] whom studied the interactions between the capillary hexapoles surrounding cubic particles as discussed in section 6.1.

In order to favor the honeycomb lattice as the ground state we want to design the particle such that the closest contact distance corresponds with the tripole-tripole interaction. We can achieve this by introducing a phase shift of $\pi/6$ between the edge undulations and the hexagonal plate geometry (i.e., Plate 2) so that the T-T contact distance is now $\sqrt{3}/2\, r$ and the D-D contact distance r. In Figure 6-7 we once again illustrate free energy as a function of center-to-center particle separation expressed in terms of r, this time for Plate 2, for attractive (a) and repulsive (b) configurations. As can be seen from (a) the minimum energy state is now the tripole-tripole orientation for the

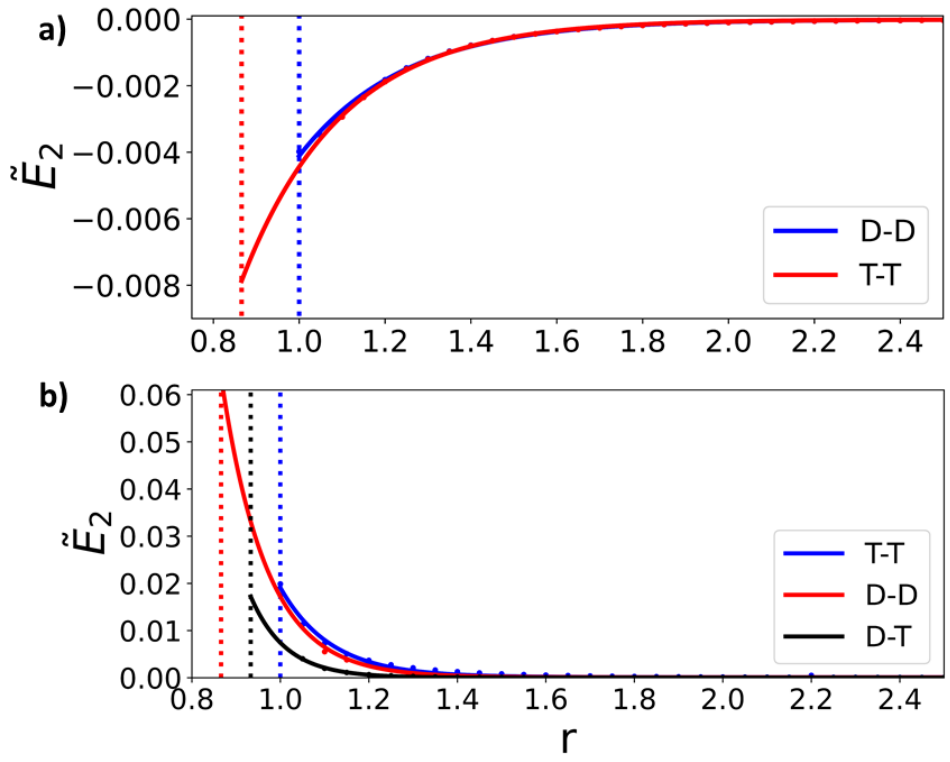

Figure 6-7 Normalised free energy calculations as a function of centre-to-centre expressed in terms of r for Plate 2. Attractive configurations (a) and repulsive interactions (b). The colour coordinated dashed lines indicate the contact distances for each configuration.

attractive interactions and similarly the roles have also been reversed for the repulsive interactions. One interesting observation of the difference between Plates 1 & 2 is that for a given separation (for example $r = 1.1$) the difference in the normalised free energy between the T-T and D-D interactions is much smaller for Plate 2 than it is for Plate 1. We attribute this effect to the slightly larger magnitude of the menisci surrounding plate two (see Figure 6-4 b & d). In the next section we introduce periodic boundary conditions to the simulations in order to calculate the free energy of a variety of crystal structures for Plates 1 & 2.

6.3.3 2D Crystalline Structures

To complete our study of undulating hexagonal platelets we implement periodic boundary conditions within SE and calculate the normalized free energy as a function of area fraction for three different possible crystal structures for each plate. Plate 1 has three likely configurations based on energetically favorable overlapping deformations illustrated in Figure 6-8, a hexagonal close packed (a), honeycomb (b) and a rectangular lattice (c). Interfacial rises and depressions are indicated by green and blue spots respectively with the plates shown at intermediate separations for clarity. The hexagonal close packed (HCP) and rectangular structures involve both the D-D and T-T capillary interactions whereas the honeycomb involves only the T-T capillary interaction. We note that the honeycomb lattice is not merely a HCP with the central particle omitted because the central space is composed entirely of interfacial depressions (or equivalently, rises) which frustrates the inclusion of another particle. In Figure 6-9 we show the equivalent candidate crystal structures for Plate 2, having the equivalents: rectangular (a), kagome (b) and honeycomb (c).

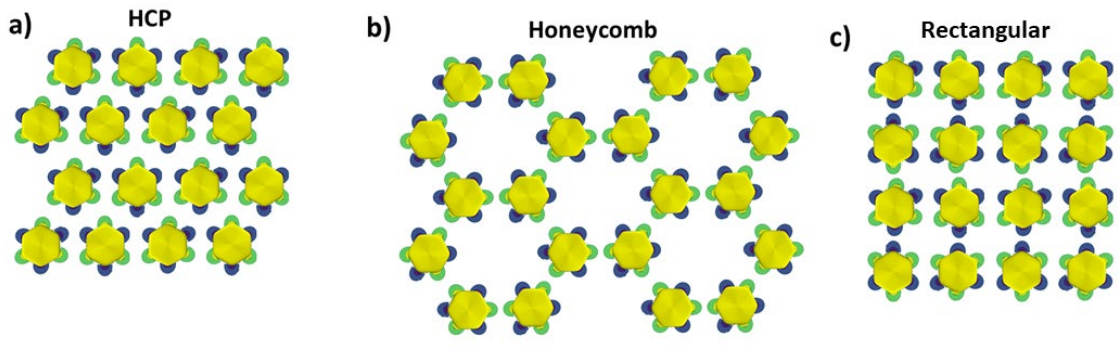

Figure 6-8 Candidate crystal structures for Plate 1 illustrated at intermediate particle separations with blue and green spots indicating interfacial depressions and rises respectively. (a) Hexagonal close packed, (b) honeycomb and (c) rectangular lattice structures.

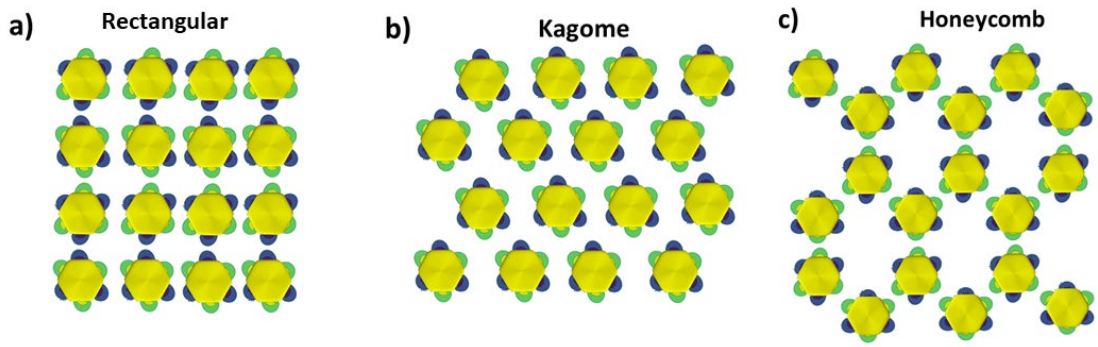

Figure 6-9 Candidate crystal structures for Plate 2 illustrated at intermediate particle separations with blue and green spots indicating interfacial depressions and rises respectively. (a) Rectangular, (b) kagome and (c) honeycomb lattice structures.

Using Surface Evolver with periodic boundary conditions, we calculate the free energy of the unit cell for each configuration. Decreasing the center to center particle separation and normalizing such that $\eta\tilde{E}_{\infty} = {\eta(s)(E(s=\infty) - E(s))}/{\gamma A}$ where $\eta(s)$ is the area fraction, A the particle(s) surface area, γ surface tension and $E(s)$ the free surface energy as calculated from SE. The results are illustrated in Figures 6-10 (a) and (b) for Plates 1 & 2 respectively, where the solid dots indicate the simulation result, solid lines a polynomial fit, dashed lines the area fraction at contact for the relevant structure and finally, the dash dot line is the common tangent construction. The common tangent line gives the lowest energy state for any given value of η i.e., the ground state at $T = 0$. Specifically, the lowest free energy state will be a phase coexistence between the two states linked by the common tangent line. In the case of Plate 1, Figure 6-10 (a), the common tangent construction shows us that the ground state is a coexistence between vacuum and all three phases with the proportions dependent on η, and the global minima the HCP (magenta line) at $\eta = 1$.

In contrast, the periodic simulations of Plate 2, Figure 6-10 (b), the common tangent construction shows us that the ground state is a coexistence between vacuum and the honeycomb (green) and rectangular (blue) lattice structures where the global minima is the rectangular lattice. Interestingly, the phase behavior of Plate 1 resembles

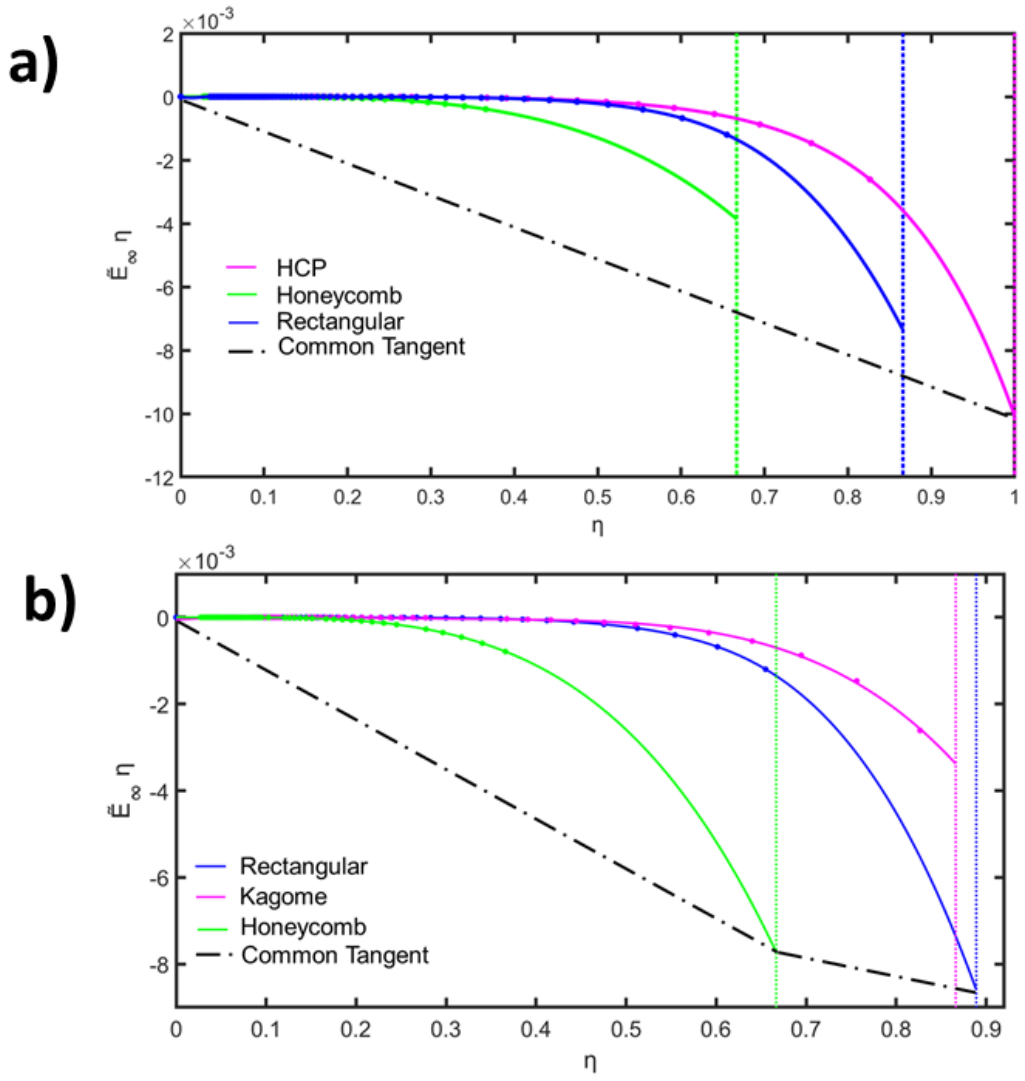

Figure 6-10 Normalised free energy as a function of area fraction for periodic boundary simulations of: (a) Plate 1 in the HCP (magenta), honeycomb (green) and rectangular (blue) lattice structures. (b) Plate 2 in the kagome (magenta), honeycomb (green) and rectangular (blue) lattice structures. Calculations indicated by solid dots accompanied by polynomial fits (solid lines), contact distances (dashed lines) and the common tangent construction (dash dot line).

the capillary interactions of hexapolar deformations surrounding cubic particles in the {111} orientation[63] whereas the phase behavior of Plate 2 is more similar to the hexagonal plates with patterned edges studied by Whitesides *et al.*[35]

Having shown that by making small alterations to the geometry we can theoretically engineer different self-assembled structures we show in the next section that it is possible to take this concept further by distorting the plates shape as well as including surface undulations in order to selectively distinguish between ground states.

6.4 Distorted Hexagonal Plates

In the previous sections we found that by changing the relative orientation between edge undulations and the hexagonal shape, we could stabilise either HCP or honeycomb, but not the kagome lattice structure. In the following we show we can stabilise the kagome lattice by using a distorted hexagon shape and a superposition of multipoles for the edge undulations.

6.4.1 Isolated Particle

Up to this point the parametric representation given in Equation 6-1 has been used to simulate undulating hexagonal platelets and in principle we can use it to create any polyhedron we desire. In the following we distort the hexagonal platelet and 'push' it's edges out such that it resembles an undulating, truncated triangular plate. The shape of interest is illustrated in Figure 6-11 and we refer to it hence forth as a distorted hexagonal plate (DHP). In Figure 6-11 we show contour plots with the particle overlaid for three variations of the DHP, all having different coefficients in Equation 6-1. We define the ratio of the longer edge (L) to the shorter edge (S) as $\alpha = {}^{L}/_{S}$. For Plates 1 & 2 presented in sections 6.1 – 6.3, $\alpha = 1$ resulting in hexagonal plates with a pure hexapole as shown in Figure 6-4. However, In Figure 6-11 the contour plots illustrate the effect varying α has on the meniscus deformations for $\alpha = 2, 2.5, 3$ (left to right). As α

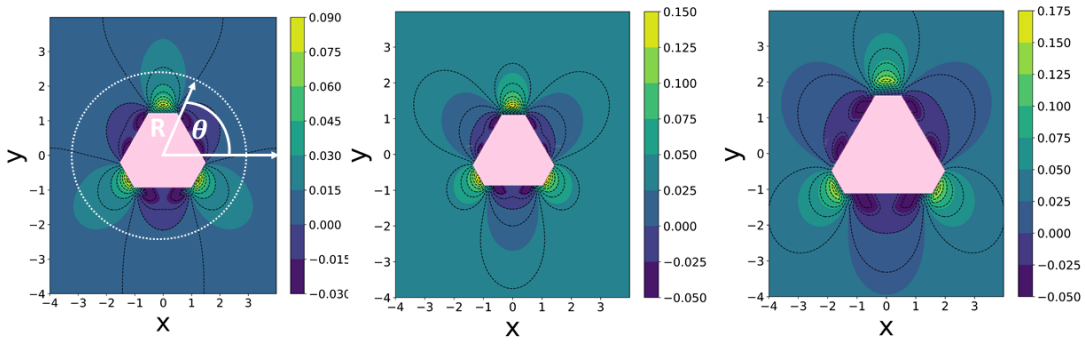

Figure 6-11 Contour plots of the equilibrated interface over the region $6r \times 6r$ centred at the origin with the particle geometry overlaid to demonstrate the effect of increasing α from 2 (a), to 2.5 (b) and finally 3 (c).

increases we observe some general trends in the meniscus contour. The height of the interfacial rise at the short edge increases and extends further out from the particle. This is also true for the depressions but less prominent. We remark that the choices of α are not arbitrary as will be seen shortly.

From the contour data for $\alpha = 2.5$ we extract the height of the meniscus, z, at a fixed radius, $R = 1.5r$ around the particle in the same fashion as shown in Figure 6-4 (b & d), and in Figure 6-12 plot it alongside the undulation of the top edge of the particle at $R = r$ (magenta line). For the meniscus height fitting (blue line) we use a Fourier series to represent the height of the liquid meniscus and due to the three-fold symmetry of the particle we only need to include Fourier modes which are multiples of three. In order to get a faithful representation of the meniscus profile we need to include terms in the Fourier series for $m = 3, 6, 9$. We require the higher order m= 9 term due to distortion from the non-circular shape. The fitting parameters take the form $f(\theta) = A_0 + A_1 \cos 3\theta + A_2 \cos 6\theta + A_3 \cos 9\theta$. Where $A_0 = 0.0108$, $A_1 = 0.03508$, $A_2 = 0.01796$ and $A_3 = 0.003765$. As in Figure 6-4 (c & d) we offset theta such that the peak

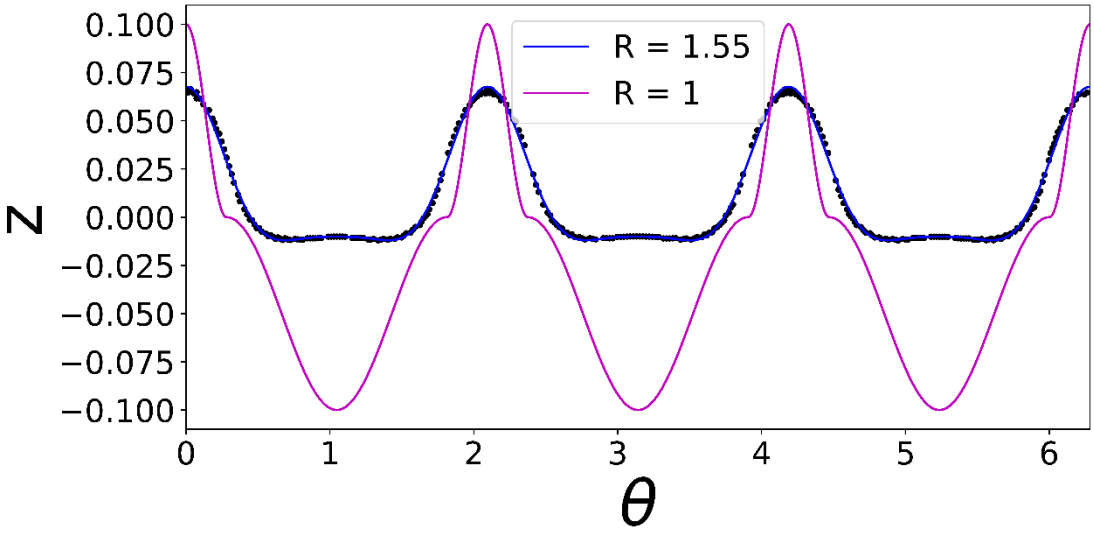

Figure 6-12 Height of the meniscus, z, as a function circular coordinate θ at fixed R as defined in Figure 6-11. The blue line is a Fourier series fit of the simulation data (black dots) at $R = 1.5r$ alongside the undulation of the top edge of the particle at $R = r$ (magenta line).

meniscus height corresponds with $\theta = 0$ allowing us to fit with only even functions without loss of generality. We find the leading order term a hexapole ($m = 3$) as expected.

6.4.2 Pairwise Interactions of Distorted Hexagonal Plates

In Figure 6-13 we study the pairwise interactions for the three side length ratios $\alpha = 2,\ 2.5,3$ (a, b & c respectively). Due to particle symmetry, there are three main capillary interactions, illustrated in the right column of Figure 6-13, which we refer to as: (d) long side short side (LS), (e) short side short side (SS) and (f) long side long side (LL). We again express as the normalized free energy $\tilde{E}_2 = E(R = \infty) - E(R)$ where R is the center-to-center particle separation as before. In all cases the LS interactions are repulsive whereas the SS and LL are attractive. Increasing α increases the distance over which the capillary deformations start to interact from approximately $R = 3$ for $\alpha = 2$ (top) up to approximately $R = 4$ for $\alpha = 3$ (bottom), most clearly seen for the LS interactions (red lines). In order to explain this, we refer back to the remarks on Figure

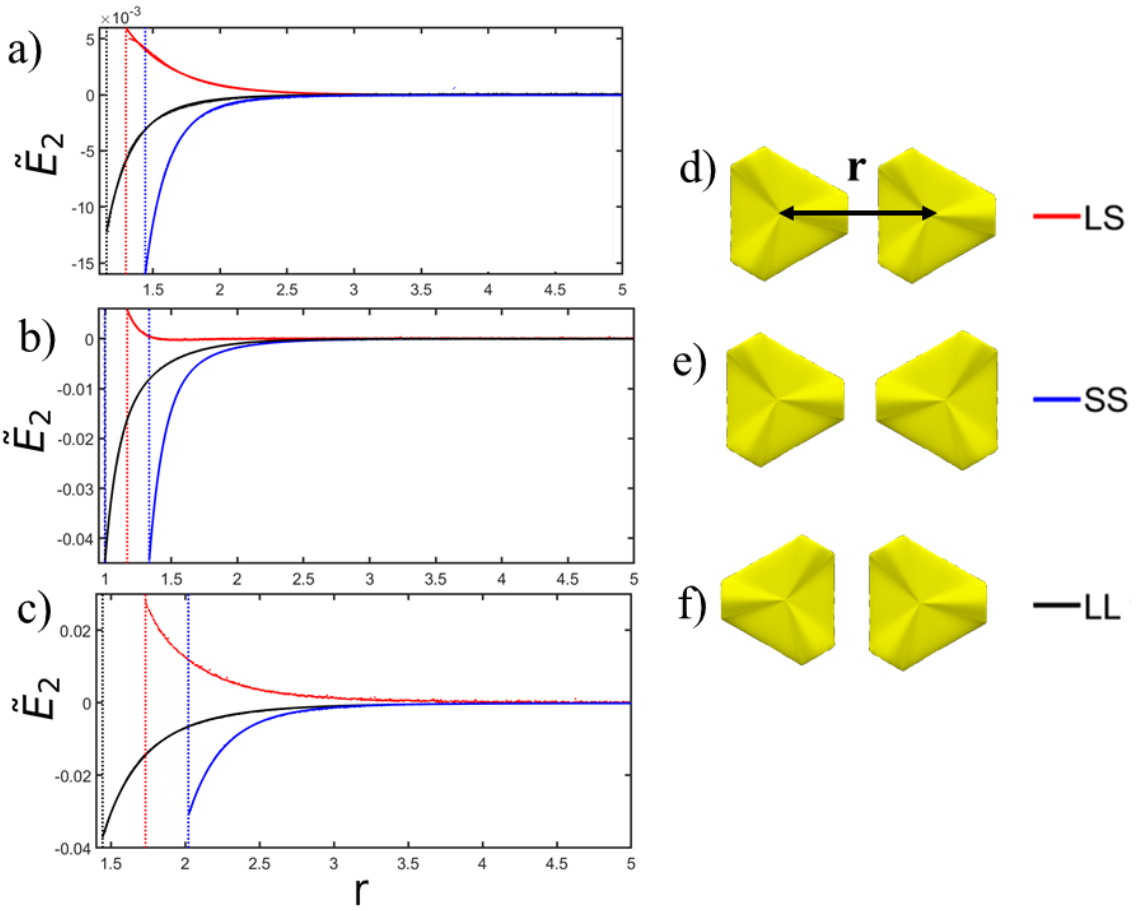

Figure 6-13 Normalized free energy vs center to center separation for side ratios 2 (a), 2.5 (b), and 3 (c) along with graphical illustrations of the three orientational configurations: (d) long-short, (e) short-short (f) long-long.

6-11 for the contour plots of isolated particles and note that increasing the side length ratio increases the peak meniscus height around the short side, the deformations on the longer sides also reach further into the interface taking up a larger area. Fascinatingly, the global minima for $\alpha = 2$ in Figure 6-13 (a) is reached when the short sides are in contact. This is somewhat unusual as the L-L can get physically closer and exclude more interfacial area when in contact. Furthermore, S-S interactions start to decrease in energy sooner than the L-L version in all cases. However, for the larger aspect ratio of three (c) The L-L interaction is the global minima because not only can it get physically closer but the interface it excludes has a much larger deformation area as can be verified from the contour plots in Figure 6-11. The point at which this relationship seems to flip is $\alpha = 2.5$ as can be seen in Figure 6-13 (b) where both the L-L and S-S interactions have approximately the same normalized free energy at contact. For the rest of this chapter, we consider only $\alpha = 2$ because, as we will show later, this produces some interesting results when extended to periodic boundary conditions.

We next make a comparison of our model against a purely theoretical treatment derived by Danov *et al.* which sums up the contributions of each and every mode interacting with each other.[32] We define two particles A & B as illustrated in Figure 6-14, having center to center separation S where Ψ_A and Ψ_B are the angles of rotation of the particles with respect to their initial state in which $\Psi_A = \Psi_B = 0$. Danov *et al.* showed that the change in surface energy as a function of separation is described as

$$\Delta W(L) \approx -\pi\sigma G_0 H_A H_B \cos(m_A\varphi_A - m_B\varphi_B)\frac{r_A^{m_A} r_B^{m_B}}{L^{(m_A+m_B)}} \quad \textbf{(6-6)}$$

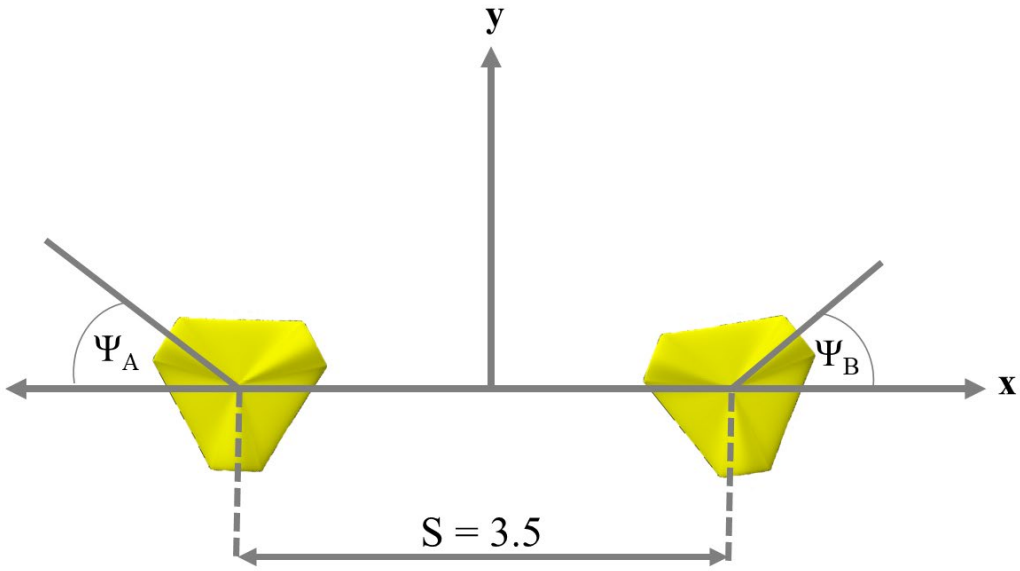

Figure 6-14 Sketch of two particles A and B at fixed center to center separation S. We use the same orientational definitions as Danov *et al.*[32] where Ψ_A and Ψ_B are the angles of rotation of the particles with respect to their initial state in which $\Psi_A = \Psi_B = 0$.

In which σ is the surface tension, H_A & H_B the undulation amplitudes, m_A & m_B the specific combination of modes under consideration, r_A & r_B the distance to the particles edge and the mode dependent G_0 calculated as

$$\sum_{n=1}^{min(m_A,m_B)} \frac{2(-1)^{m_A+m_B} m_A! m_B!}{(m_A-n)!(m_B-n)!n!(n-1)!} \quad \textbf{(6-7)}$$

We use the coefficients from the Fourier fitting shown in Figure 6-12 for the undulation amplitudes and calculate the nine unique terms due to the $m = 3, 6, 9$ modes surrounding each particle interacting with each other. We do this by summing the contributions from the [3,3], [3,6], [3,9], [6,3], [6,6], [6,9], [9,3], [9,6] and [9,9] modes in order to calculate ΔW. This is done firstly for two particles with fixed rotations and decreasing separation, shown in Figure 6-15, in order to compare to our previous pairwise calculations. Secondly, we perform the calculation for two rotating particles at a fixed separation such that $\Psi_A = \Psi_B$ in Figure 6-16.

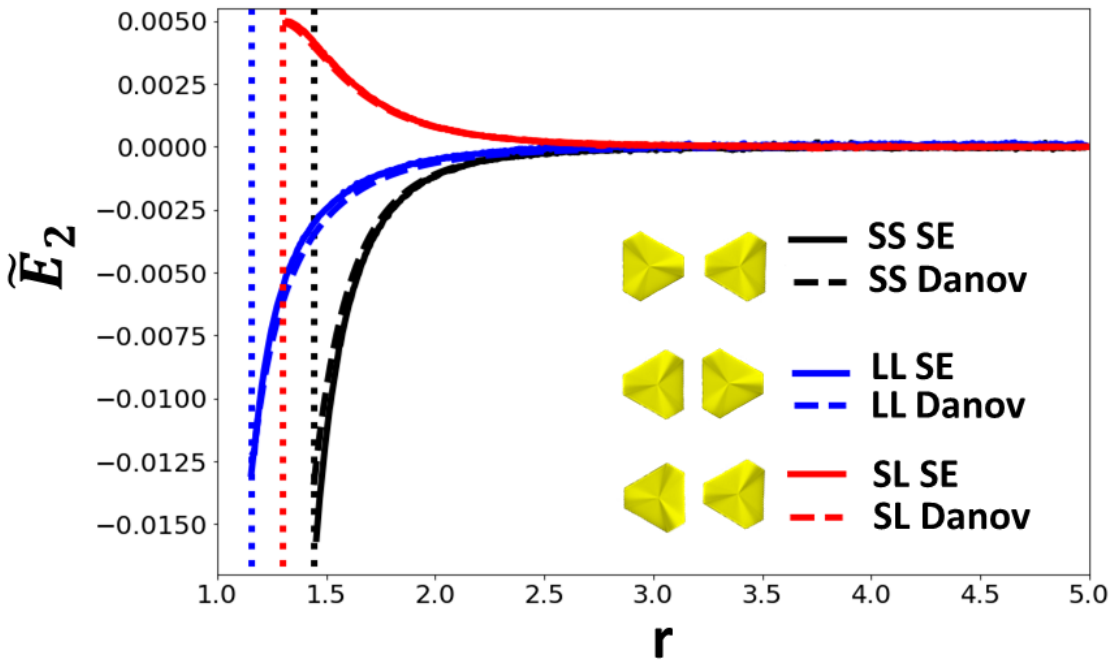

Figure 6-15 Normalized free energy vs center to center separation for $\alpha = 2$ and its comparison with the theoretical model proposed by Danov *et al*[32].

In Figure 6-15 we compare our results for the three orientations studied in Figure 6-13 (a) to the results from Danov's model. We find that the Danov formula slightly underestimates the L-L interaction and slightly overestimates the S-S interaction but otherwise we find excellent agreement with our SE method. Finally, using a fixed separation of $S = 3.5r$ and letting $\Psi_A = \Psi_B$ we compare our model to the model proposed by Danov *et al.* and find excellent agreement with the theoretical treatment once again. With minima occurring at $60°$, $180°$ and $300°$ coinciding with the alignment of the short edges. This implies that for a given separation where the particles start to 'feel' each other's presence there is not only an attractive force driving them together but also a torque acting to align them either short side to short side or long side to long side. This is very similar to the case of two interacting cylinders with a similar explanation of the deformations being concentrated on certain edges leading to the ground state being 'tip-tip'. Therefore, we have a simple set of analytical formulas which can accurately model anisotropic capillary interactions which can be used as inputs in a

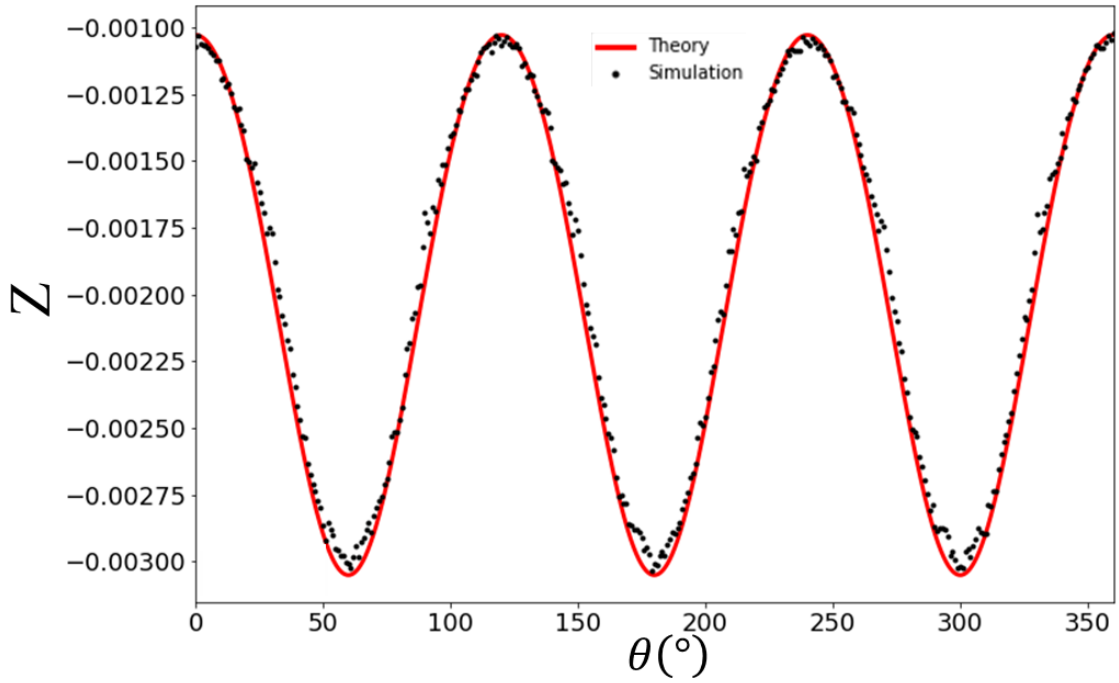

Figure 6-16 Rotating particles at fixed separation, in which $\Psi_A = \Psi_B$ simulation calculations for a given configuration (black dots) vs Danov *et al.* model (solid red line).[32]

particle-based simulation to study self-assembly in future work. It is an interesting feature that the superposition approximation works so well in modeling the systems discussed, we note that we believe this is due to limiting the amplitudes of undulation to be small such that we remain in the linear regime when describing then meniscus modes superposition.

6.4.3 2D Crystalline Structures

To conclude this study, we simulate four possible crystal structures which are derived from considering possible favorable interface overlaps, the low & high density kagome (a, b), rectangular (c) and hexagonal (d) lattices illustrated in Figure 6-17. The structures are sketched at an intermediate particle separation with blue and green spots indicating interfacial depressions and rises respectively with the particles coloured pink and having a side ratio of $\alpha = 2$.

We simulate the structures shown in Figure 6-17 using periodic boundary conditions within SE in the same way previously expressed and normalized in section 6.3.3, presenting the results in Figure 6-18. Intuitively one might expect the high density kagome (solid green line) to be the ground state because it has the highest interfacial coverage at contact (dashed green line), however this is only true at higher densities. At lower densities the open packed kagome (solid red line) is the lowest energy state as shown by the common tangent construction (black dot dashed line) which gives the lowest energy state for any given value of η, i.e., the ground state at $T = 0$. Specifically,

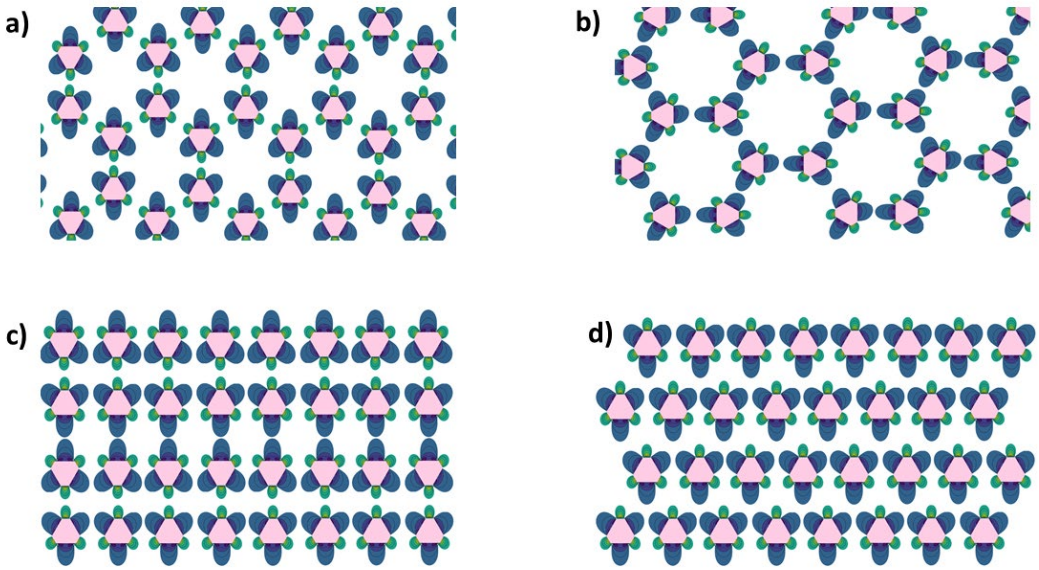

Figure 6-17 Candidate crystal structures for a distorted hexagonal plate, illustrated at intermediate particle separations with blue and green spots indicating interfacial depressions and rises respectively. Illustrations depict a low density kagome *(a)*, high density kagome *(b)*, rectangular*(c)* and hexagonal *(d)* lattice.

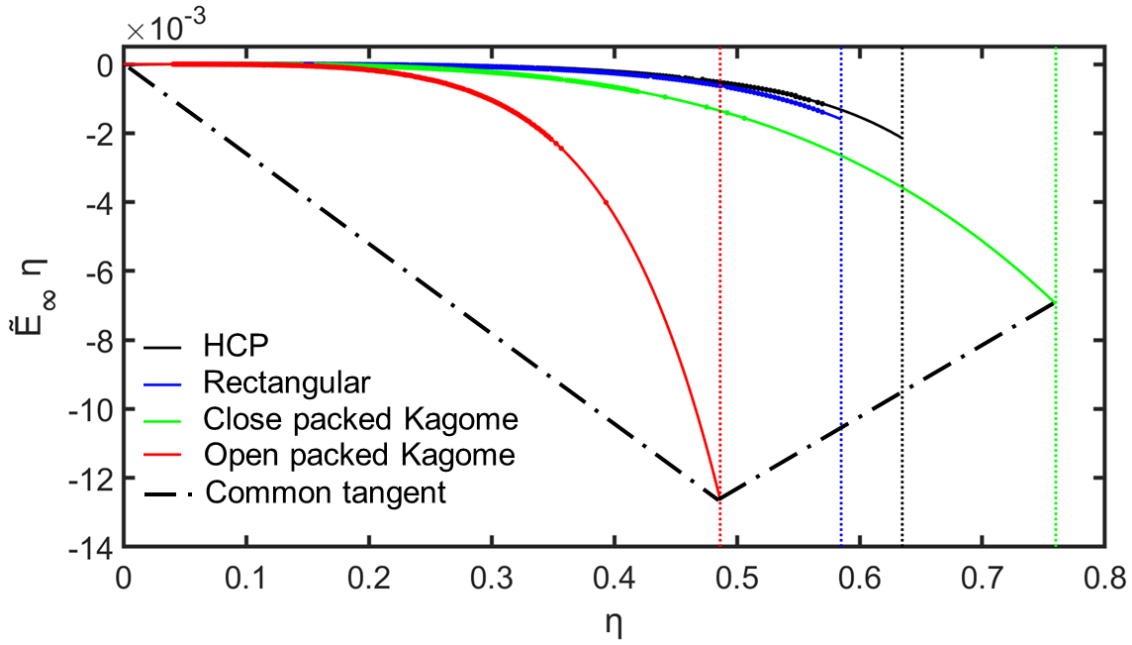

Figure 6-18 Normalised free energy as a function of area density for the 4 unit cells simulated in SE with periodic boundary conditions along with contact density (dashed lines) and common tangent construction (dot-dashed).

the lowest free energy state will be a phase coexistence between the two states linked by the common tangent line, in this case this is the open and closed packed kagome phases. An explanation of this phenomena is that the meniscus deformation around the short sides is significantly higher than on the long sides (therefore requiring more energy to maintain), as was found previously when considering the pairwise interactions in Figure 6-13. Overlapping the deformations originating from the shorts side of the platelets is significantly more energetically favorable than overlapping the deformations originating from the longer sides at an equivalent particle separation. The HCP and rectangular structures are very close energetically, likely due to being highly similar structures in this case, the difference being each alternate row being offset half a particle width.

6.5 Conclusions

We have used the finite element analysis package Surface Evolver to study the self-assembly characteristics of undulating polygonal plates. Specifically, by using undulating

hexagonal platelets and changing the relative phase axis of the capillary multipole and the hexagonal shape we change the self-assembled ground state structure from a hexagonal close packed lattice to honeycomb lattice. Furthermore, by distorting these undulating platelets and changing the ratio of the side lengths, we can tune the ground state structure and direct the self-assembly to assemble to one of two versions of kagome lattices. Finally, We find found that the pairwise interactions of the various undulating polygons could also be captured quantitatively by the analytical formulas of Danov *et al.* which, for future work, can be used to perform particle based Monte Carlo simulations of the self-assembly process.

Chapter 7 Conclusions and Future Work

7.1 Conclusions

In this thesis we have studied the adsorption kinetics of ellipsoidal and cylindrical colloids at liquid interfaces as well as the orientation, capillary forces and self-assembly of hexagonal like platelets. We have investigated the former theoretically by coupling a Langevin model to Surface Evolver simulations and the latter using Surface Evolver.

In Chapter 4, we developed a simple Langevin model which accurately captures the deformation of the liquid meniscus and uses the correct ratio for the translational and rotational particle friction coefficients. The effect of contact line pinning was incorporated into the model by renormalising particle friction coefficients and using the appropriate dynamic contact angle. Using this simple model, we reproduced the monotonic evolution of particle orientation with time that has been observed experimentally. Specifically, we were able to obtain this behaviour by accurately modelling interfacial deformation and particle friction coefficients without the need to explicitly invoke depinning dynamics of the contact line. We were also able to quantitatively model the adsorption dynamics of the individual adsorption coordinates (i.e., adsorption coordinate vs. time) for the experimental ellipsoidal systems of Coertjens *et al.*[24] but not those of Wang *et al*.[23] However, even for the latter case, our model was able to accurately capture the adsorption trajectory (i.e., particle orientation vs. height) of the particles. Our model clarifies the different roles played by capillary, viscous and contact line forces in determining the wetting dynamics of micron-scale objects. Our theoretical model can be used as a predictive tool for designing and controlling the assembly of complex particles at liquid interfaces.

In Chapter 5 we again used Langevin dynamics coupled to a finite element model to study the adsorption kinetics of cylindrical nanorods at an oil/water interface in order to determine the optimum conditions for using adsorption kinetics to assemble nanorods into vertically aligned monolayers. Our Langevin model is more accurate compared to previous models used by de Graaf *et al.*[21] as it accurately captures the deformation of the liquid meniscus during particle adsorption and uses the correct ratio for the rotational to translational friction coefficients for the nanorod.

We found that the end-on state is stable only for non-neutrally wetting cylindrical nanorods**.** We also found that the final orientation of the nanorods at the oil/water interface is determined by their initial attack angle when they contact the liquid interface. In particular, the range of attack angles leading to the end-on state is maximised when nanorods adsorb onto the liquid interface from the energetically favourable phase, i.e., hydrophobic particles from the oil phase and hydrophilic particles from the water phase. Surprisingly, we find that the range of attack angles is only weakly dependent on particle aspect ratio, thus allowing us to use adsorption kinetics to assemble vertically aligned nanorods for a wide range of aspect ratios. However, we found that the energy barrier stabilizing the (metastable) end-on state decreases with increasing aspect ratio so the end-on state becomes kinetically unstable when the aspect ratio of the cylinders is too large. This effect sets an upper limit of $\lesssim 10$ for particle aspect ratios that can be assembled into vertically aligned monolayers using adsorption kinetics.

Since only some attack angles lead to the end-on state, in the absence of an external field, only a fraction of nanorods that contact the liquid interface end

up in the end-on state (typically $\lesssim$40% even under optimum conditions). However, by pre-aligning the nanorods in the more polar bulk phase with experimentally achievable electric fields, we can effectively increase this fraction to 100%. Our kinetic assembly method is generic and can be used to assemble nanorods with a range of diameters, aspect ratios and materials (e.g., gold, silver, aluminium, copper, polymer, silica etc.). As such, it represents a versatile, low-cost and powerful platform for fabricating vertically aligned monolayers of nanorods for metamaterial applications.

In Chapter 6, we studied the self-assembly of undulating polygonal plates. Specifically, by using undulating hexagonal platelets and changing the relative phase axis of the capillary multipole and the hexagonal shape we can change the self-assembled ground state structure from hexagonal close packed to honeycomb. By distorting these platelets into distorted hexagons and changing the ratio of the long to short side lengths, we were able to tune the self-assembled ground state structure to two different versions of kagome lattices. Finally, we found that the pairwise interactions between the various undulating polygons can be captured quantitatively using the analytical formulas of Danov *et al*.[32] for the interaction between capillary multipoles. The work in this chapter provides a proof of concept for engineering directed self-assembly by manipulating particle shape alone. Having developed a predictive model for studying the adsorption of anisotropic particles at a liquid interface, a natural next step would be to use the model to study the adsorption kinetics of particles with other anisotropic shapes, e.g., cubes.

In Chapter 6 we determined the conditions required to assemble nano-rods in the end-on state using adsorption kinetics. We hope these calculations will stimulate

further efforts to realize this novel assembly method experimentally. Finally, we showed that the Danov formula can accurately capture the pairwise capillary interactions between polygons with undulating edges. A natural next step for this research would be to use these calculated interaction potentials to carry out Monte Carlo simulations for an ensemble of such particles and also to fabricate the necessary shapes (e.g., using 3D printing) to study the self-assembly of such particles experimentally.

7.2 Future Work

Having developed a simple theoretical model which can be used as a predictive tool for designing and controlling the assembly of colloidal particles at an immiscible interface a natural next step is to use it to study more anisotropic particles. Furthermore, due to the nature of the finite element analysis software, it would be straight forward to introduce surface defects to the particles under investigation to more accurately model reality. While doing this would allow investigation into pinning sites it would not be capable of modeling contact angle hysteresis due to the nature of the model being a quasi-static system.

In Chapter 6 we showed that the Danov formula can accurately capture pairwise interactions between our engineered particles. To push this study further It is desirable to use these calculated potential profiles and carry out Monte Carlo simulations for these systems. Such a study would be fairly straight forward and make a suitable undergraduate dissertation project.

Finally, to continue the research presented in Chapter 6 on hexagonal platelets and variations of them, an experimental validation of this would be desirable. The very real difficulties with respect to an experimental demonstration of these concepts is the particle fabrication steps and we envision this as a two-step process. Firstly, the low

hanging fruit is to use off the shelf 3D printers to print the various (hollow) particles on the millimeter scale and use density matching to keep them at the interface using much the same experimental approach as Whitesides *et al.*[42] Given that 3D printers print layer by layer an interesting branch of this experimental demonstration would be to perform two versions of it, firstly printing with PLA and secondly using particles printed from ABS. In the first iteration the particles are taken as is from the printer with their rippled edges (over 0.16mm – 0.4mm layer height range) and in the second iteration a single batch printed and post processed with the acetone vapor techniques to remove the ripples. One would expect pinning effects to become apparent at some point over this range. To really drive the research to smaller length scales it would require either the use of stereolithography or two photon lithography which presents a financial barrier to the research if not collaborating with a research institution with access to equipment and expertise in the areas.

References

1 B. P. Binks and T. S. Horozov, in *Colloidal Particles at Liquid Interfaces*, eds. B. P. Binks and T. S. Horozov, Cambridge University Press, Cambridge, 1st edn., 2006, pp. 1–74.

2 V. A. Hackley and C. F. Ferraris, NIST Recommended Practice Guide: The Use of Nomenclature in Dispersion Science and Technology, https://www.nist.gov/publications/nist-recommended-practice-guide-use-nomenclature-dispersion-science-and-technology, (accessed 20 January 2022).

3 W. Ramsden, *Proc. R. Soc. London*, 1904, **72**, 156–164.

4 S. U. Pickering, *J. Chem. Soc. Trans.*, 1907, **91**, 2001–2021.

5 R. Aveyard, B. P. Binks and J. H. Clint, *Adv. Colloid Interface Sci.*, 2003, **100**, 503–546.

6 K. P. Velikov and O. D. Velev, in *Colloidal Particles at Liquid Interfaces*, eds. B. P. Binks and T. S. Horozov, Cambridge University Press, Cambridge, 1st edn., 2006, p. 225 297.

7 J. Forth, P. Y. Kim, G. Xie, X. Liu, B. A. Helms and T. P. Russell, *Adv. Mater.*, 2019, **31**, 1–110.

8 B. B. Mishra, B. B. Patel and S. Tiwari, *Nanomedicine Nanotechnology, Biol. Med.*, 2010, **6**, 9–24.

9 A. V. Nguyen, R. J. Pugh and G. J. Jameson, in *Colloidal Particles at Fluid Interfaces*, eds. B. P. Binks and T. S. Horozov, Cambridge University Press, 1st edn., 2006, pp. 328–382.

10 C. C. Ho, A. Keller, J. A. Odell and R. H. Ottewill, *Colloid Polym. Sci.*, 1993, **271**, 469–479.

11 G. González-Rubio, V. Kumar, P. Llombart, P. Díaz-Núñez, E. Bladt, T. Altantzis, S. Bals, O. Peña-Rodríguez, E. G. Noya, L. G. Macdowell and A. Guerrero-Martínez, *ACS Nano*, 2019, **13**, 4424–4435.

12 S. E. Skrabalak, L. Au, X. Li and Y. Xia, *Nat. Protoc.*, 2007, **2**, 2182–2190.

13 B. Khodashenas and H. R. Ghorbani, *Arab. J. Chem.*, 2019, **1**, 1823–1838.

14 Z. Gong, T. Hueckel, G. R. Yi and S. Sacanna, *Nature*, 2017, **550**, 234–238.

15 L. Rossi, V. Soni, D. J. Ashton, D. J. Pine, A. P. Philipse, P. M. Chaikin, M. Dijkstra, S. Sacanna and W. T. M. Irvine, *Proc. Natl. Acad. Sci.*, 2015, **112**, 5286–5290.

16 S. Sacanna and D. J. Pine, *Curr. Opin. Colloid Interface Sci.*, 2011, **16**, 96–105.

17 N. Ballard and S. A. F. Bon, *J. Colloid Interface Sci.*, 2015, **448**, 533–544.

18 J. C. Loudet, A. G. Yodh and B. Pouligny, *Phys. Rev. Lett.*, 2006, **97**, 018304.

19 J. C. Loudet, A. M. Alsayed, J. Zhang and A. G. Yodh, *Phys. Rev. Lett.*, 2005, **94**, 018301.

20 E. P. Lewandowski, M. Cavallaro, L. Botto, J. C. Bernate, V. Garbin and K. J. Stebe, *Langmuir*, 2010, **26**, 15142–15154.

21 J. de Graaf, M. Dijkstra and R. R. van Roij, *J. Chem. Phys.*, 2010, **132**, 164902.

22 F. Günther, S. Frijters and J. Harting, *Soft Matter*, 2014, **10**, 4977–4989.

23 A. Wang, W. B. Rogers and V. N. Manoharan, *Phys. Rev. Lett.*, 2017, **119**, 108004.

24 S. Coertjens, R. De Dier, P. Moldenaers, L. Isa and J. Vermant, *Langmuir*, 2017, **33**, 2689–97.

25 B. J. Newton and D. M. A. Buzza, *Soft Matter*, 2016, **12**, 5285–5296.

26 G. A. Wurtz, W. Dickson, D. O'Connor, R. Atkinson, W. Hendren, P. Evans, R. Pollard and A. V. Zayats, *Opt. Express*, 2008, **16**, 7460–7470.

27 P. Bartlett, *Phys. Rev. Lett.*, 1992, **68**, 3801–3805.

28 M. D. Eldridge, P. A. Madden and D. Frenkel, *Nature*, 1993, **365**, 35–37.

29 M. E. Leunissen, C. G. Christova, A. P. Hynninen, C. P. Royall, A. I. Campbell, A. Imhof, M. Dijkstra, R. Van Roij and A. Van Blaaderen, *Nature*, 2005, **437**, 235–240.

30 E. V. Shevchenko, D. V. Talapin, N. A. Kotov, S. O'Brien and C. B. Murray, *Nature*, 2006, **439**, 55–59.

31 P. A. Kralchevsky and K. Nagayama, *Langmuir*, 1994, **10**, 23–36.

32 K. D. Danov, P. A. Kralchevsky, B. N. Naydenov and G. Brenn, *J. Colloid Interface Sci.*, 2005, **287**, 121–134.

33 K. D. Danov and P. A. Kralchevsky, *Adv. Colloid Interface Sci.*, 2010, **154**, 91–103.

34 D. Vella and L. Mahadevan, *Am. J. Phys.*, 2005, **73**, 817–825.

35 N. B. Bowden, M. Weck, I. S. Choi and G. M. Whitesides, *Acc. Chem. Res.*, 2001, **34**, 231–238.

36 L. Botto, L. Yao, R. L. Leheny and K. J. Stebe, *Soft Matter*, 2012, **8**, 4971–4979.

37 M. P. Boneschanscher, W. H. Evers, J. J. Geuchies, T. Altantzis, B. Goris, F. T. Rabouw, S. A. P. van Rossum, H. S. J. van der Zant, L. D. A. Siebbeles, G. Van Tendeloo, I. Swart, J. Hilhorst, A. V. Petukhov, S. Bals and D. Vanmaekelbergh, *Science.*, 2014, **344**, 1377–1380.

38 W. H. Evers, B. Goris, S. Bals, M. Casavola, J. De, R. Van Roij, M. Dijkstra and D. Vanmaekelbergh, *Nano Lett.*, 2013, **13**, 2317–23.

39 C. Anzivino, G. Soligno, R. van Roij and M. Dijkstra, *Soft Matter*, 2021, **17**, 965–975.

40 C. J. Myers, M. Celebrano and M. Krishnan, *Nat. Nanotechnol.*, 2015, **10**, 886–891.

41 International Space Station Research on Tiny Colloid Particles Yields Big Results, https://www.nasa.gov/mission_pages/station/research/news/iss-research-colloid-particles-ace, (accessed 1 March 2022).

42 N. Bowden, A. Terfort, J. Carbeck and G. M. Whitesides, *Science.*, 1997, **276**, 233–235.

43 S. Coertjens, R. De Dier, P. Moldenaers, L. Isa and J. Vermant, *Langmuir*, 2017, **33**, 2689–2697.

44 A. Wang, W. B. Rogers and V. N. Manoharan, *Phys. Rev. Lett.*, 2017, **119**, 108004.

45 E. P. Lewandowski, P. C. Searson and K. J. Stebe, *J. Phys. Chem. B*, 2006, **110**, 4283–4290.

46 P. Pieranski, *Phys. Rev. Lett.*, 1980, **45**, 569–572.

47 N. Ballard, A. D. Law and S. A. F. Bon, *Soft Matter*, 2019, **15**, 1186–1199.

48 B. J. Newton, K. A. Brakke and D. M. Buzza, *Phys. Chem. Chem. Phys.*, 2014, **16**, 26051–26058.

49 S. Levine, B. D. Bowen and S. J. Partridge, *Colloids and Surfaces*, 1989, **38**, 325–343.

50 B. P. Binks, *Curr. Opin. Colloid Interface Sci.*, 2002, **7**, 21–41.

51 B. P. Binks and J. H. Clint, *Langmuir*, 2002, **18**, 1270–1273.

52 P. G. de Gennes, F. Brochard-Wyart and D. Quéré, *Capillarity and wetting phenomena drops, bubbles, pearls, waves*, Springer, New York, 1st edn., 2004.

53 L. Gao and T. J. McCarthy, *Langmuir*, 2006, **22**, 6234–6237.

54 H. B. Eral, D. J. C. M. T. Mannetje and J. M. Oh, *Colloid Polym. Sci.*, 2013, **291**, 247–260.

55 A. V. Rapacchietta, A. W. Neumann and S. N. Omenyi, *J. Colloid Interface Sci.*, 1977, **59**, 541–554.

56 D. Y. C. Chan, J. D. Henry and L. R. White, *J. Colloid Interface Sci.*, 1981, **79**, 410–418.

57 J. de Graaf, M. Dijkstra and R. van Roij, *Phys. Rev. E*, 2009, **80**, 051405.

58 J. N. Israelachvili, *Intermolecular and Surface Forces*, Academic Press, San Diego, 3rd edn., 2011.

59 J. P. Hirth, T. Jøssang and J. Lothe, *J. Appl. Phys.*, 1966, **37**, 110–116.

60 A. Amirfazli and A. W. Neumann, *Adv. Colloid Interface Sci.*, 2004, **110**, 121–141.

61 B. M. Law, S. P. McBride, J. Y. Wang, H. S. Wi, G. Paneru, S. Betelu, B. Ushijima, Y. Takata, B. Flanders, F. Bresme, H. Matsubara, T. Takiue and M. Aratono, *Prog. Surf. Sci.*, 2017, **92**, 1–39.

62 B. J. Newton, R. Mohammed, G. B. Davies, L. Botto and D. M. A. Buzza, *ACS Omega*, 2018, **3**, 14962–14972.

63 G. Soligno, M. Dijkstra and R. van Roij, *Phys. Rev. Lett.*, 2016, **116**, 258001.

64 D. Stamou, C. Duschl and D. Johannsmann, *Phys. Rev. E*, 2000, **62**, 5263–5272.

65 L. Botto, E. P. Lewandowski, M. Cavallaro and K. J. Stebe, *Soft Matter*, 2012, **8**, 9957–71.

66 G. B. Davies, T. Krüger, P. Coveney, J. Harting and F. Bresme, *Adv. Mater.*, 2014, **26**, 6715–6719.

67 H. Lehle, E. Noruzifar and M. Oettel, *Eur. Phys. J. E*, 2008, **26**, 151–160.

68 G. Soligno, M. Dijkstra and R. R. Van Roij, *Soft Matter*, 2018, **14**, 42–60.

69 J. Hu, S. Zhou, Y. Sun, X. Fang and L. Wu, *Chem. Soc. Rev.*, 2012, **41**, 4356–4378.

70 R. N. Wenzel, *Ind. Eng. Chem.*, 1936, **28**, 988–994.

71 A. B. Cassie and S. Baxter, *Trans. Faraday Soc.*, 1944, 546–51.

72 Y. Nonomura and S. Komura, *J. Colloid Interface Sci.*, 2008, **317**, 501–506.

73 Y. Nonomura, S. Komura and K. Tsujii, *Langmuir*, 2005, **21**, 9409–9411.

74 Y. Nonomura, S. Komura and K. Tsujii, *J. Phys. Chem. B*, 2006, **110**, 13124–13129.

75 C. Huh and L. E. Scriven, *J. Colloid Interface Sci.*, 1971, **35**, 85–101.

76 P. G. de Gennes, *Rev. Mod. Phys.*, 1985, **57**, 827–863.

77 J. A. Marsh and S. Garoff, *Phys. Rev. Lett.*, 1993, **70**, 2778.

78 V. N. Paunov, *Langmuir*, 2003, **19**, 7970–7976.

79 T. D. Blake and J. M. Haynes, *J. Colloid Interface Sci.*, 1969, **30**, 421–423.

80 T. M. Ruhland, A. H. Gröschel, N. Ballard, T. S. Skelhon, A. Walther, A. H. E. Müller and S. A. F. Bon, *Langmuir*, 2013, **29**, 1388–1394.

81 B. J. Park and D. Lee, *ACS Nano*, 2012, **6**, 782–790.

82 A. R. Morgan, N. Ballard, L. A. Rochford, G. Nurumbetov, T. S. Skelhon and S. A. F. Bon, *Soft Matter*, 2013, **9**, 487–491.

83 B. J. Park and D. Lee, *Soft Matter*, 2012, **8**, 7690–7698.

84 S. O. Morgan, J. Fox, C. Lowe, A. M. Adawi, J. S. G. Bouillard, G. J. Stasiuk, T. S. Horozov and D. M. A. Buzza, *Phys. Rev. E*, 2021, **103**, 42604.

85 S. Succi, *The Lattice Boltzmann Equation: for Fluid Dynamics and Beyond*, Oxford University Press, Oxford, 2001.

86 X. Shan and H. Chen, *Phys. Rev. E*, 1993, **47**, 1815–1819.

87 S. Lee, Y. Roichman, G. Yi, S. Kim, S. Yang, A. van Blaaderen, P. van Oostrum and D. G. Grier, *Opt. Express*, 2007, **15**, 18275–18282.

88 B. J. Park and E. M. Furst, *Langmuir*, 2008, **24**, 13383–13392.

89 D. M. Kaz, R. Mcgorty, M. Mani, M. P. Brenner and V. N. Manoharan, *Nat. Mater.*, 2012, **11**, 138–142.

90 A. Wang, R. Mcgorty, D. M. Kaz and V. N. Manoharan, *Soft Matter*, 2016, **12**, 8958–8967.

91 C. E. Colosqui, J. F. Morris and J. Koplik, *Phys. Rev. Lett.*, , DOI:10.1103/PhysRevLett.111.028302.

92 G. Boniello, C. Blanc, D. Fedorenko, M. Medfai, N. Ben Mbarek, M. In, M. Gross, A. Stocco and M. Nobili, *Nat. Mater.*, 2015, **14**, 908–911.

93 L. Isa, F. Lucas, R. Wepf and E. Reimhult, *Nat. Commun.*, 2011, **2**, 1–9.

94 L. Isa, *Chim. Int. J. Chem.*, 2013, **67**, 231–235.

95 F. Bresme and M. Oettel, *J. Phys. Condens. Matter*, 2007, **19**, 413101.

96 Z. Zhang, P. Pfleiderer, A. B. Schofield, C. Clasen and J. Vermant, *J. Am. Chem. Soc.*, 2011, **133**, 392–395.

97 J. C. Loudet and B. Pouligny, *Europhys. Lett.*, 2009, **85**, 28003.

98 Q. Song and H. Schönherr, *Langmuir*, 2019, **35**, 6742–6751.

99 Q. Song, M. Steuber, S. I. Druzhinin and H. Schönherr, *Angew. Chemie - Int. Ed.*, 2019, **131**, 5300–5304.

100 W. Beugeling, E. Kalesaki, C. Delerue, Y. M. Niquet, D. Vanmaekelbergh and C. M. Smith, *Nat. Commun.*, 2015, **6**, 1–7.

101 O. J. Cayre and V. N. Paunov, *J. Mater. Chem.*, 2004, **14**, 3300–3302.

102 D. L. Hu and J. W. M. Bush, *Nature*, 2005, **437**, 733–736.

103 D. B. Wolfe, A. Snead, C. Mao, N. B. Bowden and G. M. Whitesides, *Langmuir*, 2003, **19**, 2206–2214.

104 P. W. K. Rothemund, *Proc. Natl. Acad. Sci.*, 2000, **97**, 984–989.

105 C. B. Murray, C. R. Kagan and M. G. Bawendi, *Science.*, 1995, **270**, 1335–1338.

106 V. N. Paunov, *Langmuir*, 1998, **14**, 5088–5097.

107 P. Velikov, K, F. Durst and D. Velev, O, *Langmuir*, 1998, **14**, 1148–1155.

108 G. S. Lazarov, N. D. Denkov, O. D. Velev, P. A. Kralchevsky and K. Nagayama, *J. Chem. Soc. Faraday Trans.*, 1994, **90**, 2077–2083.

109 C. A. Mirkin, R. L. Letsinger, R. C. Mucic and J. J. Storhoff, *Nature*, 1996, **382**, 607–609.

110 N. C. Seeman, *Angew. Chemie - Int. Ed.*, 1998, **37**, 3220–3238.

111 M. Trau, D. A. Saville and A. Aksay, *Science.*, 1996, **272**, 706–709.

112 M. Adams, Z. Dogic, S. L. Keller and S. Fraden, *Nature*, 1998, **393**, 349–352.

113 S. E. Lohse and C. J. Murphy, *Chem. Mater.*, 2013, **25**, 1250–1261.

114 K. A. Brakke, *Exp. Math.*, 1992, **1**, 141–165.

115 K. A. . Brakke, *Philos. Trans. R. Soc. London. Ser. A Math. Phys. Eng. Sci.*, 1996, **354**, 2143–2157.

116 A. I. Rusanov and V. Prokhorov, *Interfacial Tensiometry*, Elsevier, Amsterdam, 1st edn., 1996.

117 G. Morris, S. J. Neethling and J. J. Cilliers, *J. Colloid Interface Sci.*, 2011, **354**, 380–385.

118 K. Asanovic, R. Bodik, B. C. Catanzaro, J. J. Gebis, P. Husbands, K. Keutzer, D. A. Patterson, W. L. Plishker, J. Shalf, S. W. Williams and K. A. Yelick, The Landscape of Parallel Computing Research: a View from Berkeley., https://www2.eecs.berkeley.edu/Pubs/TechRpts/2006/EECS-2006-183.html, (accessed 2 February 2022).

119 J. da Silva Ribeiro, PhD Thesis, Universidade do Minho, 2015.

120 D. Walter, Computational Complexity Theory, https://plato.stanford.edu/archives/fall2021/entries/computational-complexity/, (accessed 3 February 2022).

121 A. D. Dinsmore, M. F. Hsu, M. G. Nikolaides, M. Marquez, A. R. Bausch and D. A. Weitz, *Science.*, 2002, **298**, 1006–1009.

122 E. Dickinson, *Curr. Opin. Colloid Interface Sci.*, 2010, **15**, 40–49.

123 B. P. Binks and R. Murakami, *Nat. Mater.*, 2006, **5**, 865–869.

124 P. Aussillous and D. Quéré, *Nature*, 2001, **411**, 924–927.

125 K. Stratford, R. Adhikari, I. Pagonabarraga, J. C. Desplat and M. E. Cates, *Science.*, 2005, **309**, 2198–2201.

126 E. M. Herzig, K. A. White, A. B. Schofield, W. C. K. Poon and P. S. Clegg, *Nat. Mater.*, 2007, **6**, 966–971.

127 T. D. Blake, *J. Colloid Interface Sci.*, 2006, **299**, 1–13.

128 F. S. Günther, PhD Thesis, Eindhoven University of Technology, 2017.

129 S. Coertjens, P. Moldenaers, J. Vermant and L. Isa, *Langmuir*, 2014, **30**, 4289–4300.

130 M. Doi and S. F. Edwards, *The Theory of Polymer Dynamics*, Oxford University Press, Oxford, 1st edn., 1988.

131 J. Happel and H. Brenner, *Low Reynolds number hydrodynamics: with special applications to particulate media*, Springer Science & Business Media, Berlin, 2012.

132 R. H. Davis, J. A. Schonberg and J. M. Rallison, *Phys. Fluids A*, 1989, **1**, 77–81.

133 R. Kubo, *Reports Prog. Phys.*, 1966, **29**, 255.

134 J. C. Berg, *Wettability*, CRC Press, 1st edn., 1993.

135 K. Tauer, in *Colloids and Colloid Assemblies: Synthesis, Modification, Organization and Utilization of Colloid Particles*, 2004, pp. 1–51.

136 J. D. Feick, N. Chukwumah, A. E. Noel and D. Velegol, *Langmuir*, 2004, **20**, 3090–3095.

137 O. D. Velev and S. Gupta, *Adv. Mater.*, 2009, **21**, 1897–1905.

138 G. Xie, J. Forth, Y. Chai, P. D. Ashby, B. A. Helms and T. P. Russell, *Chem*, 2019, **5**, 2678–2690.

139 B. Madivala, J. Fransaer and J. Vermant, *Langmuir*, 2009, **25**, 2718–2728.

140 D. Vestler, I. Shishkin, E. A. Gurvitz, M. E. Nasir, A. Ben-Moshe, A. P. Slobozhanyuk, A. V. Krasavin, T. Levi-Belenkova, A. S. Shalin, P. Ginzburg, G. Markovich and A. V. Zayats, *Opt. Express*, 2018, **26**, 17841–17848.

141 A. V. Kabashin, P. Evans, S. Pastkovsky, W. Hendren, G. A. Wurtz, R. Atkinson, R. Pollard, V. A. Podolskiy and A. V. Zayats, *Nat. Mater.*, 2009, **8**, 867–871.

142 J. Gao, X. Wu, Q. Li, S. Du, F. Huang, L. Liang, H. Zhang, F. Zhuge, H. Cao and Y. Song, *Adv. Mater.*, 2017, **29**, 1605324.

143 G. A. Wurtz, R. Pollard, W. Hendren, G. P. Wiederrecht, D. J. Gosztola, V. A. Podolskiy and A. V. Zayats, *Nat. Nanotechnol.*, 2011, **6**, 107–111.

144 D. J. Roth, A. V. Krasavin, A. Wade, W. Dickson, A. Murphy, S. Kéna-Cohen, R. Pollard, G. A. Wurtz, D. Richards, S. A. Maier and A. V. Zayats, *ACS Photonics*, 2017, **4**, 2513–2521.

145 D. P. Lyvers, J. M. Moon, A. V. Kildishev, V. M. Shalaev and A. Wei, *ACS Nano*, 2008, **2**, 2569–2576.

146 X. D. Tian, Y. Lin, J. C. Dong, Y. J. Zhang, S. R. Wu, S. Y. Liu, Y. Zhang, J. F. Li and Z. Q. Tian, *Adv. Opt. Mater.*, 2017, **5**, 1700581.

147 Z. Zhang and M. Lin, *J. Mater. Chem. C*, 2014, **2**, 4545–4551.

148 R. A. Alvarez-Puebla, A. Agarwal, P. Manna, B. P. Khanal, P. Aldeanueva-Potel, E. Carbó-Argibay, N. Pazos-Pérez, L. Vigderman, E. R. Zubarev, N. A. Kotov and L. M. Liz-Marzán, *Proc. Natl. Acad. Sci.*, 2011, **108**, 8157–8161.

149 K. Kim, H. S. Han, I. Choi, C. Lee, S. G. Hong, S. H. Suh, L. P. Lee and T. Kang, *Nat. Commun.*, 2013, **4**, 1–9.

150 G. A. Wurtz, P. R. Evans, W. Hendren, R. Atkinson, W. Dickson, R. J. Pollard, A. V Zayats, W. Harrison and C. Bower, *Nano Lett.*, 2007, **7**, 1297–1303.

151 A. D. Neira, N. Olivier, M. E. Nasir, W. Dickson, G. A. Wurtz and A. V. Zayats, *Nat. Commun.*, 2015, **6**, 1–8.

152 P. R. Evans, G. A. Wurtz, R. Atkinson, W. Hendren, D. O'Connor, W. Dickson, R. J. Pollard and A. V. Zayats, *J. Phys. Chem. C*, 2007, **111**, 12522–12527.

153 K. Takahashi, S. J. Limmer, Y. Wang and G. Cao, *J. Phys. Chem. B*, 2004, **108**, 9795–9800.

154 D. Zschech, D. H. Kim, A. P. Milenin, R. Scholz, R. Hillebrand, C. J. Hawker, T. P. Russell, M. Steinhart and U. Gösele, *Nano Lett.*, 2007, **7**, 1516–1520.

155 Y. Xie, S. Guo, Y. Ji, C. Guo, X. Liu, Z. Chen, X. Wu and Q. Liu, *Langmuir*, 2011, **27**, 11394–

11400.

156 B. Peng, Z. Li, E. Mutlugun, P. L. Hernández Martínez, D. Li, Q. Zhang, Y. Gao, H. V. Demir and Q. Xiong, *Nanoscale*, 2014, **6**, 5592–5598.

157 A. Guerrero-Martínez, J. Pérez-Juste, E. Carbó-Argibay, G. Tardajos and L. M. Liz-Marzán, *Angew. Chemie*, 2009, **121**, 9648–9652.

158 A. D. Law, D. M. A. Buzza and T. S. Horozov, *Phys. Rev. Lett.*, 2011, **106**, 128302.

159 A. D. Law, M. M. Auriol, D. Smith, T. S. Horozov and D. M. A. Buzza, *Phys. Rev. Lett.*, 2013, **110**, 138301.

160 M. Rey, A. D. Law, D. M. Buzza and N. Vogel, *J. Am. Chem. Soc.*, 2017, **139**, 17464–73.

161 M. Rey, T. Yu, K. Bley, K. Landfester, D. M. A. Buzza and N. Vogel, *Langmuir*, 2018, **34**, 9990–10000.

162 T. Kraus, D. Brodoceanu, N. Pazos-Perez and A. Fery, *Adv. Funct. Mater.*, 2013, **23**, 4529–4541.

163 B. Ai, H. Möhwald, D. Wang and G. Zhang, *Adv. Mater. Interfaces*, 2017, **4**, 1600271.

164 M. E. J. Hummel, C. Stelling, B. A. F. Kopera, F. A. Nutz, M. Karg, M. Retsch and S. Förster, *Langmuir*, 2019, **35**, 973–979.

165 P. Collins, *Differential and Integral Equations*, Oxford university press, 2006.

166 J. N. Israelachvili, *Intermolecular & Surface Forces*, Elsevier Science, Amsterdam, 2nd edn., 2011.

167 L. D. Landau, E. M. Lifshitz and L. P. Pitaevskii, *Electrodynamics of Continious Media*, Elsevier Butterworth-Heinemann, Oxford, 2nd edn., 1984.

168 D. R. Lide, Ed., in *CRC Handbook of Chemistry and Physics*, CRC Press/Taylor and Francis, Boca Raton, 88th edn., 2008.

169 G. I. Guerrero-García and M. O. De La Cruz, *J. Chem. Theory Comput.*, 2013, **9**, 1–7.

170 Z. Samec, *Chem. Rev.*, 1988, **88**, 617–632.

171 E. J. W. Verwey and K. F. Niessen, *London, Edinburgh, Dublin Philos. Mag. J. Sci.*, 1939,

28, 435–446.

172 R. M. Erb, H. S. Son, B. Samanta, V. M. Rotello and B. B. Yellen, *Nature*, 2009, **457**, 999–1002.

173 K. S. Khalil, A. Sagastegui, Y. Li, M. A. Tahir, J. E. S. Socolar, B. J. Wiley and B. B. Yellen, *Nat. Commun.*, 2012, **3**, 1–8.

174 R. Lekkerkerker, Henk NW. Tuinier, in *Colloids and the Depletion Interaction*, Springer, Dordrecht, 2011, pp. 57–108.

175 T. S. Horozov, R. Aveyard, B. P. Binks and J. H. Clint, *Langmuir*, 2005, **21**, 7405–7412.

176 J. Lucassen, *Colloids and Surfaces*, 1992, **65**, 131–137.

177 J. Huang, Q. Qin and J. Wang, *Processes*, 2020, **8**, 1138.

178 V. M. Shalaev, *Nat. Photonics*, 2007, **1**, 41–48.

179 J. A. Fan, C. Wu, K. Bao, J. Bao, R. Bardhan, N. J. Halas, V. N. Manoharan, P. Nordlander, G. Shvets and F. Capasso, *Science.*, 2010, **328**, 1135–1138.

180 W. van der Stam, A. P. Gantapara, Q. A. Akkerman, G. Soligno, J. D. Meeldijk, R. van Roij, M. Dijkstra and C. De Mello Donega, *Nano Lett.*, 2014, **14**, 1032–1037.

181 L. Yao, L. Botto, M. Cavallaro, B. J. Bleier, V. Garbin and K. J. Stebe, *Soft Matter*, 2013, **9**, 779–786.

182 R. P. Doherty, T. Varkevisser, M. Teunisse, J. Hoecht, S. Ketzetzi, S. Ouhajji and D. J. Kraft, *Soft Matter*, 2020, **16**, 10463–10469.

183 G. Soligno, M. Dijkstra and R. Van Roij, *J. Chem. Phys.*, 2014, **141**, 244702.

Appendix 1 Surface Evolver Program and Parallelisation

In the following we outline the technical details of running Surface Evolver in parallel across multicore machines to reduce the lead time for a full set of results. We run this on The University of Hull's Linux based supercomputer Viper across 6000 cores, managed by a SLURM scheduler. The process can be modified in a straightforward manner to run on other machines and/or operating systems as will be detailed.

The following set up steps all take place within the local Surface Evolver directory, in our case /ev272v, in which we create a new folder called array_job and inside this folder create a file named submit1.sh which contains the following code:

```
#!/bin/bash
#SBATCH -J job1
#SBATCH -N 1
#SBATCH -n 1
#SBATCH -o %N.%j.%a.out
#SBATCH --array=1-100
#SBATCH -e %N.%j.%a.err
#SBATCH -p compute
echo "$SLURM_JOB_NODELIST $SLURM_ARRAY_TASK_ID"
#cd ev272v/
export LD_LIBRARY_PATH=$LD_LIBRARY_PATH:/home/462915/ev272v/lib64
#cd src
#./evolver
SCRATCH=/local/$USER/$SLURM_JOB_ID/$SLURM_ARRAY_TASK_ID
echo Creating temp dir $SCRATCH
ulimit -f 1048576
mkdir -p $SCRATCH || exit $?
echo Coping files. srun cp is equivalent to loop over each node + scp
cp -r /home/462915/ev272v/fe/${SLURM_ARRAY_TASK_ID}.fe $SCRATCH || exit $?
cd $SCRATCH
/home/462915/ev272v/src/evolver -r "run; exit 0; q" -x $SCRATCH/${SLURM_ARRAY_TASK_ID}.fe 1>
 $SCRATCH/${SLURM_ARRAY_TASK_ID}.output 2>$SCRATCH/${SLURM_ARRAY_TASK_ID}.error
echo calculation finished - copying files back to home directory
cp $SCRATCH/* $SLURM_SUBMIT_DIR
echo calculation finished - removing scratch dir
rm -rf  $SCRATCH
```

This submission script looks for files inside the directory: home/USER/ev272v/fe/ and searches for files with names between 1.fe -100.fe. When a core on Viper becomes free, it copies a simulation script to the core and executes everything inside the run command inside the simulation file. Once a simulation set has finished, all files on the core get copied back to the local drive, inside the same directory as submit1.sh is stored in. There will be the original simulation, an output.txt, error.txt and any output from the simulation itself. To modify the process to a local windows

machine the array job script would be replaced with a .bat file with the relevant syntax and split across the number of cores on the local machine.

In the following example we simulate two of the hexagonal platelets studied in section 6.3.2 at an interface with an initial centre to centre separation (Sep) of $10r$, where r is the particle radius. The simulation file, shown below, has a PARAMETER Sep = $10 * r$ on line 1, and the output command to write the total energy and separation to a file : outp := {printf " %f\n", total_energy >> "c:\\Users\\YOU\\output.txt" } on lines 229 - 234. We will give an example of how we use Python programs firstly to automatically generate 100 unique simulation scripts which decrease the particle separation by $0.1 * Sep$ and output the results to a unique file. Secondly, to automatically compile all these files into a single one upon completion, as described in Chapter 3. Before doing so however, we will first make some notes on the structure and salient features of the Surface Evolver script for clarity.

The Simulation script is shown below and has the C++ syntax, an overview of the structure is as follows. Global parameters, definitions and functions are placed at the top of the file followed by function definitions preface by the keywords PARAMETER, #define and formula respectively. The systems geometry is then defined, as detailed in Chapter 3, with the keyword's vertices, edges and faces alongside any constraints which apply to them. Finally, under the read heading are the execution statements which call the various methods of Surface Evolver such as input/output operations, tessellation schemes and minimisation procedures. The final "run" statement bundles together all the sub-routines and is the statement which is passed from the array job script to execute the simulation. A given particle morphology/configuration is developed on a local machine and tested with some boundary conditions before the full set is run.

```
// 2d parameterised hexagonal plate
// define constants:
PARAMETER Sep = 2.5
#define r 1
#define rad pi/180.
#define component (r*sin(30.0*rad))
#define Boxsize 20*r

// coefficients:
#define a 1
#define b 1
#define c 1
#define d 0.1
#define h d/2
PARAMETER eta = 4
PARAMETER eta2 = 2
PARAMETER tilt_angle = 0.0        //first rotation about y axis
PARAMETER ta = 0.0
PARAMETER rotation = 0.0         //second rotation about x prime axis
PARAMETER rot = 0.0
PARAMETER tilt_angleP2 = 0.0    //first rotation about y axis
PARAMETER taP2 = 0.0
PARAMETER rotationP2 = 30.0   //second rotation about x prime axis
PARAMETER rotP2 = 30.0
#define psi ((pi/180)*tilt_angle) //conversion of first rotation to radians
#define beta ((pi/180)*rotation)//conversion of second rotation to radians
#define psiP2 ((pi/180)*tilt_angleP2)      //conversion of first rotation to radians
#define betaP2 ((pi/180)*rotationP2)     //conversion of second rotation to radians
PARAMETER contact_angle = 90.0
#define gamma  ((cos((contact_angle*pi)/180))/2)
#define gamma2  ((-cos((contact_angle*pi)/180))/2)
#define theta0 0                                  // i.e. at x=r,y=0
#define A 0.05                                    // amplitude of undulation
#define rc sqrt(xprime_2^2+yprime_2^2) //*****************
#define zZero (A*rc*cos(3*(theta-theta0)))
#define var (sqrt((yprime_2/(sqrt(yprime_2^2+xprime_2^2)))^2))
#define var2 (yprime_2/(sqrt(yprime_2^2+xprime_2^2)))
#define checkUnity (var-(var%1))
#define sign (2*(floor(zprime_2/10))+1)
#define argument (checkUnity?(sign*(0.9999999999999999)):(var2))
#define theta sign*(acos(argument))
#define yprime_1 y
#define zprime_1 ((-x*sin(psi))+(z*cos(psi)))
#define xprime_1 ((x*cos(psi))+(z*sin(psi)))
#define xprime_2 ((xprime_1*cos(beta))+(yprime_1*sin(beta)))
#define yprime_2 ((-xprime_1*sin(beta))+(yprime_1*cos(beta)))
#define zprime_2 zprime_1
#define rcP2 sqrt(xprime_2P2^2+yprime_2P2^2) //*****************
#define zZeroP2 (A*rcP2*cos(3*(thetaP2-theta0)))
#define varP2 (sqrt((yprime_2P2/(sqrt(yprime_2P2^2+xprime_2P2^2)))^2))
#define var2P2 (yprime_2P2/(sqrt(yprime_2P2^2+xprime_2P2^2)))
#define checkUnityP2 (varP2-(varP2%1))
#define signP2 (2*(floor(zprime_2P2/10))+1)
#define argumentP2 (checkUnityP2?(signP2*(0.9999999999999999)):(var2P2))
```

```
#define thetaP2 signP2*(acos(argumentP2))
#define yprime_1P2 (y-Sep)
#define zprime_1P2 z //((-x*sin(psiP2))+(z*cos(psiP2)))
#define xprime_1P2 x //((x*cos(psiP2))+(z*sin(psiP2)))
#define xprime_2P2 ((xprime_1P2*cos(betaP2))+(yprime_1P2*sin(betaP2)))
#define yprime_2P2 ((-xprime_1P2*sin(betaP2))+(yprime_1P2*cos(betaP2)))
#define zprime_2P2 zprime_1P2

constraint plate
formula:
((((sqrt(3)/2)*xprime_2+(1/2)*yprime_2)/a)^eta+(yprime_2/b)^eta+(((sqrt(3)/2)*xprime_2-
(1/2)*yprime_2)/c)^eta+((zprime_2-zZero)/d)^eta2) = 1

constraint plateP2
formula:
((((sqrt(3)/2)*xprime_2P2+(1/2)*yprime_2P2)/a)^eta+(yprime_2P2/b)^eta+(((sqrt(3)/2)*xprim
e_2P2-(1/2)*yprime_2P2)/c)^eta+((zprime_2P2-zZeroP2)/d)^eta2) = 1

constraint x_limit_positive                    // Set limits of boundary edges
formula: x = Boxsize
constraint x_limit_negative
formula: x = -Boxsize
constraint y_limit_positive
formula: y = Boxsize
constraint y_limit_negative
formula: y = -Boxsize

vertices
//upper face
1 r        0          -h         constraint plate
2 component    -r         -h         constraint plate
3 -component   -r         -h         constraint plate
4 -r       0          -h         constraint plate
5 -component   r          -h         constraint plate
6 component    r          -h         constraint plate
// lower face
7 r        0          h          constraint plate
8 component    -r         h          constraint plate
9 -component   -r         h          constraint plate
10 -r      0          h          constraint plate
11 -component r          h          constraint plate
12 component   r          h          constraint plate
13 Boxsize     -Boxsize        0          constraints x_limit_positive,y_limit_negative
14 -Boxsize    -Boxsize        0          constraints x_limit_negative,y_limit_negative
15 -Boxsize    (Sep/2) 0          constraints x_limit_negative
16 Boxsize     (Sep/2) 0          constraints x_limit_positive

//Particle 2
//upper face
17 r       Sep        -h         constraint plateP2
18 component   -r+Sep     -h         constraint plateP2
19 -component  -r+Sep     -h         constraint plateP2
20 -r      Sep        -h         constraint plateP2
21 -component r+Sep     -h         constraint plateP2
```

```
22 component  r+Sep   -h        constraint plateP2
// lower face
23 r      Sep      h         constraint plateP2
24 component  -r+Sep  h         constraint plateP2
25 -component -r+Sep  h         constraint plateP2
26 -r     Sep      h         constraint plateP2
27 -component r+Sep   h         constraint plateP2
28 component  r+Sep   h         constraint plateP2
29 -Boxsize       Boxsize 0         constraints x_limit_negative,y_limit_positive
30 Boxsize        Boxsize 0 constraints x_limit_positive,y_limit_positive

edges
// lower face
1 1 2     constraint plate
2 2 3   constraint plate
3 3 4   constraint plate
4 4 5   constraint plate
5 5 6   constraint plate
6 6 1   constraint plate
//upper face
7 7 8               constraint plate
8 8 9      constraint plate
9 9 10     constraint plate
10 10 11    constraint plate
11 11 12    constraint plate
12 12 7     constraint plate
//sides
13 1 7              constraint plate
14 2 8     constraint plate
15 3 9     constraint plate
16 4 10    constraint plate
17 5 11    constraint plate
18 6 12    constraint plate

//interface
19 13 14 constraint y_limit_negative
20 14 15 constraint x_limit_negative
21 15 16 //constraint y_limit_positive
22 16 13 constraint x_limit_positive
23 13 2
24 14 3
25 15 4
26 16 6

//Particle 2
// lower face
27 17 18          constraint plateP2
28 18 19   constraint plateP2
29 19 20   constraint plateP2
30 20 21   constraint plateP2
31 21 22   constraint plateP2
32 22 17   constraint plateP2
//upper face
33 23 24                  constraint plateP2
```

```
34 24 25     constraint plateP2
35 25 26    constraint plateP2
36 26 27   constraint plateP2
37 27 28   constraint plateP2
38 28 23    constraint plateP2
//sides
39 17 23          constraint plateP2
40 18 24    constraint plateP2
41 19 25    constraint plateP2
42 20 26   constraint plateP2
43 21 27   constraint plateP2
44 22 28   constraint plateP2
45 15 29 constraint x_limit_negative
46 29 30 constraint y_limit_positive
47 30 16 constraint x_limit_positive
48 15 19
49 29 20
50 30 22
51 16 18

faces
// lower face
1 1 2 3 4 5 6                        constraint plate color yellow tension gamma2
// sides
2 7 -14 -1 13         constraint plate color yellow tension gamma
3 8 -15 -2 14         constraint plate color yellow  tension gamma
4 9 -16 -3 15         constraint plate color yellow   tension gamma
5 10 -17 -4 16        constraint plate color yellow   tension gamma
6 11 -18 -5 17        constraint plate color yellow   tension gamma
7 12 -13 -6 18        constraint plate color yellow   tension gamma
//upper face
8 -12 -11 -10 -9 -8 -7  constraint plate color yellow tension gamma
//interface
9 2 -24 -19 23              color green
10 -20 24 3 -25    color green
11 -21 25 4 5 -26   color green
12 26 6 1 -23 -22   color green

//Particle2
// lower face
13 27 28 29 30 31 32                        constraint plateP2 color yellow tension gamma2
// sides
14 33 -40 -27 39        constraint plateP2 color yellow tension gamma
15 34 -41 -28 40        constraint plateP2 color yellow      tension gamma
16 35 -42 -29 41        constraint plateP2 color yellow   tension gamma
17 36 -43 -30 42       constraint plateP2 color yellow   tension gamma
18 37 -44 -31 43       constraint plateP2 color yellow   tension gamma
19 38 -39 -32 44       constraint plateP2 color yellow   tension gamma
//upper face
20 -38 -37 -36 -35 -34 -33  constraint plateP2 color yellow tension gamma
//
21 -48 21 51 28             color green
22 -45 48 29 -49    color green
23 49 30 31 -50 -46 color green
```

```
24 50 32 27 -51 -47 color green

read
outp := {
          {
           printf " %f\t", Sep >> "c:\\Users\\462915\\.txt" ;
           printf " %f\n", total_energy >> "c:\\Users\\462915\\.txt" ;
          }
 }
set background white ;
groom_length := 0.2;
groom := {
  refine edge where length > groom_length;
  u; V;
  delete edge where length < groom_length/5;
}
gogo := {
  groom 8;
  {g 5; groom; } 20;
fix vertex where on_constraint plate;
fix vertex where on_constraint plateP2;
 hessian_seek; hessian_seek;
 unfix vertex where on_constraint plate;
 unfix vertex where on_constraint plateP2;

  { g 5; groom; } 5;
}
go_more := {
  { recalc; M 1;
    {g 5; groom } 10;
           fix vertex where on_constraint plate;
           fix vertex where on_constraint plateP2;
    hessian_seek; hessian_seek;
          unfix vertex where on_constraint plate;
          unfix vertex where on_constraint plateP2;
    {g 5; groom } 10;
M 2; {g 5; u; V;} 10;
refine edge where on_constraint plate;
refine edge where on_constraint plateP2;
 u; V;
{g 5; u; V;} 50;
  }
}

FacetGeometry:=foreach facet ff do { printf "%d  %d %d %d\n", ff.id,ff.edge[1].oid,
    ff.edge[2].oid,ff.edge[3].oid }

resolve:={{r; groom}2;u;V}; {r; groom}2}
init:={gogo;{eta+=2;resolve}4}
setUp1:={for (ta -= 0 ; tilt_angle < ta ; tilt_angle += 2.0)
 {
          gogo;
 }}
setUp2:={for (rot -= 0 ; rotation < rot ; rotation += 2.0)
```

```
 {
        gogo;
 }}

setUp3:={for (rotP2 -= 0 ; rotationP2 < rotP2 ; rotationP2 += 2.0)
 {
        gogo;
 }}
contour:= {  ddd:=sprintf"c:\\Users\\scott\\HexPlateContour.txt";
    foreach vertex where not on_constraint plate do
        {
         printf "%f %f %f \n" ,x, y, z >> ddd;
        }}

contact_line :=  {
     dd:=sprintf"c:\\Users\\comsol\\Contact_line_cube_0_to_20.txt";
   foreach vertex where on_constraint plate do
   { printf "%f\t %f\t %f\n", x ,y ,z >> dd;
        }}
run:= {init;setUp2;setUp3;gogo;go_more;outp}
```

Once we have a working surface evolver simulation and have tested it with some boundary conditions it is saved as a .txt file, for this example masterHexPlates.txt. Finally, we place the commands we wish to execute in the run statement on the final line of the simulation file. This statement contains any initialisation protocols, the tessellation and minimisation schemes and any output commands, all of which can be either custom written or internal Surface Evolver methods.

To automatically spawn the desired number of simulations we use the Python script shown below which opens the masterHexPlates.txt file and stores each line as a single string type element in an indexed list. Next, we create a loop which iterates over the number of simulations we wish to create i.e., 100 simulations each one incrementing the particle separation by $0.1 * Sep$ and changing the output file name and simulation file name to the index of the loop with the .fe post-fix. In this manner we create 100 simulations, named 1.fe – 100.fe, inside of which the output destination are corresponding output files 1.txt – 100. Note, we need a numbered file name because

that is what allows us to call the jobs from the submit.sh script line ${SLURM_ARRAY_TASK_ID}.fe because the SLURM array is an array of numbers from 1 – 100.

```
FileOutputName = []
# note list names not meaningful, reused and edited program many times, left over from
# older work
space = ' '
filePath = "toUpload\\"
end = '.fe'
def file_reader(file_name):
      #function to read in data line by line, returns all data
      # in single list,each element is one line.
      a = open(file_name, "r")
      data = a.readlines()
      a.close()
      return(data)

# Spawn list of parameter values we want to change  in the script, in this case use for
#Seperaion
tilts=[]
number= 10.0
for i in range(0,100):
   number-=0.1
   var=str(number)
   tilts.append(var)


c=0
for tilt in tilts:
   c+=1
   data=file_reader( "masterSpawn.txt" ) # open sim file
   phi=data[2].split(' ') # this line is: "PARAMETER Sep = 2.5"
   phi[-1]=str(tilt) # change Sep value
   newLine1=phi[0]+space+phi[1]+space+phi[2]+space+phi[3] # rebuild line from list
   data[2]=newLine1 # replace original with newline

   """ Now do the same for the file outputs, want unique name for each loop iteration
   so use loop counter for this """
   x=data[230].split(' ') # line of interest
   x2=data[231].split(' ') # 2nd line of interest
   out=x[21] # file name in line of interest
   out2=x2[22] # file name in line of interest

   new = ""
   for letter in out:
   # because string need to rebuild filepath and change to unique file name

      if letter is out[20]: # means now at filename
         new+=str(c)
```

```
            new+=letter
        else: # means sill rebuilding original line
            new+=letter

    # As above for 2nd line of interest
    new2 = ""
    for letter in out2:
        if letter is out2[20]:
            new2+=str(c)
            new2+=letter
        else:
            new2+=letter
    x[21]=new
    x2[22]=new2
    replaceLine = ""
    # now rebuild entire command:
    for y in x:
        replaceLine+=y
    data[230]=replaceLine

    # as above but for 2nd
    replaceLine2 = ''
    for y in x2:
        replaceLine2+=y
    data[231]=replaceLine2

    fN=filePath+str(c)+end

    # output SE sim:
    file = open(fN, "w")
    for line in data:
        file.write(str(line))
        file.write('\n')
    file.close()
```

The final step of the process is a simple Python program, shown below, which lists all the files in a specified directory, loops over each one, extracts the data and writes it to a single master file from which we can perform data analysis.

```
"""Program looks in directory, iterates over all files within extracting the data on first line,
compiles and outputs a single file named compiledData.txt """

import os
dirName = "forProcessing" # dir to compile
fileNames = os.listdir(dirName) # returns all filenames in directory
fullDataSet = []

def file_reader(file_name):
    #function to read in data line by line, returns all data
```

```
        # in single list,each element is one line.
        a = open(file_name, "r" )
        data = a.readlines()
        a.close()
        return(data)

for x in fileNames:
    # open each file
    data = file_reader((dirName+'\\'+x))
    y = data[0].split('\t')              # data on first line
    fullDataSet.append(y)

# output compiled set
output = open('compiledData.txt','w')
for z in fullDataSet:
    # note, format to your requirements, currently tab spaced with blank line inbetween
    datapoints
    for var in z:
        output.write(str(var))
        output.write('\t')
    output.write('\n')
output.close()
```